

*ANTI-REFLECTION COATINGS AND  
OPTICAL INTERFERENCE IN  
PHOTOVOLTAICS*

**Gerald Womack**



**A Doctoral Thesis**

**Submitted in partial fulfilment of the requirements of the award of**

**Doctor of Philosophy at Loughborough University**

**June 2017**

**© Gerald Womack**

**Centre for Renewable Systems Technology**

**School of Mechanical, Electrical and Manufacturing Engineering**

**Loughborough University**

*I dedicate this work to Verity Theophanous.*

Every 24 hours, enough sunlight touches the Earth to provide the energy for the entire planet for 24 years. - Martha Maeda

## ABSTRACT

Light reflection from the glass surface of a photovoltaic (PV) module is a significant source of energy loss for all types of PV devices. The reflection at the glass and air interface accounts for ~4% of the total energy. Single layer anti-reflection coatings with sufficiently low refractive index have been used, such as those using magnesium fluoride or porous silica, but these are only effective over a narrow range of wavelengths. Multilayer-antireflection coatings reduce the weighted average reflection over the wavelength range used by solar technologies more effectively by utilising interference effects. Multilayer stacks consisting of silica and zirconia layers deposited using reactive magnetron sputtering and single layer porous silica coatings were compared in terms of effectiveness and durability. Details of the stack design, sputter deposition process parameters, and the optical and micro-structural properties of the layers of the multilayer coating are provided and similar properties where applicable for the single layer coatings.

Anti-reflection coatings on glass exposed to the outdoors must not degrade over the lifetime of the module. A comprehensive set of accelerated environmental durability tests has been carried out in accordance with IEC 61646 PV qualification tests. The durability tests confirmed no damage to the coatings or performance drop as a result of thermal cycling or damp heat. All attempts to perform pull tests on either coating resulted in either adhesive or substrate failure, with no damage to the coating itself. Scratch resistance, abrasion resistance, and adhesion tests have also been conducted. The optical performance of the coatings was monitored during these tests and the coatings were visually inspected for any sign of mechanical failure. These tests provide confidence that broadband anti-reflection coatings are highly durable and will maintain their performance over the lifetime of the solar module. Additionally heat treatment experiments demonstrated both coatings can withstand up to 600°C temperatures and can thereby withstand CdTe manufacturing processes allowing for pre-coated glass. Additionally experiments demonstrated that multi-layer coatings are resistant to acid attack.

Thin film photovoltaic devices are multilayer opto-electrical structures in which light interference occurs. Light reflection at the interfaces and absorption within the window layers reduces transmission and, ultimately, the conversion efficiency of photovoltaic

devices. Optical reflection losses can be reduced by adjusting the layer thicknesses to achieve destructive interference within the structure of the cell. The light transmission to the CdTe absorber of a CdS/CdTe cell on a fluorine doped tin oxide transparent conductor has been modelled using the transfer matrix method. The interference effect in the CdS layer and high resistance transparent buffer layers ( $\text{SnO}_2$  and ZnO) has been investigated. The modelling shows that due to relatively high absorption within the  $\text{SnO}_2$  layer, there are modest benefits to engineering anti-reflection interference in the stack. However, a ZnO buffer layer has limited absorption and interference can be exploited to provide useful anti-reflection effects. Additionally the light transmission to the perovskite absorber of a thin film solar cell using fluorine doped tin oxide (FTO) transparent conductor has been modelled. Alternative transparent conductor materials have also been investigated including aluminium doped zinc oxide (AZO) and indium tin oxide (ITO) and shown to be beneficial to transmission.

## ACKNOWLEDGEMENTS

I would like to thank my academic and industrial supervisors, Prof Michael Walls, Dr Jake Bowers, Dr Geraldine Durand, and Mr Andrew Whitaker. Your guidance and insights were invaluable. I would also like to thank my co-authors; Dr Piotr Kaminski for his enlightening discussion and help with my scientific writing, Dr Ali Abbas for his masterful use of TEM and SEM, Mr Kenan Isbilir for assistance in weathering experiments, Dr Patrick Isherwood for his useful insights into modelling, and Prof Ralph Gottschalg for access to climatic chambers and general discussion. Additionally I am grateful to the UKERC for funding this work through the EPSRC Supergen SuperSolar Hub, and to TWI Ltd and NSIRC Ltd for supporting a CASE studentship. I am also grateful to Prof W. Sampath and Dr K Barth of Colorado State University for the thin film CdTe cell used in Figure 4.13. Also I would like to thank my friends and family for supporting me throughout my PhD particularly my parents Ann and David Womack for raising me, I'm sure it will end one day, and finally my fiancée Ms Verity Theophanous for her unwavering ability to deal with me, I'm glad you were here.

# CONTENTS

<b>1 INTRODUCTION.....</b>	<b>1</b>
1.1 THE SUN AS A POWER SOURCE .....	2
1.2 PHOTOVOLTAICS .....	3
1.3 PHOTOVOLTAIC TECHNOLOGIES .....	5
1.4 SCOPE OF THIS THESIS .....	7
<b>2 ANTI-REFLECTION COATINGS.....</b>	<b>9</b>
2.1 DESIGN PRINCIPLES .....	9
2.2 THE TRANSFER MATRIX METHOD.....	10
2.3 MULTILAYER AR .....	16
2.4 TEXTURED AR COATINGS .....	16
2.5 ADDITION OF HYDROPHOBIC COATING .....	17
<b>3 DEPOSITION TECHNIQUES FOR THIN FILMS.....</b>	<b>18</b>
3.1 THIN FILM DEPOSITION METHODS .....	19
3.1.1 <i>Reactive Magnetron Sputtering</i> .....	19
3.2 SOLUTION GELATION .....	21
3.2.1 <i>Dip coating</i> .....	21
3.2.2 <i>Spin coating</i> .....	23
3.2.3 <i>Meniscus coating</i> .....	24
3.3 INDUSTRIAL SOL-GEL COATINGS .....	25
3.3.1 <i>Porous Silica and Nano Spheres</i> .....	25
3.3.2 <i>DSM Hard Coat</i> .....	26
3.4 GLASS SUBSTRATE PREPARATION.....	28
<b>4 APPLICATION OF ANTI-REFLECTION COATINGS TO THIN FILM CDTE</b>	<b>29</b>
4.1 THIN FILM MAR COATINGS FOR CdTe.....	29
4.1.1 <i>Coating Design Principles</i> .....	30
4.1.2 <i>Modelled Coatings</i> .....	33
4.1.3 <i>Deposited SiO<sub>2</sub>/ZrO<sub>2</sub> Coatings for thin film CdTe photovoltaics</i> .....	40
4.2 SINGLE LAYER COATINGS .....	48
4.2.1 <i>Deposition methods</i> .....	48
4.2.2 <i>TWI sol-gel coatings</i> .....	49
4.2.3 <i>Commercial sol-gel hard coats</i> .....	50
4.3 DISCUSSION.....	52
<b>5 APPLICATION OF ANTI-REFLECTION COATINGS TO OTHER PV TECHNOLOGIES.....</b>	<b>53</b>

5.1 INTRODUCTION.....	53
5.2 MULTILAYER ANTI-REFLECTION COATINGS.....	54
5.2.1 <i>Multilayer anti-reflection experimental and Design</i> .....	54
5.2.2 <i>Multilayer Anti-Reflection coating for thin film a-Si PV</i> .....	54
5.2.3 <i>Multilayer Anti-Reflection coating for Perovskite PV</i> .....	56
5.2.4 <i>Multilayer Anti-Reflection coating for CIGS</i> .....	58
5.2.5 <i>MAR Comparison</i> .....	60
5.3 SOL-GEL ANTI-REFLECTION COATINGS.....	61
5.3.1 <i>Comparison and discussion</i> .....	63
<b>6 DURABILITY OF ANTI-REFLECTION COATINGS .....</b>	<b>64</b>
6.1 INTRODUCTION.....	64
6.2 DURABILITY OF THE MULTILAYER ANTI-REFLECTION COATINGS.....	65
6.2.1 <i>Adhesion</i> .....	65
6.2.2 <i>High temperature stability</i> .....	68
6.2.3 <i>Resistance to temperature and humidity</i> .....	78
6.2.4 <i>Contact angle</i> .....	79
6.2.5 <i>Stability against thermal cycling</i> .....	80
6.2.6 <i>Water solubility testing</i> .....	81
6.2.7 <i>Acid attack</i> .....	83
6.2.8 <i>Abrasion resistance</i> .....	83
6.2.9 <i>Scratch Resistance</i> .....	84
6.3 DURABILITY OF THE SOL-GEL COATINGS .....	86
6.3.1 <i>Adhesion</i> .....	86
6.3.2 <i>High temperature stability</i> .....	87
6.3.3 <i>Resistance to temperature and humidity</i> .....	88
6.3.4 <i>Contact angle</i> .....	89
6.3.5 <i>Stability against thermal cycling</i> .....	91
6.3.6 <i>Water Solubility Test</i> .....	92
6.3.7 <i>Abrasion Resistance</i> .....	94
6.3.8 <i>Scratch resistance</i> .....	94
6.4 SUMMARY AND CONCLUSIONS .....	96
<b>7 MODELLING OF INTERFERENCE EFFECTS IN CDTE .....</b>	<b>99</b>
7.1 INTRODUCTION.....	99
7.1.1 <i>The thin film CdTe solar cell</i> .....	100
7.1.2 <i>High resistance transparent (HRT) buffer layers</i> .....	100

7.2 OPTICAL MODELLING .....	103
7.3 RESULTS.....	103
7.3.1 Varying the thickness of the CdS layer .....	103
7.3.2 Varying the thickness of the SnO <sub>2</sub> High Resistance Transparent buffer layer .....	104
7.3.3 Varying the thickness of the ZnO High Resistance Transparent buffer layer .....	105
7.3.4 A comparison of the optical effects of introducing SnO <sub>2</sub> and ZnO high resistance buffer layers .....	107
7.4 CONCLUSIONS .....	108
<b>8 OPTIMISATION OF PEROVSKITE SOLAR CELL STRUCTURE FOR MAXIMUM CURRENT COLLECTION .....</b>	<b>111</b>
8.1 INTRODUCTION.....	112
8.2 EXPERIMENTAL DETAILS .....	112
8.3 RESULTS.....	113
8.3.1 TiO <sub>2</sub> .....	113
8.3.2 Transparent conductor selection .....	115
8.3.3 ITO .....	115
8.3.4 AZO.....	117
8.4 MULTI-LAYER AR .....	119
8.5 SUMMARY .....	120
<b>9 CONCLUSIONS AND FUTURE WORK.....</b>	<b>121</b>
<b>10 REFERENCES.....</b>	<b>125</b>
<b>11 PUBLICATIONS .....</b>	<b>136</b>

# LIST OF TABLES

TABLE 4.1: THE OPTICAL CONSTANTS AND IMPORTANT MECHANICAL PROPERTIES OF CANDIDATE HIGH INDEX MATERIALS FOR USE IN MARS. ....	32
TABLE 4.2: THE STRUCTURE OF A MODELLED MAR COATING OPTIMISED FOR USE ON CdTe SOLAR CELLS, WHERE TiO <sub>2</sub> IS THE HIGH REFRACTIVE INDEX MATERIAL. ....	36
TABLE 4.3: THE STRUCTURE OF A MODELLED MAR COATING OPTIMISED FOR USE ON CdTe SOLAR CELLS, WHERE HfO <sub>2</sub> IS THE HIGH REFRACTIVE INDEX MATERIAL. ....	37
TABLE 4.4: THE STRUCTURE OF A MODELLED MAR COATING OPTIMISED FOR USE ON CdTe SOLAR CELLS, WHERE Ta <sub>2</sub> O <sub>5</sub> IS THE HIGH REFRACTIVE INDEX MATERIAL. ....	38
TABLE 4.5: THE STRUCTURE OF A MODELLED MAR COATING OPTIMISED FOR USE ON CdTe SOLAR CELLS, WHERE Nb <sub>2</sub> O <sub>5</sub> IS THE HIGH REFRACTIVE INDEX MATERIAL. ....	39
TABLE 4.6: MEASURED PERFORMANCE OF MAR FOR CdTe. ....	46
TABLE 4.7: MODELLED MAR COATING DESIGN OPTIMISED FOR USE ON A SPECIFIC CdTe SOLAR CELL. ....	47
TABLE 4.8: MAR COATING PERFORMANCE WHEN OPTIMISED FOR DIFFERENT OPTICAL SYSTEMS. ....	47
TABLE 4.9: A COMPARISON OF THE OPTICAL PROPERTIES OF THE ARCS PRESENTED IN THIS CHAPTER. ....	52
TABLE 5.1: THE STRUCTURE OF THE MAR DESIGNED FOR THIN FILM A-Si SOLAR CELLS. ....	55
TABLE 5.2: STRUCTURE OF THE MAR DESIGNED FOR USE ON PEROVSKITE SOLAR CELLS. ....	57
TABLE 5.3: THE STRUCTURE OF A SIX LAYER MAR DESIGNED FOR THIN FILM CIGS SOLAR CELLS. ....	59
TABLE 5.4: THE NUMBER OF LAYERS, THE THICKNESS, WEIGHTED AVERAGE REFLECTION (WAR), RELATIVE REDUCTION IN REFLECTION, AND THE INCREASED MAXIMUM JSC (IMPROVEMENT OVER UNCOATED GLASS IN BRACKETS). ....	61
TABLE 5.5: COMPARISON OF SOL-GEL COATINGS FOR VARIOUS PV TECHNOLOGIES. ....	63
TABLE 6.1: COMPARISON OF WAR OF SAMPLES ON TEC 7 BEFORE AND AFTER HEAT TREATMENT AT DIFFERENT TEMPERATURES. NUMBERS EXCLUDE BACK SURFACE REFLECTION. ....	74

TABLE 6.2: COMPARISON OF WAR OF SAMPLES ON EG BEFORE AND AFTER HEAT TREATMENT AT DIFFERENT TEMPERATURES. ....	77
TABLE 6.3: MEASURED WAR OF AR1 SAMPLES AFTER DH EXPOSURE: .....	88
TABLE 7.1: COMPARISON OF HRT LAYER PERFORMANCE.....	109
TABLE 9.1: SUMMARY OF CANDIDATE ARCS. THE COATINGS ARE COMPARED ON ANTI-REFLECTIVE PERFORMANCE, DURABILITY, HYDROPHOBICITY, AND DEPOSITION EXPENSE.....	123

# LIST OF FIGURES

FIGURE 1.1: A PLOT OF THE AM0 SPECTRUM AND THE AM1.5 SPECTRUM BOTH DIRECT (D) AND GLOBAL (G)[10].	3
FIGURE 1.2: (A) A DIAGRAM OF THE BAND STRUCTURE OF A SIMPLE P-N JUNCTION, AND (B) A VISUAL REPRESENTATION OF THE P-N JUNCTION.	5
FIGURE 2.1: DESTRUCTIVE INTERFERENCE IN A SINGLE LAYER AR COATING.	15
FIGURE 2.2: SCHEMATIC DIAGRAM OF A GENERIC 4-LAYER MAR COATING ON GLASS.	16
FIGURE 3.1: SCHEMATIC DIAGRAM OF THE APPARATUS USED IN MAGNETRON SPUTTERING, SHOWING MAGNETS AND MAGNETIC FIELD LINES.	20
FIGURE 3.2: THE STAGES OF THE DIP COATING PROCESS: THE SUBSTRATE IS DIPPED INTO A SOL, THE SUBSTRATE IS THEN REMOVED FROM THE SOL FORMING A WET LAYER COATING, THE COATING IS THEN LEFT TO DRY AND CONDENSE INTO A GEL.	22
FIGURE 3.3: THE SPIN COATING PROCESS: 1. AN EXCESS OF SOL IS APPLIED TO THE SUBSTRATE, 2. THE SUBSTRATE IS SPUN AND EXCESS SOL IS REMOVED BY WAY OF THE CENTRIFUGAL FORCE, 3. THE COATING THINS FURTHER AS THE SUBSTRATE SPINS SLOWER AND STOPS THROUGH EVAPORATION, 4. THE COATING IS DEPOSITED AND CONDENSED AFTER ANNEALING.	23
FIGURE 3.4: COMPARISON OF A TRADITIONAL NANO-POROUS SOL-GEL COATING AND A SILICA SHELL/RESIN COATING.	27
FIGURE 3.5 THE TRANSMITTANCE OF UNCOATED GLASS COMPARED TO THE TRANSMITTANCE OF KHEPRICOAT COATED GLASS BETWEEN 300 AND 2500NM WAVELENGTH. TAKEN FROM INNOVATION AT DSM: STATE OF THE ART SINGLE LAYER ANTI-REFLECTIVE COATINGS FOR SOLAR CELL COVER GLASS [72].	27
FIGURE 4.1: THE REFRACTIVE INDEX DISPERSION OF (A) $ZrO_2$ AND (B) $SiO_2$ USED FOR THE MAR DEPOSITION.	31
FIGURE 4.2: THE MODELLED REFLECTION SPECTRA OF AN UNCOATED 1MM GLASS SURFACE. THE BLACK SOLID CURVE MODELS THE REFLECTION FROM BOTH THE FRONT AND BACK GLASS SURFACES. THE RED DOTTED CURVE REPRESENTS THE FRONT SURFACE LOSSES ONLY.	34
FIGURE 4.3: THE REFRACTIVE INDEX DISPERSIONS OF HIGH REFRACTIVE INDEX MATERIAL CANDIDATES, $Nb_2O_5$ , $TiO_2$ , $Ta_2O_5$ , AND $HfO_2$ .	34

FIGURE 4.4: REFLECTION AT AIR GLASS INTERFACE WITH AND WITHOUT A $\text{SiO}_2/\text{TiO}_2$ MAR COATING. ....	36
FIGURE 4.5: REFLECTION AT AIR /GLASS INTERFACE WITH AND WITHOUT A $\text{SiO}_2/\text{HfO}_2$ MAR COATING. ....	37
FIGURE 4.6: REFLECTION AT AIR GLASS INTERFACE WITH AND WITHOUT A $\text{SiO}_2/\text{Ta}_2\text{O}_5$ MAR COATING. ....	38
FIGURE 4.7: REFLECTION AT AIR GLASS INTERFACE WITH AND WITHOUT A $\text{SiO}_2/\text{Nb}_2\text{O}_5$ MAR COATING. ....	39
FIGURE 4.8: COMPARISON OF ANGULAR DEPENDENCE OF MAR COATINGS OF VARYING HIGH REFRACTIVE INDEX MATERIAL.....	40
FIGURE 4.9: A SCHEMATIC DIAGRAM OF THE MAR COATING DESIGN ON A CdTe DEVICE, THE REFRACTIVE INDEX OF THE GLASS SUPERSTRATE IS $n=1.51$ AT 550NM. FOR MODELLING, THE GLASS WAS ASSUMED TO BE STANDARD SODA-LIME GLASS. ....	41
FIGURE 4.10: A 3D SCHEMATIC DIAGRAM OF THE REACTIVE SPUTTERING SYSTEM USED TO DEPOSIT THE MAR COATINGS. ....	42
FIGURE 4.11: STEM IMAGE OF A CROSS –SECTION OF THE MAR COATING DESIGN PRESENTED IN FIGURE 4.9, DEPOSITED USING REACTIVE SPUTTERING. THE $\text{SiO}_2$ IS AMORPHOUS AND THE $\text{ZrO}_2$ HAS A COLUMNAR STRUCTURE. ....	44
FIGURE 4.12: THE MODELLED REFLECTANCE OF MAR COATED GLASS WITH NO BACK REFLECTANCE, COMPARED TO THE MEASURED REFLECTANCE OF BARE GLASS AND MAR COATED GLASS. ....	45
FIGURE 4.13: THE J-V CHARACTERISTICS OF A CdTe SOLAR CELL AT FULL SUN ILLUMINATION, BEFORE AND AFTER THE APPLICATION OF A MAR, ALSO SHOWING POWER DECREASE. ....	45
FIGURE 4.14: THE MODELLED WAR FOR THE MAR DESIGN AND COMPARED WITH UNCOATED GLASS FOR A RANGE OF ANGLES OF INCIDENCE.....	46
FIGURE 4.15: SEM IMAGE OF A POROUS SILICA COATING WITH A SPHERE DIAMETER OF ~200NM. SPHERE SIZE VARIES, IDEAL AR PROPERTIES WERE FOUND USING SILICA SPHERES OF 12NM DIAMETER. ....	48
FIGURE 4.16: MEASURED REFLECTION OF SOL-GEL COATED GLASS (RED) COMPARED TO UNCOATED GLASS (BLACK).....	50

FIGURE 4.17: MEASURED TRANSMISSION OF SOL-GEL COATED GLASS (RED) COMPARED TO UNCOATED GLASS (BLACK).....	50
FIGURE 4.18: MEASURED REFLECTION AR 1 COATED GLASS (RED) COMPARED TO UNCOATED GLASS (BLACK).....	51
FIGURE 4.19: MEASURED TRANSMISSION OF AR1 COATED GLASS (RED) COMPARED TO UNCOATED GLASS (BLACK).....	51
FIGURE 5.1: MODELLED PERFORMANCES OF A FOUR LAYER MAR COATING FOR THIN FILM A-SI PV.....	55
FIGURE 5.2: THE MEASURED REFLECTANCE SPECTRUM FOR 4LAYER MAR COATING DESIGNED FOR A-SI SOLAR CELLS (BLACK LINE), THE MODELLED REFLECTANCE (BLUE LINE), AND THAT OF UNCOATED GLASS (RED LINE). ....	56
FIGURE 5.3: MODELLED PERFORMANCES OF A FOUR LAYERED MAR COATING FOR PEROVSKITE PV; THE FRONT REFLECTION OF THE MAR COATING (BLUE LINE), THE FRONT AND BACK REFLECTION (BLACK LINE), AND THE FRONT AND BACK REFLECTION OF UNCOATED GLASS (RED LINE).....	57
FIGURE 5.4: THE MEASURED REFLECTANCE SPECTRUM FOR SIX LAYER MAR COATING DESIGNED FOR PEROVSKITE SOLAR CELLS (BLACK LINE), THE MODELLED REFLECTANCE (BLUE LINE), AND THAT OF UNCOATED GLASS (RED LINE). ....	58
FIGURE 5.5: MODELLED PERFORMANCES OF SIX LAYERED MAR COATING FOR THIN FILM CIGS PV; THE FRONT REFLECTION OF THE MAR COATING (BLUE LINE), THE FRONT AND BACK REFLECTION (BLACK LINE), AND THE FRONT AND BACK REFLECTION OF UNCOATED GLASS (RED LINE).....	59
FIGURE 5.6: THE MEASURED REFLECTANCE SPECTRUM FOR A SIX LAYER MAR COATING DEPOSITED FOR A CIGS SOLAR CELL (BLACK LINE), COMPARED TO UNCOATED GLASS (RED LINE), AND THE MODELLED REFLECTANCE (BLUE LINE). ....	60
FIGURE 5.7: A COMPARISON OF THE MEASURED REFLECTANCES AT UNCOATED GLASS AND AR1 COATED GLASS SURFACES, BETWEEN 350NM AND 1100NM. ....	62
FIGURE 5.8 A COMPARISON OF THE MEASURED REFLECTANCES AT UNCOATED GLASS AND TWI SOL-GEL COATED GLASS SURFACES, BETWEEN 350NM AND 1100NM. ....	62

FIGURE 6.1: A SCHEMATIC DIAGRAM OF A DOLLY FIXED TO THE COATING SURFACE USING AN ADHESIVE, SHOWING THE DOLLY, STAND-OFF, COUPLING, AND UNIFORM PULL-OFF FORCE LINES.....	66
FIGURE 6.2: (A) THE BASE OF A DOLLY WITH GLASS ADHERED TO THE SURFACE, INDICATING NO COATING DELAMINATION. (B) A FRACTURED SAMPLE OF THE SPUTTERED SiO <sub>2</sub> /ZrO <sub>2</sub> MAR COATING ON GLASS AFTER A PULL TEST. THE COATING REMAINED UNDAMAGED. ....	67
FIGURE 6.3: A CROSS-HATCH TEST ON THE SPUTTERED SiO <sub>2</sub> /ZrO <sub>2</sub> MAR COATING BEFORE (A) AND AFTER THE APPLICATION OF TAPE (B).....	67
FIGURE 6.4: SEM SURFACE IMAGES OF AS DEPOSITED SPUTTERED SiO <sub>2</sub> /ZrO <sub>2</sub> MAR COATED GLASS SURFACE AND SURFACES EXPOSED TO TEMPERATURES OF 200°C, 400°C AND 500°C FOR 30 MIN. NO CRAZING IS OBSERVED. ....	69
FIGURE 6.5: AN OPTICAL MICROSCOPE IMAGE OF A SPUTTERED SiO <sub>2</sub> /ZrO <sub>2</sub> MAR SAMPLE EXPOSED TO 580 °C FOR 30 MIN, SHOWING NO VISIBLE DAMAGE.....	69
FIGURE 6.6: OPTICAL MICROSCOPE IMAGES OF A SPUTTERED SiO <sub>2</sub> /ZrO <sub>2</sub> MAR SAMPLE EXPOSED TO 590°C FOR 30 MIN, SHOWING AN ISOLATED FISSURE IN THE SURFACE OF THE COATING. ....	70
FIGURE 6.7: OPTICAL MICROSCOPE IMAGE OF A SPUTTERED SiO <sub>2</sub> /ZrO <sub>2</sub> MAR SAMPLE EXPOSED TO 600°C FOR 30 MIN REVEALING THE OCCURRENCE OF MILD CRAZING....	70
FIGURE 6.8: MEASURED REFLECTANCE SPECTRUM OF AS DEPOSITED SPUTTERED SiO <sub>2</sub> /ZrO <sub>2</sub> MAR COATED SODA LIME GLASS (SLG)(BLACK LINE) AND SPUTTERED SiO <sub>2</sub> /ZrO <sub>2</sub> MAR COATED GLASS HEAT TREATED TO 500°C (RED LINE), 590°C (GREEN LINE) AND 600°C (BLUE LINE) FOR 30MIN, INCLUDING BACK SURFACE REFLECTANCE. ....	71
FIGURE 6.9: CCI IMAGES OF MAR SAMPLES. A: AS DEPOSITED. B: HEAT TREATED AT 500°C. C: HEAT TREATED AT 600°C.....	72
FIGURE 6.10: SEM SURFACE IMAGES OF THE CENTRAL AREA OF SPUTTERED SiO <sub>2</sub> /ZrO <sub>2</sub> MAR COATINGS DEPOSITED ON TEC 7 AND THEN EXPOSED TO TEMPERATURES OF 500°C (TOP LEFT), 580°C (TOP RIGHT), 590°C (BOTTOM LEFT) AND 600°C (BOTTOM RIGHT). THE COATINGS SHOW NO SIGNS OF CRAZING. ....	73

FIGURE 6.11: OPTICAL MICROSCOPE IMAGE OF A SPUTTERED $\text{SiO}_2/\text{ZrO}_2$ MAR COATING DEPOSITED ON TEC 7 AND EXPOSED TO 590°C FOR 30 MINUTES SHOWING VERY MILD CRAZING AT THE WARPED EDGES OF THE GLASS. ....	74
FIGURE 6.12: MEASURED REFLECTANCE SPECTRUM OF AS DEPOSITED SPUTTERED $\text{SiO}_2/\text{ZrO}_2$ MAR ON TEC 7 GLASS (BLACK LINE), AND MAR COATED GLASS HEAT TREATED TO 500°C (RED LINE), 590°C (GREEN LINE) AND 600°C (BLUE LINE), INCLUDING BACK SURFACE REFLECTANCE. ....	75
FIGURE 6.13: SEM SURFACE IMAGES OF SPUTTERED $\text{SiO}_2/\text{ZrO}_2$ MAR SAMPLES DEPOSITED ON EAGLE GLASS EXPOSED TO TEMPERATURES OF 590°C, 650°C AND 700°C. THE SAMPLES SHOW NO SIGNS OF CRAZING. ....	76
FIGURE 6.14: OPTICAL MICROSCOPE IMAGES OF A SPUTTERED $\text{SiO}_2/\text{ZrO}_2$ MAR SAMPLE DEPOSITED ON EAGLE GLASS EXPOSED TO 800°C FOR 30 MINUTES WITH NO CRAZING OCCURRING, REVEALING MILD CRAZING. ....	76
FIGURE 6.15: MEASURED REFLECTANCE SPECTRUM OF UNCOATED GLASS (BLACK LINE) MAR COATED GLASS (RED LINE), AND MAR COATED GLASS HEAT TREATED TO 700°C (GREEN LINE) AND 800°C (BLUE LINE), INCLUDING BACK SURFACE REFLECTANCE. ....	77
FIGURE 6.16: PLOT OF HEAT TREATMENT TEMPERATURE AGAINST WAR FOR SPUTTERED $\text{SiO}_2/\text{ZrO}_2$ MAR COATED EAGLE GLASS. ....	78
FIGURE 6.17: MEASURED WEIGHTED AVERAGE REFLECTANCE (WAR) OF SPUTTERED $\text{SiO}_2/\text{ZrO}_2$ MAR SAMPLES AFTER EXPOSURE TO 85% HUMIDITY AT A TEMPERATURE OF 85°C, FOR UP TO 1000 HOURS. ....	79
FIGURE 6.18: A WATER DROP ON THE SURFACE OF A SPUTTERED $\text{SiO}_2/\text{ZrO}_2$ MAR COATING WITH A CONTACT ANGLE OF 35°. ....	80
FIGURE 6.19: A WATER DROP ON THE SURFACE OF A SPUTTERED $\text{SiO}_2/\text{ZrO}_2$ MAR COATING, COATED IN HMDS. THE CONTACT ANGLE IS 107°. ....	80
FIGURE 6.20: THE MEASURED WEIGHTED AVERAGE REFLECTANCE (WAR) OF SPUTTERED $\text{SiO}_2/\text{ZrO}_2$ MARs CYCLED 0, 100, 150, AND 200 TIMES BETWEEN -40°C AND 85°C IN A CLIMATIC CHAMBER. THIS IS A MINIMUM OF 2000MINS (~33HRS) AT EACH TEMPERATURE EXTREME. ....	81

FIGURE 6.21: THE WEIGHTED AVERAGE REFLECTANCE (WAR) OF SPUTTERED $\text{SiO}_2/\text{ZrO}_2$ MAR SAMPLES AFTER IMMERSION IN BOILING DI WATER FOR 0, 5, 15, AND 30MINS. .....	82
FIGURE 6.22: THE WEIGHTED AVERAGE REFLECTANCE (WAR) OF SPUTTERED $\text{SiO}_2/\text{ZrO}_2$ MAR COATED GLASS AFTER 0, 1, 2, 5 AND 10 CYCLES OF BOILING WATER CYCLING. CYCLES CONSISTED OF 2MIN OF BOILING DI WATER AND 1MIN COOLING IN ROOM TEMPERATURE DI WATER. ....	82
FIGURE 6.23: THE WEIGHTED AVERAGE REFLECTANCE (WAR) OF SPUTTERED $\text{SiO}_2/\text{ZrO}_2$ MAR SAMPLES AFTER EXPOSURE TO DILUTE SULPHURIC ACID SIMULATING THE EFFECT OF ACID RAIN FOR 0, 30, 60, 90, AND 120MINS.....	83
FIGURE 6.24: SCRATCHES IN THE SURFACE OF A SPUTTERED $\text{SiO}_2/\text{ZrO}_2$ MAR SAMPLE. THE SCRATCHES WERE PRODUCED BY PRESSING A MICRO-INDENTER INTO THE SURFACE OF THE COATING AND MOVING THE SAMPLE AS THE LOAD IS INCREASED. .	85
FIGURE 6.25: PLOT OF THE LOAD APPLIED TO THE MICRO-INDENTER AGAINST DEPTH PENETRATED INTO THE SURFACE OF THE SPUTTERED $\text{SiO}_2/\text{ZrO}_2$ MAR SAMPLE. ....	85
FIGURE 6.26: (A) THE BASE OF A DOLLY WITH GLASS ADHERED TO THE SURFACE, INDICATING NO COATING DELAMINATION. (B) A FRACTURED SAMPLE OF AR1 ON GLASS AFTER A PULL TEST. THE COATING REMAINED UNDAMAGED. ....	86
FIGURE 6.27: THE SURFACE OF AN AR1 SAMPLE AFTER HEAT TREATMENT AT $100^\circ\text{C}$ FOR 30MIN. ....	87
FIGURE 6.28: THE SURFACE OF AN AR1 SAMPLE AFTER HEAT TREATMENT AT $200^\circ\text{C}$ , SHOWING HIGH DAMAGE FOR 30MIN. ....	87
FIGURE 6.29: THE SURFACE OF AN AR1 SAMPLE AFTER EXPOSURE TO $700^\circ\text{C}$ FOR 30MIN. .....	88
FIGURE 6.30: PHOTOGRAPH OF SAMPLE 1 SHOWING SIGNS OF WATER DAMAGE AFTER 1000HRS OF DH EXPOSURE. ....	89
FIGURE 6.31: A WATER DROP ON THE SURFACE OF A TWI ARC WITH A CONTACT ANGLE OF $100^\circ$ . ....	90
FIGURE 6.32: A WATER DROP ON THE SURFACE OF A TWI ARC COATED IN HMDS, THE CONTACT ANGLE IS $111^\circ$ . ....	90

FIGURE 6.33: A WATER DROP ON THE SURFACE OF AN AR1 WITH A CONTACT ANGLE OF 9°.	91
.....	
FIGURE 6.34: A WATER DROP ON THE SURFACE OF AN AR1 COATED IN HMDS. THE CONTACT ANGLE IS 89°.	91
.....	
FIGURE 6.35: THE MEASURED WAR OF AR1 SAMPLES CYCLED 0, 100, 150, AND 200 TIMES BETWEEN -40°C AND 85°C IN A CLIMATIC CHAMBER (~33Hrs).	92
.....	
FIGURE 6.36: THE WAR OF AR1 SAMPLES AFTER IMMERSION IN DI WATER FOR 0, 6, 24, AND 96HRS.	93
.....	
FIGURE 6.37: THE WAR OF AR1 SAMPLES AFTER IMMERSION IN BOILING DI WATER FOR 0, 5, 15 AND 30MINS.	93
.....	
FIGURE 6.38: THE WAR OF SAMPLES OF AR1 AFTER 0, 1, 2 , 5, AND 10 CYCLES OF 2 MINUTES IN BOILING DI, FOLLOWED BY 1 MINUTE IN ROOM TEMPERATURE DI WATER.	94
.....	
FIGURE 6.39: SCRATCHES IN THE SURFACE OF AN AR1 SAMPLE. THE SCRATCHES WERE PRODUCED BY PRESSING A MICRO-INDENTER INTO THE SURFACE OF THE COATING AND MOVING THE SAMPLE AS THE LOAD IS INCREASED.	95
.....	
FIGURE 6.40: PLOT OF THE LOAD APPLIED TO THE MICRO-INDENTER AGAINST DEPTH PENETRATED INTO THE SURFACE OF THE AR1 SAMPLE.	96
.....	
FIGURE 7.1: A SCHEMATIC DIAGRAM OF THE CdTe SOLAR CELL STRUCTURE SHOWING THE POSITION OF (FROM BOTTOM TO THE TOP), THE BACK CONTACT, THE CdTe ABSORBER, THE CdS WINDOW LAYER, THE BUFFER LAYER, THE TCO LAYER, AND THE GLASS SUBSTRATE.	102
.....	
FIGURE 7.2: THE REFRACTIVE INDEX DISPERSION FOR SnO <sub>2</sub> AND ZnO, THE CANDIDATE HIGH RESISTANCE BUFFER LAYER MATERIALS.	102
.....	
FIGURE 7.3: THE EXTINCTION COEFFICIENTS OF SnO <sub>2</sub> AND ZnO, THE CANDIDATE HIGH RESISTANCE BUFFER LAYER MATERIALS.	102
.....	
FIGURE 7.4: THE MODELLED OPTICAL WEIGHTED AVERAGE TRANSMISSION (WAT) TO THE CdTe LAYER IN A CdTe PHOTOVOLTAIC DEVICE, PLOTTED AGAINST THE THICKNESS OF THE CdS LAYER. THE EFFECT OF A HIGH RESISTANCE BUFFER LAYER IS NOT INCLUDED.	104
.....	

FIGURE 7.5: THE MODELLED WAT TO THE ABSORBING LAYER OF A CdTe SOLAR CELL AS A FUNCTION OF CdS AND THE SnO<sub>2</sub> LAYER THICKNESS. THICKNESSES OF CdS AND SnO<sub>2</sub> LAYERS (NM) ARE PLOTTED ON THE X-Y PLANE AND THE MODELLED VALUE FOR WAT IS PLOTTED ALONG THE Z-AXIS. IN THIS REGION A MAXIMUM TRANSMISSION OCCURS AT 50NM CdS AND 48NM SnO<sub>2</sub>..... 105

FIGURE 7.6: THE MODELLED WAT TO THE ABSORBER LAYER FOR A CdTe SOLAR CELL WITH CdS WINDOW AND A ZnO HIGH RESISTANCE BUFFER LAYER. THE THICKNESS OF THE CdS AND ZnO LAYERS (NM) ARE PLOTTED ON THE X-Y PLANE AND THE MODELLED VALUE FOR WAT IS PLOTTED ALONG THE Z-AXIS..... 106

FIGURE 7.7: MODELLED WAT TO THE ABSORBER LAYER OF THE CdTe STACK PLOTTED AGAINST THICKNESS FOR THE TWO CANDIDATE HRT LAYERS. ZnO DATA IS REPRESENTED BY SOLID LINES AND SnO<sub>2</sub> DATA IS REPRESENTED BY DASHED LINES. VALUES ARE GIVEN AT SELECTED THICKNESSES OF CdS LAYER; 50, 100, 150, 200, 250 AND 300NM. .... 107

FIGURE 7.8: COMPARISON OF MODELLED WAT TO THE CdTe LAYER IN THE SOLAR CELL PLOTTED AGAINST THE THICKNESS OF THE ZnO AND SnO<sub>2</sub> BUFFER LAYERS. THE ZnO DATA IS REPRESENTED BY SOLID LINES AND SnO<sub>2</sub> DATA IS REPRESENTED BY DASHED LINES. VALUES ARE GIVEN AT SELECTED THICKNESSES OF CdS LAYER; 50NM AND 100NM. .... 108

FIGURE 8.1: STRUCTURE OF PEROVSKITE SOLAR CELL USED FOR OPTICAL MODELLING. 113

FIGURE 8.2: PERFORMANCE OF STANDARD SOLAR CELL. LIGHT REFLECTIONS AT THE GLASS SURFACE AND THE TRANSMISSION INTO ABSORBER LAYER HAVE BEEN MODELLED. .... 113

FIGURE 8.3: A 3D PLOT OF TRANSMITTANCE AGAINST TiO<sub>2</sub> LAYER THICKNESS AND WAVELENGTH. .... 114

FIGURE 8.4: A GRAPH SHOWING THE PHOTOCURRENT DENSITY [mA/cm<sup>2</sup>] DEPENDENCE ON THE THICKNESS OF THE TiO<sub>2</sub> LAYER [NM]. .... 114

FIGURE 8.5: DEPENDENCE OF THE PHOTOCURRENT DENSITY [mA/cm<sup>2</sup>] ON THE THICKNESS OF THE ITO LAYER [NM]. .... 116

FIGURE 8.6: REFLECTION LOSSES AS FUNCTION OF ITO THICKNESS..... 117

FIGURE 8.7: A 3D PLOT OF TRANSMITTANCE AGAINST AZO LAYER THICKNESS AND WAVELENGTH. .... 117

FIGURE 8.8: A GRAPH SHOWING THE PHOTOCURRENT [MA/CM <sup>2</sup> ] DEPENDENCE ON THE THICKNESS OF THE AZO LAYER [NM].....	118
FIGURE 8.9: REFLECTION LOSSES MODELLED FOR PEROVSKITE SOLAR CELLS AS A FUNCTION OF AZO THICKNESS.....	118
FIGURE 8.10: OPTICAL PROPERTIES OF PEROVSKITE SOLAR CELLS USING AZO (DOTTED LINES) AND FTO (SOLID LINES) AS TCO. ....	119
FIGURE 8.11: REFLECTION SPECTRA OF MAR-COATED GLASS DESIGNED FOR PEROVSKITE SOLAR CELLS.....	119

## LIST OF ABBREVIATIONS AND ACRONYMS

ARC – Anti-Reflection Coating

a- Si – Amorphous silicon

AZO – Aluminium doped Zinc Oxide

CdTe – Cadmium Telluride

CIGS – Copper indium gallium selenide

DI – de-ionised

HMDS – hexamethyldisilazane

HRT – High resistance transparent

ITO – Indium Tin Oxide

FTO – Fluorine doped Tin Oxide

MAR – Multilayer Anti-Reflection coating

Sol-gel – Solution gelation

TCO – Transparent Conducting Oxide

WAR – Weighted Average Reflection

WAT – Weighted Average Transmission

# 1 INTRODUCTION

As resources become more prevalent and easily accessible, humanities' ability to consume becomes greater, travel becomes faster, war becomes deadlier, and light production becomes more abundant. Because of this, energy consumption since the industrial revolution has exploded and there is little evidence to indicate this trend is nearing an end [1]. Within the last ten years, humankind's energy usage has exceeded the equivalent of 130 billion tons of oil. [2]. Fossil fuels continue to supply this growth in energy consumption in the form of coal, oil and gas, which are abundant and readily accessible with current technology. However, the use of fossil fuels has produced greenhouse gases, most notably CO<sub>2</sub>, in large volumes [1], [3], [4].

Due to solar re-emittance of incoming radiation back into space, the average surface temperature of the earth remains stable [3]. Since CO<sub>2</sub> absorbs light in the infra-red region of the electromagnetic spectrum, a greater percentage of the CO<sub>2</sub> present in the atmosphere leads to a greater percentage of incoming light initially being re-emitted back into space. However, a greater concentration of CO<sub>2</sub> means that light reaching the surface of the earth and re-emitting into the atmosphere has a lower chance of penetrating the atmosphere and escaping into space. Therefore, more light remains in the atmosphere or is reflected back to the surface of the earth more often. The net effect is that CO<sub>2</sub> reduces the heat flux from earth to space [1], [3], thus causing a warming effect.

It is extremely unlikely that humankind would seriously consider lowering energy usage in a way that limits entertainment, defence, transport, research, or private use (even that which is completely unnecessary). Considering the entirety of human history as

evidence, this is an unfortunate truth. Any attempts to curtail energy usage would be rightfully viewed as totalitarian and arbitrary. As the technology required to remove vast quantities of CO<sub>2</sub> from the atmosphere safely and easily does not exist, this leaves only one possible solution: the use of power sources that provide abundant energy, while producing minimal or no CO<sub>2</sub> [1]. Candidate non-fossil fuel sources include nuclear power, hydro, biomass, tidal, wind, geothermal, and solar.

## 1.1 The sun as a power source

Most energy sources on earth can be traced back to the sun; the notable exceptions are geothermal and nuclear. Assuming a solar constant of 1.361 kW/m<sup>2</sup>, around 174 PW is delivered to the atmosphere from solar radiation [3]. This energy source, after accounting for reflectance and absorption in the atmosphere, is 10 thousand times greater than the amount humanity uses over a given time period. Assuming even modest solar cell efficiencies leads to the conclusion that 0.1% of the earth's surface is all that is needed to produce enough energy to power all of civilisation [5]–[7]. Logistically, some issues may occur as much of the incoming solar energy is delivered between the tropics. Powering Reykjavik with a solar farm in Europe would prove challenging. Regardless, solar energy is an abundant and attractive resource.

In order to develop effective technologies to utilise solar power, one must have an understanding of the solar spectrum and how it varies depending on global position, environment, and altitude [5], [8], [9]. The spectrum at ground level differs from the spectrum at the top of the atmosphere due to absorption by gases in the atmosphere; most apparently water (particularly in Britain), but also ozone, dust, smog, aerosols, and CO<sub>2</sub>. A comparison of the spectrum at the top of the atmosphere and the average spectrum at ground level in Europe is shown in Figure 1.1.

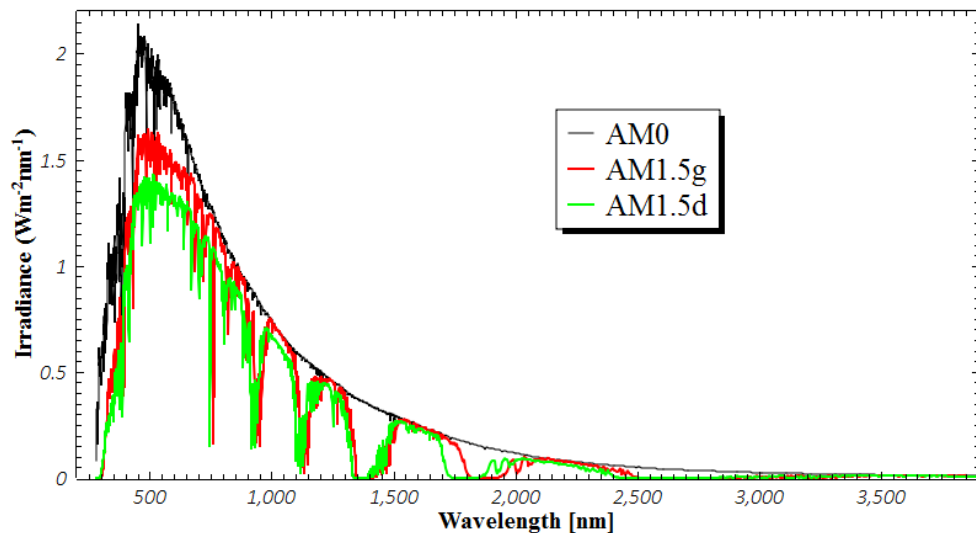


**Figure 1.1: A plot of the AM0 spectrum and the AM1.5 spectrum both direct (d) and global (g)[10].**

Because of all the parameters to consider, perfectly optimising any one solar installation for photon collection would be highly complex. As a result, systems are normally optimised for use in the standard Air Mass (AM) 1.5 spectrum [5], [9]. The AM system describes the amount of atmosphere light must penetrate in order to reach mean sea level at different points on the globe. When the sun is directly overhead, near the equator when incoming light is normal to the mean ground surface, the spectrum is labelled AM1, so named because the light has travelled through 1 atmosphere thickness of “Air Mass”.

For comparison, the spectrum at the top of the atmosphere is designated AM0 and AM1.5 is the spectrum after penetrating 1.5 times the thickness of the atmosphere assumed in the AM1 spectrum[9]. In the AM1.5 spectrum, the angle of incidence of light at ground level is  $\sim 48.2^\circ$ . The AM1.5 spectrum is therefore an accurate assumption for most areas where solar cells are likely to be installed, such as Europe, North America, Australia, southern Africa, and north Asia [5], [9].

## 1.2 Photovoltaics

The photovoltaic (PV) effect is the use of photons to excite electrons into an excited state within a material, so they are free to move. Under such circumstances an excited electron would usually collapse back to the original unexcited state, emitting the photon to conserve energy. However, in a PV device there is built in asymmetry, which ensures

the electron does not relax by removing the electron from the excitation site and feeding it into a circuit [11].

Solar cells typically utilise a p-n junction, which is comprised of a p-type and an n-type semiconductor in close proximity to one another, as to be touching. N-type and p-type semiconductors are doped with electrons and holes (electron vacancies) respectively [5]. In silicon solar cells, for example, doping is achieved through the addition of group 3 elements to produce p-type silicon, and doped with group 5 elements to produce n-type silicon [5], [12]. When such materials are in contact, holes diffuse from the p-type material to the n-type and electrons from the n-type diffuse into the p-type. As the p-type material bleeds holes to the n-type, a net negative charge builds in the p-type material. In the same way, a net positive charge builds in the n-type material due to loss of electrons to the p-type. This area in the cell is known as the 'space charge region' and it results in a potential difference and the creation of an electromagnetic field. Electrons can be excited by impinging photons to create electron-hole pairs, these pairs can then be separated from each other by the field in the space charge region and removed from the system to do work [13]. The amount of energy a photon requires to excite an electron from the valence band into the conduction band is known as the band-gap. The band-gap is dependent on the absorbing material and is usually between 1.0 and 1.65eV. This energy range corresponds to a wavelength range of ~750nm (perovskite) ~1200nm (crystalline silicon). The difference between the Fermi levels in the p-type and n-type semiconductors within the stack determines the open circuit voltage ( $V_{oc}$ ) of a solar cell. The short circuit current of a device ( $I_{sc}$ ) is the current through the cell when the voltage is zero, such as when the cell has short-circuited.  $I_{sc}$  is related to the short circuit current density ( $J_{sc}$ ). The cell cannot operate under either open circuit or short circuit conditions. These electronic properties of PV technologies are highly dependent on the band-gap; a low band gap device will suffer from a low  $V_{oc}$ , but will have a large amount of photons capable of exciting electrons across the band-gap. High band-gap devices have a high  $V_{oc}$  and have less available photons of a suitable energy for electron excitation, resulting in a low  $I_{sc}$ . As a result,  $I_{sc}$  and  $V_{oc}$  are negatively correlated. This relationship limits the theoretical maximum efficiencies of PV technologies, as ideally both parameters should be as high as possible. The ideal band-gap for a single-junction cell, for producing maximum efficiency, has been estimated to be between 1.4 and 1.5eV [14].

There are two main types of p-n junction, hetero and homo-junctions. If both the n-type and p-type semiconductors are doped with the opposite charge but maintain the same material, the resulting p-n junction is considered a homo-junction. A diagram of the band structure of a p-n junction and a visual representation of a space charge region is shown in Figure 1.2. If the materials differ completely then the p-n junction is considered a hetero-junction.

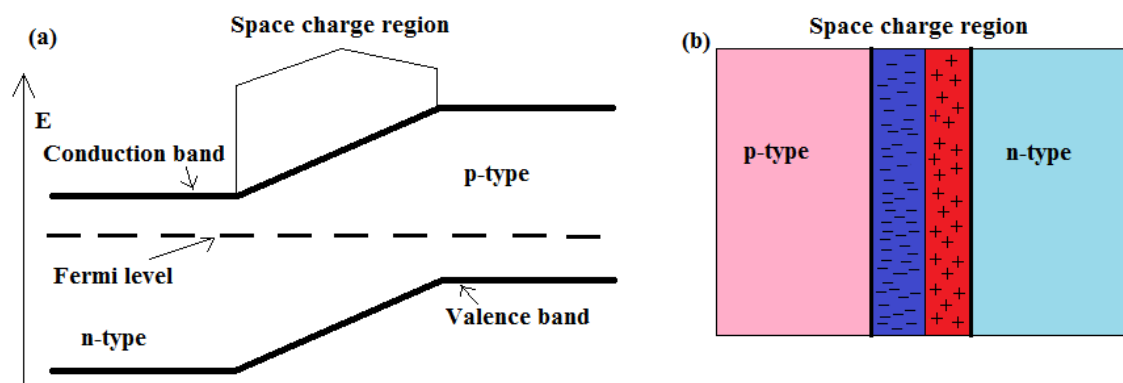


**Figure 1.2:** (a) A diagram of the band structure of a simple p-n junction, and (b) a visual representation of the p-n junction.

### 1.3 Photovoltaic technologies

The majority of solar cells bought in the worldwide PV market are Silicon PV. Mono and multi-crystalline silicon accounted for just over 90% of all power generated through PV [15]. The competing thin-film technology with the largest market share is CdTe, at 5% of total PV energy generation [15]. There are many reasons for the popularity of silicon: as an element in the earth's crust it is abundant, and is already used in the manufacturing of computer chips and other devices. Because of this, silicon has already been mined in large amounts. Silicon is also convenient as it can be doped to be both an n-type and p-type semiconductor, and can therefore form a homo-junction, negating the need for a second material.

In silicon semiconductors, in momentum space, the highest point in the valence band is not directly below the lowest point in the conduction band. As a result, light is not readily absorbed in silicon because interaction with a phonon is necessary to successfully excite an electron into the conduction band from the valence band. Therefore, the absorber in silicon solar cells (or any technology based on a material with an indirect band-gap) must have a thick absorbing layer. Materials with direct band-gaps can have much thinner absorbing layers [16]. Total absorption is achieved with

~300 $\mu\text{m}$  and high purity silicon is needed for the manufacture of highly efficient cells. However, once electrons are in the conduction band re-absorption is just as difficult as the initial excitation. As a result, silicon PV is both inexpensive and efficient, which partly explains silicon PV's stranglehold on the PV market. Multi-crystalline silicon has lower production costs when compared to mono-crystalline, but the addition of grain boundaries within the absorber creates opportunities for recombination of excited electrons, and thus results in a less efficient solar cell.

Crystalline silicon devices have a theoretical maximum efficiency of 30%. The highest recorded efficiency of a mono-crystalline silicon solar cell in the AM1.5 spectrum is 26.3% [17] and silicon PV is nearing the maximum possible cell efficiency of 29.8% [18]. The record efficiency for mono-crystalline silicon is high compared to other technologies, such as multi-crystalline silicon (20.8%), and thin film solar cells like Cu(InGa)Se<sub>2</sub> (22.6%), and CdTe (22.1%)[17]. Considering the cost of maintenance and installation, in addition to the cost of the panel proper, the total cost of mono-crystalline silicon solar panels is ~\$0.37/Wp. In contrast, multi-crystalline is slightly cheaper due to lower manufacturing costs at ~\$0.35/Wp [19]. The price of PV has been reduced by a factor of 4 in just a few short years. As silicon is expensive to produce and reaching theoretical maximum efficiency, it is important to research alternative PV technologies to further reduce the cost per watt.

Thin film solar cells, such as CdTe, offer high efficiencies- but unlike silicon cells, thin film technologies can be produced quickly and, thanks to a direct band-gap, offer low material usage for near complete photon absorption. The most prominent company to adopt CdTe as a commercial product is First Solar, Inc. As previously stated, CdTe devices offer efficiencies of 22.0% over a small area under standard test conditions. The highest recorded efficiency outside of standard test conditions is 22.1% [20], recorded by First Solar, Inc [21].

The CdTe solar cell is a thin film stack with a total thickness typically ~3 $\mu\text{m}$ . The standard CdTe stack consists of (from the bottom to the top): a back contact, the cadmium telluride (CdTe) absorbing layer, the cadmium sulphide (CdS) window layer, a buffer layer, and a transparent conducting oxide (TCO) layer. All of which is beneath a glass superstrate. For commercial modules, the layers are deposited on to a low-cost soda lime glass substrate pre-coated with a TCO. CdTe has a direct band-gap, so unlike silicon solar cells, photons are absorbed and directly excite electrons into the conduction band, allowing for much thinner absorption layers in the CdTe stack compared to

traditional silicon cells. Additionally, the band-gap of cadmium telluride is near ideal and therefore has very high maximum theoretical efficiency. As CdTe is a p-type absorber and has a high electron affinity, CdTe devices require very high work function materials as back contacts. Unfortunately no common metals have work functions high enough [22]. This necessitates the use of expensive metals or doped common materials, such as NiO.

## 1.4 Scope of this thesis

PV technologies have a clear role in providing significant power to meet global demand. PV can be applied in many situations and is a clean and renewable source of energy, growing cheaper year-on-year. This consistent price drop is beneficial because, ultimately, PV energy needs to be as cheap as possible in order to compete with fossil fuel energy sources. Ideally, alternative energy should be so cheap it should not be considered an alternative at all, but the logical economic choice, no government incentivisations needed. To achieve cheaper solar panels, one or both of two things must be improved: the efficiency of the panels must be raised, or the cost of production must be lowered.

The air-glass interface at the front of any mainstream PV technology is responsible for ~4.23% loss of light into the cell. One way to improve the efficiency of PV technologies is by applying an anti-reflection coating (ARC) to reduce the amount of light reflected at said interface. The different kinds of ARCs and the physics behind the application of these coatings are described in full in Chapter 2, in addition to the effect of hydrophobic coatings on ARC performance. Chapter 3 describes the various deposition techniques involved in the deposition of both single layer and multilayer ARCs. Chapters 4 and 5 consider the application of a multilayer anti-reflection coating to different PV technologies, with a focus on CdTe. ARCs applied to solar panels need to withstand all standard tests that assess the long-term survivability of solar panels. Durability testing and information regarding adhesion for ARCs can be found in Chapter 6.

Another route to improve solar cell efficiency is through the optical optimisation of the layers within the cell. Destructive interference can be achieved between different layers within the stack to improve transmission to the absorber. In order to find optimal beneficial interference, the behaviour of light was predicted by the transfer matrix method, outlined in chapter 2, when varying the structure of PV technologies. Models

of the CdTe and perovskite stacks used to optimise each system optically are presented in Chapter 7.

## 2 ANTI-REFLECTION COATINGS

Solar cell efficiencies can be increased by reducing optical losses, such as reflection and absorption. One of the most apparent sources of reflection loss in any PV system is the air-glass interface at the front of the module. Reflection reduces the photon flux into the cell by ~4.3%. The application of an anti-reflective coating (ARCs) addresses some of this loss of potential photocurrent.

### 2.1 Design principles

To design effective ARCs it is necessary to understand the nature of reflection. Reflection occurs at the interface between 2 materials of varying refractive indices. The percentage of incident light reflected depends on the angle of incidence at the interface, as well as the polarity of the light and the magnitude of the difference between the refractive indices of the respective layers. Reflectance can be described by the following equations derived from the Fresnel equations [23]:

$$R_s = \left| \frac{n_1 \cos \theta_i - n_2 \cos \theta_t}{n_1 \cos \theta_i + n_2 \cos \theta_t} \right|^2 \quad (2.1)$$

$$R_p = \left| \frac{(n_1 \cos \theta_t - n_2 \cos \theta_i)}{n_1 \cos \theta_t + n_2 \cos \theta_i} \right|^2 \quad (2.2)$$

Where  $n_1$  is the refractive index of the entrance medium,  $n_2$  is the refractive index of the exit medium,  $\theta_i$  is the angle of incidence, and  $\theta_t$  is the angle of transmitted light. (2.1 and (2.2) represent s-polarised light and p-polarised light respectively.

Sunlight is unpolarised (an even mixture of different polarisations of light), so for the purposes of solar cell application, or any outdoor application, the following equation holds:

$$R_T = \frac{1}{2}(R_s + R_p) \quad (2.3)$$

Where  $R_T$  is the total reflection at the material interface; due to conservation of energy, any non-reflected light is transmitted; that is transmission equals 1 minus the reflection.

## 2.2 The transfer matrix method

It is possible to calculate the reflection and transmission of light through optical systems of varying complexity in several different ways [24]. It is common in thin film optics to calculate reflection by employing matrix methods. As the equations governing the propagation of the electric field are linear [25], and the tangential electric field is continuous at media interfaces [26], structures with distinct parallel-plane material interfaces and isotropic and homogenous layers can be described as a series of  $2 \times 2$  layer matrices and interface matrices [24], [27]. Layer and interface matrices can be combined into a single ‘transfer matrix’ which takes both absorption and reflection into consideration. Transfer matrices can be resolved to find the transmission and reflection coefficient for an incident electric field.

According to Leif A. A. Pettersson, each layer in the system is denoted by a “j” value ( $j=1, 2, 3\dots$ ), and has a thickness of value  $d_j$  [24]. The optical properties of a material are governed by the complex index of refraction  $\mathbf{n}_j = n_j + ik_j$ , where  $n_j$  is the refractive index of material “j” and  $k_j$  is the magnitude of the imaginary absorption coefficient. This refractive index of a system can be described in terms of a complex dielectric function and is a function of the energy of incoming light. The field (which includes light) within the material can be resolved into 2 components, one travelling in the positive “x” direction and one travelling in the negative direction. Each interface within an optical system can be described by the Fresnel complex reflection and transmission in an interface matrix, shown in equation (2.5).

$$\begin{bmatrix} \widehat{E}_j^+ \\ \widehat{E}_j^- \end{bmatrix} = I_{ab} \begin{bmatrix} \widehat{E}_k^+ \\ \widehat{E}_k^- \end{bmatrix} \quad (2.4)$$

$$I_{jk} = \frac{1}{t_{jk}} \begin{bmatrix} 1 & r_{jk} \\ r_{jk} & 1 \end{bmatrix} \quad (2.5)$$

Where  $r_{jk}$  represents the Fresnel complex reflection and  $t_{jk}$  represents the Fresnel complex transmission, at the interface between material “j” and “k”.  $\widehat{E}_j^+$  and  $\widehat{E}_j^-$  are the electrical field of the light propagating in the positive and negative x-direction through the material labelled ‘j’, respectively. When the electric field of the incoming light is perpendicular to the plane of incidence, the reflection and transmission coefficients are represented by equations (2.6) and (2.7) respectively.

$$r_{jk} = \frac{q_j - q_k}{q_j + q_k} \quad (2.6)$$

$$t_{jk} = \frac{2q_j}{q_j + q_k} \quad (2.7)$$

When the electric field of the incoming light is parallel to the plane of incidence, the reflection and transmission coefficients are described by equations (2.8) and (2.9).

$$r_{jk} = \frac{\mathbf{n}_k^2 q_j - \mathbf{n}_j^2 q_k}{\mathbf{n}_k^2 q_j + \mathbf{n}_j^2 q_k} \quad (2.8)$$

$$t_{jk} = \frac{2\mathbf{n}_j \mathbf{n}_k q_j}{\mathbf{n}_k^2 q_j + \mathbf{n}_j^2 q_k} \quad (2.9)$$

Where  $q_j = \mathbf{n}_j \cos(\varphi_j)$  and  $\varphi_j$  is the angle of refraction within layer ‘j’. The interface matrix does not describe the behaviour of light through the bulk of the material, so to describe many layered systems layer matrices must be used. The layer matrix of any given layer ‘j’, is described by equation (2.10).

$$L_j = \begin{bmatrix} e^{-i\zeta_j d_j} & 0 \\ 0 & e^{i\zeta_j d_j} \end{bmatrix} \quad (2.10)$$

where

$$\zeta_j = \frac{2\pi}{\lambda} q_j \quad (2.11)$$

Where  $\zeta_j d_j$  is the phase thickness of the layer and “ $\lambda$ ” is the wavelength of the light traversing the layer. Similar to a single interface matrix, the behaviour of light though

the entire system— from the entrance material to the exit material— can be described by the combination of layer and interface matrices. The resultant matrix is known as the transfer matrix, defined in equation (2.12).

$$\mathbf{S} = \begin{bmatrix} S_{11} & S_{12} \\ S_{21} & S_{22} \end{bmatrix} = \left( \prod_{n=1}^m I_{(n-1)n} L_n \right) \cdot I_{m(m+1)} \quad (2.12)$$

The complex reflection and transmission coefficients for the entire system can be expressed in terms of the matrix elements of the transfer matrix shown in equation (2.12), so:

$$r = \frac{\widehat{E}_0^-}{\widehat{E}_0^+} = \frac{S_{21}}{S_{11}} \quad (2.13)$$

$$t = \frac{\widehat{E}_{m+1}^+}{\widehat{E}_0^+} = \frac{1}{S_{11}} \quad (2.14)$$

Using this technique, it is possible to calculate the internal electric field in any given layer within a system by considering the transfer matrices for the system either side of the layer of interest. So the transfer matrix can be written:

$$\begin{bmatrix} \widehat{E}_0^+ \\ \widehat{E}_0^- \end{bmatrix} = S'_j \begin{bmatrix} \widehat{E}_j^+ \\ \widehat{E}_j^- \end{bmatrix} \quad (2.15)$$

$$\mathbf{S}'_j = \begin{bmatrix} S'_{j11} & S'_{j12} \\ S'_{j21} & S'_{j22} \end{bmatrix} = \left( \prod_{n=1}^{j-1} I_{(n-1)n} L_n \right) \cdot I_{(j-1)j} \quad (2.16)$$

Where  $\widehat{E}_j^+$  and  $\widehat{E}_j^-$  denotes the electric field within layer  $j$  at the  $(j-1)$  to  $j$  layer boundary, in the positive and negative x-direction respectively. For the system after the  $j$ -layer the partial transfer matrix is:

$$\begin{bmatrix} \widehat{E}_j^+ \\ \widehat{E}_j^- \end{bmatrix} = S''_j \begin{bmatrix} \widehat{E}_{m+1}^+ \\ \widehat{E}_{m+1}^- \end{bmatrix} \quad (2.17)$$

$$\mathbf{S}''_j = \begin{bmatrix} S''_{j11} & S''_{j12} \\ S''_{j21} & S''_{j22} \end{bmatrix} = \left( \prod_{n=j+1}^m I_{(n-1)n} L_n \right) \cdot I_{m(m+1)} \quad (2.18)$$

Where  $\widehat{E}_j^+$  and  $\widehat{E}_j^-$  are the electric field inside the  $j$ -layer at the  $j$  to  $(j+1)$  layer boundary, in the positive and negative x-direction respectively. The Fresnel complex

reflection and transmission coefficients in terms of matrix elements are then defined as such:

$$r'_j = \frac{S'_{j21}}{S'_{j11}} \quad (2.19)$$

$$t'_j = \frac{1}{S'_{j11}} \quad (2.20)$$

$$r''_j = \frac{S''_{j21}}{S''_{j11}} \quad (2.21)$$

$$t''_j = \frac{1}{S''_{j11}} \quad (2.22)$$

From the combination of equations (2.13)-(2.22) we can derive the internal transfer coefficient for the electric field in the positive x-direction at the  $(j-1)$  to  $j$  interface. Shown below:

$$t_j^+ = \frac{\widehat{E}_j^+}{\widehat{E}_0^+} = \frac{t'_j}{1 - r'_{j-1} r''_j \cdot e^{i2\zeta_j d_j}} \quad (2.23)$$

And the electric field in the negative x-direction at the same interface:

$$t_j^- = \frac{\widehat{E}_j^-}{\widehat{E}_0^-} = \frac{t'_j r''_j \cdot e^{i2\zeta_j d_j}}{1 - r'_{j-1} r''_j \cdot e^{i2\zeta_j d_j}} = t'_j r''_j \cdot e^{i2\zeta_j d_j} \quad (2.24)$$

From equations (2.23) and (2.24), the entire electric field inside a given layer within the system can be derived [24], [27]. In terms of distance from the  $(j-1)$  to  $j$  boundary, “ $x$ ”, and the electric field of the incident plane, “ $\widehat{E}_0^+$ ”, in the region  $0 \leq x \leq d_j$ , the electric field is given by:

$$\begin{aligned} \widehat{E}_j(x) &= \widehat{E}_j^+(x) + \widehat{E}_j^-(x) && \text{Using} \\ &= [t_j^+ e^{i\zeta_j x} + t_j^- e^{-i\zeta_j x}] \widehat{E}_0^+ && \text{the} \\ &= t_j^+ [e^{i\zeta_j x} + r''_j e^{-i\zeta_j (2d_j - x)}] \widehat{E}_0^+ && \text{transfer} \\ &&& \text{matrix} \\ &&& \text{method,} \end{aligned} \quad (2.25)$$

the transmission of photons through a stratified system can be calculated. This is useful

for predicting the effectiveness of ARCs (particularly multi-layer ARCs) due to their complexity. Another application is calculating the transmission to the absorbing layer of a solar cell.

The transfer matrix method has been implemented fully in a software package, 'Essential MacLeod'[28], which has been used to calculate the transmission and reflection of optical systems throughout this thesis. Single layer AR

Different techniques can be implemented to create effective ARC designs. The simplest ARC is a single layer index matching coating. Index matching involves a coating with an intermediate refractive index with a value between the refractive index of glass and air. Single layer coatings create an antireflection effect through a combination of two separate effects.

Independent of the wavelength of light and the thickness of the coating, small changes in refractive index will always result in less reflection than that of one large step change in refractive index. If, the refractive index gradually changed from the refractive index of one medium to the refractive index of the other medium at a material boundary, there would be no reflection at all. The ideal refractive index of a coating to maximise transmission was first derived by Lord Rayleigh[29]. The ideal refractive index for a single-layer ARC, with clearly defined step changes in refractive index, is the square root of the refractive index of the exit medium multiplied by the square root of the refractive index of the entry medium [30]:

$$n_c = \sqrt{n_1 n_2} \quad (2.26)$$

Where  $n_c$  is the refractive index of the coating,  $n_1$  is the refractive index of the entrance medium, and  $n_2$  is the refractive index of the exit medium. In the case of an air-glass interface, assuming the refractive index of glass is  $\sim 1.5$ , the ideal refractive index for a single layer ARC is  $\sim 1.22$ .

The second form of single layer antireflection is achieved through the manipulation of different reflections to create destructive interference, between the glass-coating interface and the coating-air interface. As shown in Figure 2.1, the ideal thickness of interference based single layer coatings is a quarter the wavelength of incident light. As the thickness of a coating can only be a quarter of a single wavelength, the effectiveness of single layer ARCs is greatest around a single wavelength. Additionally, as the path length through the single layer ARC depends on the path taken through the coating, destructive interference is most effective at a single angle of incidence.

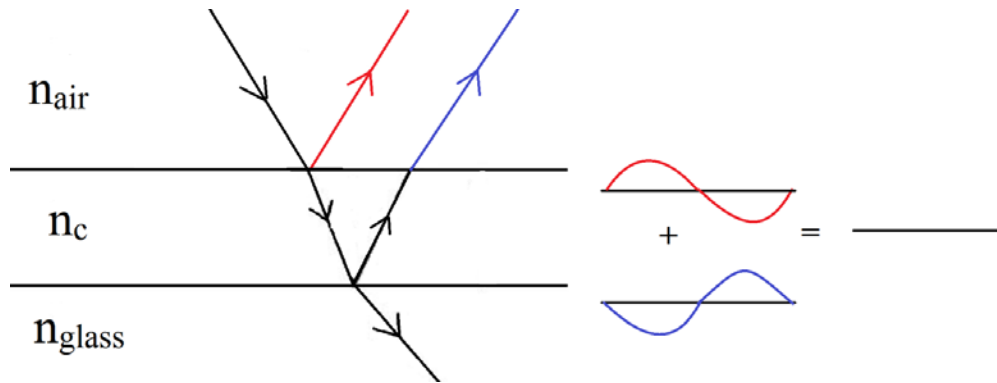


**Figure 2.1: Destructive interference in a single layer AR coating**

The lowest refractive index of any solid is magnesium fluoride ( $\text{MgF}_2$ ) with a refractive index of 1.32 at 550nm on the electromagnetic spectrum [31]. The use of a quarter wavelength thick layer of  $\text{MgF}_2$  provides an effective ARC on glass.

An alternative material to  $\text{MgF}_2$  for single layer ARCs is sol-gel processed porous silica coatings. In porous coatings, materials of lower refractive index, usually air, are introduced into the coating to artificially reduce the refractive index of the coating. The refractive index of sol-gel ARCs can be as low as 1.08 [32]. However as sol-gel coatings are so highly tuneable the refractive index of sol-gel ARCs can be chosen to fit the requirements based on the entrance and exit media at the interface. This brings the refractive index closer to the ideal index of 1.22.  $\text{SiO}_2$  has a low refractive index. Although materials with lower refractive indices exist (such as the previously mentioned  $\text{MgF}_2$ ),  $\text{SiO}_2$  retains greater mechanical strength as void percentage is increased than competing materials of lower refractive indices.

Sol-gel derived coatings are an attractive choice for many reasons. Sol-gel ARCs have a high manufacturing speed and low production costs. It is also possible to use many different precursor materials [33]–[35]. Due to these characteristics, sol-gel is suitable for mass production. An attractive property of sol-gel coatings is that they can possess a variety of useful functions simultaneously [36], such as hydrophobicity and scratch resistance. However, improving the coating adhesion or hydrophobicity usually has an adverse effect on the optical properties of the coating.

Porous silica ( $\text{SiO}_2$ ) is the most commonly used material in single layer ARCs deposited through the sol-gel method. It is also possible to control many aspects of sol-gel deposition, providing greater control over the dimensions of microstructures in sol-gel surfaces. This includes surface area, void radius, and volume [37].

## 2.3 Multilayer AR

Multilayer AR (MAR) coatings, similarly to interference based single layer ARCs, use the interference of light at medium boundaries to create destructive interference. This reduces reflection at the air-glass interface, thereby improving transmission through the surface. A schematic diagram of a typical MAR coating design is shown in Figure 2.2. The structure of the MAR alternates between high and low refractive index materials. The low index material used is almost always thin film silicon dioxide ( $\text{SiO}_2$ ) with a refractive index of  $\sim 1.46$  at 550nm. There are several candidate materials for the high index layers, including zirconium dioxide ( $\text{ZrO}_2 \sim 2.23$ ), titanium dioxide ( $\text{TiO}_2 \sim 2.23$ ), and hafnium oxide ( $\text{HfO}_2 \sim 1.93$ ). The thicknesses of the layers in the design are manipulated to cause destructive interference on a scale similar to the wavelength range of the light being captured. Consequently, the thicknesses of layers, when changed slightly, can have a considerable effect on the effectiveness of the MAR coating. Therefore, deposition methods capable of reliably producing flat, smooth surfaces of deposited material, ion beam sputtering[38], ion assisted electron beam evaporation[38] and magnetron sputtering [39]), are necessary when manufacturing MAR coatings.

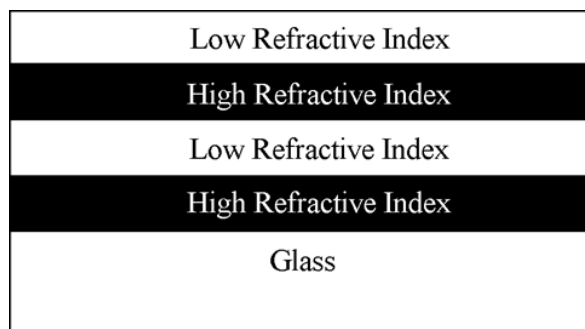


**Figure 2.2: Schematic diagram of a generic 4-layer MAR coating on glass.**

The greater the number of layers in an MAR design, the greater the reduction in reflection. However, a more layered design means more stages in the deposition process (which means greater cost and manufacturing time), and a thicker, possibly less stable coating.

## 2.4 Textured AR Coatings

Surfaces can be modified through etching or deposition to produce 3-dimensional pyramidal structures, grooves, or other structures to produce an anti-reflection effect [40]. Interestingly, when considering the light of wavelengths larger, smaller, or of

equivalent size to the surface structures, the reflection reduction is explained by different mechanisms.

Large wavelengths interact with the surface as if it were a gradient of refractive index. Reflection is therefore reduced considerably across a broad range of angle of incidence. Wavelengths of light smaller than the structure size are reflected in many directions as they impinge on surfaces on the structures[41]. Most paths lead into the desired medium, and traces leading back to the source are comparably rare when compared to smooth bare glass. Reflection in the case of smaller wavelengths can be calculated using ray tracing, as the system utilises simple optical geometry in these conditions[42].

## 2.5 Addition of Hydrophobic Coating

ARCs are sometimes susceptible to water ingress, which lowers the effectiveness of the AR by changing the refractive index of the coating. A coating that holds water is also more likely to degrade faster over time from erosion and mineral deposition. The application of an additional hydrophobic layer can address water related weathering in ARCs susceptible to water ingress. Hydrophobic coatings can be modified porous silica, which has some AR properties [43], [44]. Alternatively, a very thin layer of a material detrimental to the AR properties of the system can be used. The layer must be very thin to minimise interference with the ARC. Layers 100 times smaller than the wavelength of light being transmitted through the system have a negligible effect on the transmission. For example, if the ARC is designed to increase the transmission of light in the wavelength range of 350-850nm, it would be beneficial to deposit a hydrophobic layer below 3.5nm in thickness. Therefore, it is possible to add a small hydrophobic material with poor optical properties without destroying the effectiveness of the ARC. Texturing the ARC can lead to hydrophobic properties, potentially removing the need for an additional layer for certain ARC technologies [45].

# 3 DEPOSITION TECHNIQUES FOR THIN FILMS

The deposition of anti-reflective coatings and the internal layers of PV technologies can be achieved in a myriad of ways, including physical and chemical methods. The properties of a thin film are determined by the deposition method used in production. When choosing an appropriate deposition technique used to produce the layers of PV technologies, the opto-electrical properties of the film must be taken into consideration. In the case of AR coatings, both the optical properties and the mechanical durability of the coatings need to be considered. Chemical methods are predominately performed in atmospheric conditions and involve chemical precursors reacting to produce the desired material to be deposited. Chemical vapour deposition (CVD) can be used to deposit the transparent conducting oxide (TCO) layer of PV technologies. This deposition is performed at the end of the glass production line while the substrate is still hot [46]. The heat aids in the deposition of the TCO as the deposited materials need to be in the vapour phase to adhere successfully to the surface of the substrate. An alternative chemical method similar to CVD is spray pyrolysis. The main difference between the two deposition methods is the phase of the deposited matter; in contrast to the vapour phase of CVD, spray pyrolysis deposits liquid phase precursors. Chemical methods have a history of poor control over the chemical composition of produced films due to precursor impurities and because they are performed in atmospheric conditions. However these difficulties have been overcome in the certain cases, such as Pilkington

TEC glass [46]. Screen printing, electrospray and doctor blading are other atmospheric techniques less relevant to this thesis [5], [47], [48].

An alternative form of deposition commonly used in the manufacturing of thin film PV technologies (such as CdTe and CIGS) is physical deposition techniques, performed in a vacuum. Physical deposition techniques provide films of greater and more consistent quality in comparison to chemical deposition techniques. This is because physical deposition takes place in a vacuum. For example, in the case of sputtering, the chamber is pumped down to a high vacuum and then an inert gas is introduced to the system, raising the pressure to a low vacuum of ~5mbar. This means that the only possible impurities in the deposited films come from contamination of the sample, system, or the target. When taking precaution and correctly sourcing targets, these sources of contamination can be easily minimised. Other physical deposition techniques include: thermal and electron beam evaporation, ion assisted electron beam evaporation, ion beam sputtering, close space sublimation (CSS), Vapour Transport Deposition (VTD), and magnetron sputtering [49]–[54].

### 3.1 Thin film deposition methods

#### 3.1.1 Reactive Magnetron Sputtering

In this work, magnetron sputtering was used as a deposition method of thin film multi-layered AR Coatings. Sputtering is a process involving the bombardment of a solid target with energetic gaseous ions to eject material from the surface of the target [55]. After the material is ejected, it travels typically ~10cm where it condenses as a thin film on a substrate, see Figure 3.1.

In magnetron sputtering, the target is a cathode and the substrate is an anode, typically grounded or electrically floated. The target is held at a negative potential, a voltage pulse is used to induce ionisation in the argon atoms and a plasma is then formed. This creates a potential difference between the negatively charged target and the positively charged argon ions, and accelerates the ions towards the target for bombardment. As atoms and fragments are ejected from the target, secondary electrons are also emitted from the surface. Such electrons are confined to the surface of the target by a magnetic field, preventing damage to the target from high energy electrons. Free electrons on the surface collide with argon atoms, creating argon ions and sustaining the plasma. The electrons can also collide with argon ions and form a neutral atom. In the event of an ion

accepting a free electron, a photon is emitted which results in the glow of the plasma. Theoretically, when sputtering is performed in a perfect vacuum the ejected particles travel in a straight line to the substrate. The particles then condense onto the substrate, which is commonly glass but can be any material needed. The direct high energy impact of sputtered material onto condensed material on the substrate can cause resputtering of the deposited material from the substrate. When an inert gas is introduced into the system, the ejected matter interacts more with the gas in the chamber. The particles therefore arrive at the substrate, or on the sides of the vacuum chamber, after a random walk with reduced kinetic energy. The percentage of particles that make a direct impact with the substrate and the percentage that interact with the vacuum chamber gas can be controlled by manipulating the pressure within the chamber, effectively changing the mean free path of particles through the gas, this in turn allows the deposition energy to be manipulated. Ideally, the energetic particles used for bombardment should have a similar atomic weight to those in the target material, allowing for efficient transfer of kinetic energy.

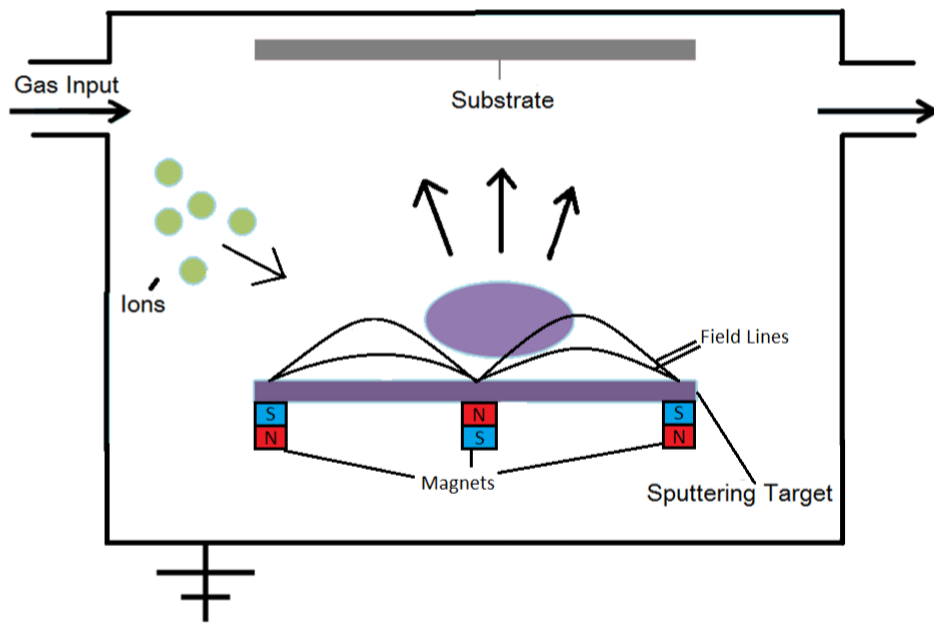


**Figure 3.1: Schematic diagram of the apparatus used in magnetron sputtering, showing magnets and magnetic field lines.**

Reactive magnetron sputtering involves the introduction of a reactive gas [56], such as oxygen or nitrogen, into the deposition plasma typically present during magnetron sputtering. The added gas becomes chemically active during the deposition process through excitation by the existing plasma. The reactive gas then reacts with the surface of the target, altering its chemical makeup before sputtering. The gas also reacts with

the growing film on the surface of the substrate. This allows for composition control of deposited films, allowing for the production of nitrides, carbides, and, in the case of this work, oxides[57]. The reactive sputtering process allows for the control of the structure and chemical composition of thin films.

## 3.2 Solution Gelation

An option for AR production is solution gelation (sol-gel) processing. Sol-gel involves the mixtures of a solution that, through an applicatory process, goes through a gelation process on a substrate, forming a coating. Sol-gel has many possible precursor materials [35], [58], [59], has a high manufacturing speed, and has a low production cost. Due to these characteristics, sol-gel is suitable for mass production. Sol-gel coatings can have a variety of functions simultaneously [36]. Porous silica ( $\text{SiO}_2$ ) is the most common material used in single layer AR coatings deposited through the sol-gel method.  $\text{SiO}_2$  has a low refractive index ( $n < 1.45$ ) and although materials with lower refractive indices exist, (e.g. magnesium fluoride)  $\text{SiO}_2$  retains greater mechanical strength as void (air pocket within the film) percentage is increased, than competing materials of lower refractive indices. It is also possible to control many aspects of sol-gel deposition, which provides greater control over the dimensions of microstructures in sol-gel surfaces, such as surface area, void radius and volume [37].

Due to the vast array of possible Sol-Gel solutions, the characteristics of sol-gel coatings vary greatly. Many different AR coatings have useful properties, such as hydrophobicity and antistaticity [60]–[62]. The reflectance, transmittance, and absorption of coatings, when well designed, depend on the intended use of the coating. Given a suitably designed coating, Sol-Gel can reduce reflectance at air-glass interfaces to about 0.6% for many wavelength ranges. AR coatings with sufficient adhesion and mechanical strength have been produced on both glass and plastic [63].

### 3.2.1 Dip coating

In this work, dip coating was used to deposit basic sol-gel coatings for comparison against commercial sol-gel, and high vacuum, physical deposition techniques. Dip coating has three distinct stages: Substrate immersion in the solution to be deposited, substrate removal from the solution, and a curing stage, as can be seen in Figure 3.2. The thickness of the resulting film is controlled by several competing forces; drag upwards on the solution from the substrate as it moves upwards, the gravitational force

downwards, the surface tension of the solution, viscosity, ambient temperature, humidity, and the disjoining and conjoining pressure of the solution.

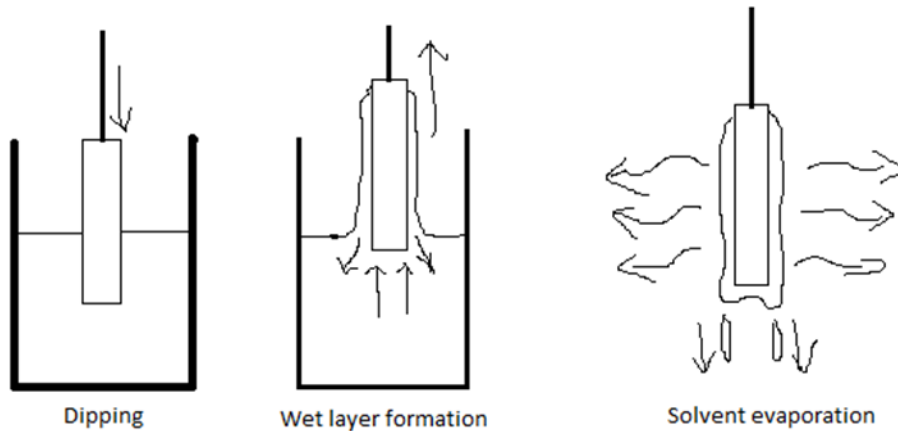


**Figure 3.2: The stages of the dip coating process: The substrate is dipped into a sol, the substrate is then removed from the sol forming a wet layer coating, the coating is then left to dry and condense into a gel.**

In cases where the solutions viscosity is low and the substrate is removed at a sufficiently slow speed the resulting coating has a thickness ( $h$ ) that can be expressed by the equation below:

$$h = \frac{0.94(\eta U)^{\frac{2}{3}}}{\gamma_{LV}^{\frac{1}{6}}(\rho g)^{\frac{1}{2}}} \quad (3.1)$$

Where  $\eta$  is the solution viscosity,  $U$  is the substrate withdrawal speed,  $\rho$  is the density of the solution and  $\gamma_{LV}$  is the liquid-vapour surface tension. This equation was derived by Landau and Levich and verified by Brinker and Scherer [37]. The accuracy of this equation in the context of acid catalysed silicate sol was confirmed to be in accordance with experimental results by James and Strawbridge [64].

The dip coating method is the most common technique used in sol-gel thin film deposition. The ubiquity of the dip coating method can be explained by the flexibility of the procedure. Substrates can be of many different shapes and sizes— the only requirement of a substrate is that it can be dipped into the solution. Dip coating can coat substrates on the order of square meters in surface area. Substrates can be dipped while other substrates are concurrently lifted from the solution, or run in batches that enter and leave the solution simultaneously.

### 3.2.2 Spin coating

Spin coating involves applying an excess of the solution to slowly spinning or stationary substrate. The substrate is then rotated at an accelerated pace, pushing the deposited material to the outer edge of the substrate by means of centrifugal force, where it collects and leaves the substrate. As the film gets thinner, the rate of thickness change decreases. The film thins further during spin down and then through evaporation and solidification as any solutes and particulates concentrate. A diagram of this can be seen in Figure 3.3 below.

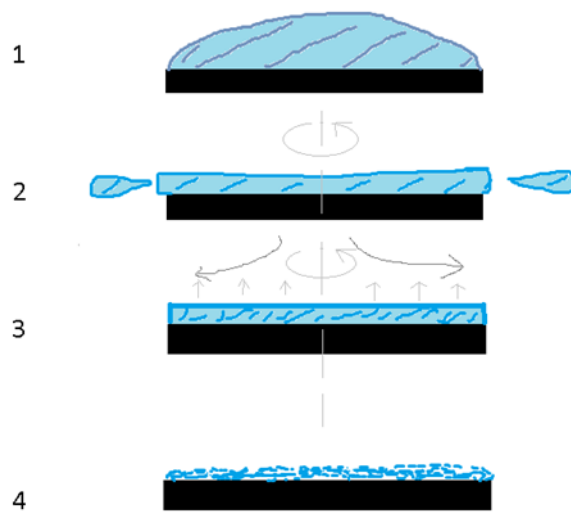


**Figure 3.3: The spin coating process: 1. An excess of sol is applied to the substrate, 2. The substrate is spun and excess sol is removed by way of the centrifugal force, 3. The coating thins further as the substrate spins slower and stops through evaporation, 4. The coating is deposited and condensed after annealing.**

Damon and Kodak modelled the film thickness of a sample deposited by spin coating to simply be [65]:

$$h = \frac{kc_0^2}{f^{\frac{1}{2}}} \quad (3.2)$$

Where  $h$  is the thickness of the coating, on a spinner platform rotation rate of  $f$ , with an initial solids concentration of the solution. To give greater detail, the films thickness is determined predominantly by the following equations during the rotation of the substrate (spinoff). As shown by Meyerhofer [65].

$$h_{\text{spinoff}} = \left[ \frac{3\mu e}{2\rho_{A0}\omega^2} \right]^{\frac{1}{3}} \quad (3.3)$$

$$t_{\text{spinoff}} = \frac{3\mu}{4\rho_A\omega^2} \left[ \frac{1}{h_{\text{spinoff}}^2} - \frac{1}{h_0^2} \right] \quad (3.4)$$

Where  $h_{\text{spinoff}}$  is the resulting height at any point during spinoff without an evaporation phase, and  $t_{\text{spinoff}}$  is the time needed to attain the desired film thickness.  $\rho_A$  is the density of volatile solvent within the solution  $\rho_{A0}$  is the initial density, and  $e$  is a constant evaporation rate,  $\omega$  is the angular velocity of the substrate, and  $\mu$  is the solutions viscosity. After the spinoff stage, the evaporation stage begins. After evaporation is complete, a given film's thickness is determined by the following equations:

$$h_{\text{final}} = \left[ 1 - \frac{\rho_{A0}}{\rho_A} \right] \left[ \frac{3\mu e}{2\rho_{A0}\omega^2} \right]^{\frac{1}{3}} \quad (3.5)$$

$$t_{\text{final}} = t_{\text{spinoff}} + h_{\text{spinoff}} \frac{\rho_{A0}}{e\rho_A} \quad (3.6)$$

Using equations (3.3)(3.6 allows for the deposition of films of particular thicknesses in a standardised predictable manner, with little waste in comparison to dip coating. Dip coating requires the substrate to be placed into a volume of deposition solution, whereas spin coating only requires the amount of solution necessary to cover the platform.

### 3.2.3 Meniscus coating

The meniscus coating method involves forcing the coating solution through a porous metal applicator tube, resulting in a thin film over the surface of the applicator. The applicator tube is then lowered to the substrate until the film is only just touching the substrate, forming a meniscus. The substrate is then moved relative to the applicator and a liquid film is deposited and, after drying, a gelled film. The main benefit to this method of deposition is the minimal wastage of coating solution. The thicknesses of films deposited using the meniscus coating method are dependent on the substrates translation rate, suspension viscosity, geometry, and film flowrate [66].

Both meniscus and spin coating are attractive deposition methods and have benefits, such as solution efficiency and precision. However, due to constraints in available

equipment and time, only dip coated chemically deposited coatings are investigated in this thesis.

### 3.3 Industrial Sol-Gel coatings

Both chemical and physical coatings were deposited for this work, specifically dip coating method and reactive magnetron sputtering. In chapter 6, a comparison is drawn between the mechanical and anti-weathering properties of MAR coatings deposited by magnetron sputtering, and single layer porous silica AR deposited through sol-gel processes (such as dip and spin coating). However, the dip coated basic sol-gel coatings created for this work were highly friable. Therefore for this comparison, ‘AR1’ from Prinz Optic<sup>®</sup>, a single layer AR that utilises an inverted porous silica structure, has been used as a commercial bench mark. This section describes the science and deposition of coatings like AR1 that use the method created by DSM<sup>®</sup>.

#### 3.3.1 Porous Silica and Nano Spheres

Voids within a coating help to reduce the refractive index of any given layer. As the lowest refractive index of any known solid material is in the region of 1.35[67], implementing air pockets in the coating allows the refractive index to more closely approach that of air. This results in a reduction of reflection at the coating – air interface.

The refractive index of silicon can be varied greatly through oxidation and the inclusion of voids within the film. Unfortunately, achieving useful refractive indices, such as  $n=1.3$ , has proven difficult. The initial porosity in a pure silica film before oxidation (that, when oxidised, results in a silica film of  $n=1.3$ ) is around 70%. This high percentage of voids meant that early attempts at low refractive index films resulted in mechanically weak samples. In addition, the production of lower porosity films has proved more difficult than anticipated, as oxidation processes close smaller voids. This further complicates the production and marketing of viable Sol-Gel AR coatings [68].

Theoretically, the resulting refractive index of any given film of certain porosity can be calculated using equation (3.7 seen below):

$$n_c = (\varphi_p n_p^2 + (1 - \varphi_p) n_a^2)^{\frac{1}{2}}, \quad \frac{d_p}{\lambda} \ll 1 \quad (3.7)$$

Where  $n_c$  is the refractive index of the coating,  $n_p$  is the refractive index of the particles making up the bulk of the film,  $n_a$  is the refractive index of the void gas (most likely

air),  $\phi_p$  is the volume fraction of particles in the coating,  $d_p$  is the maximal particle diameter, and  $\lambda$  is the wavelength of light relevant to the refractive indices.  $(d_p)/\lambda \ll 1$  is a condition on the equation, and if not met renders the equations inaccurate. This is because the voids are of the same order of magnitude as the wavelength of the incident light, the amorphous refractive index interfaces cause diffraction and therefore increase the length that light must travel through the coating, resulting in greater absorption [68]. Silica based coatings have shown to reduce reflection by up to 88%, by mixing different sized silica particles in the sol.

The manipulation of refractive index by the application of voids within a film was first patented in 1949 by American Optical Corp. The patent's title describes the idea as: "[A] Method of producing thin micro-porous silica coatings having reflection reducing characteristics and the articles so coated". The proposal to apply this technology to glass to create a low reflectance glass was first patented by Nicoll Frederick H in 1951[69]. After the concept of a chemically derived porous antireflective coating was first suggested, it took 50 years before the first commercially available AR using the technology was marketed. Low academic interest, low resistance to weathering, and difficulties in coating method scaling, coating adhesion, and mechanical stability contributed to this delay [70].

### 3.3.2 DSM Hard Coat

In 2003, DSM filed a patent for a newly developed coating technology. This new method results in coatings that are mechanically robust and durable in interior and exterior environments [71]. This technology has been applied to museum display glass to reduce unwanted glare and to provide greater visibility of displayed items. DSM's display glass has been commercially available under the product name Claryl since 2007. The coating method utilises silica nano spheres to support the voids so they do not close during processing; and low refractive index silicon resins ( $n < 1.35$ ) to produce antireflective films. The structure of hard coats can be seen in Figure 3.4.

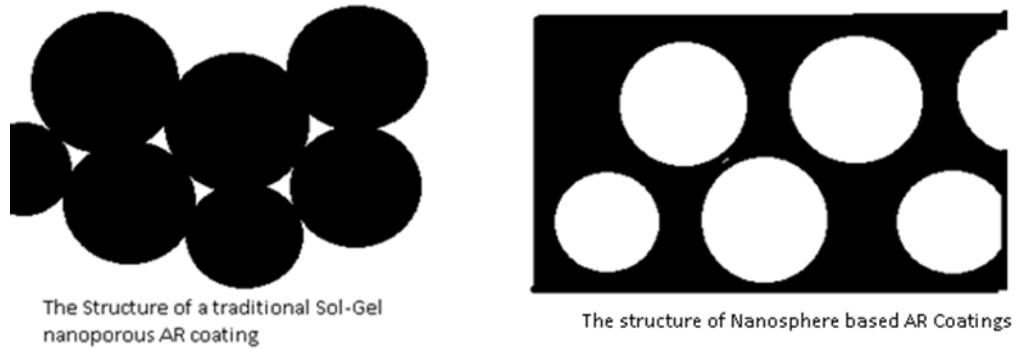


**Figure 3.4: Comparison of a traditional nano-porous sol-gel coating and a silica shell/resin coating.**

Traditionally, sol-gel anti-reflective coatings have consisted of masses of nanoparticles in amorphous shapes. By manipulating the ratio of abundance between specific compounds within the layer, it is possible to grade the refractive index of subsequent layers using traditional sol-gel methods. Coatings produced through the method developed by DSM implement silica shells, which have hollow cores and gaps between the shells which are filled with a silica binder. The performance of such coatings as reported by DSM, using khepricoat as an example can be seen in Figure 3.5. This effectively inverts the traditional structure, allowing the top of the coating to have fewer bumps and therefore lower surface area. This also allows the coating to retain structural integrity at greater void percentages.

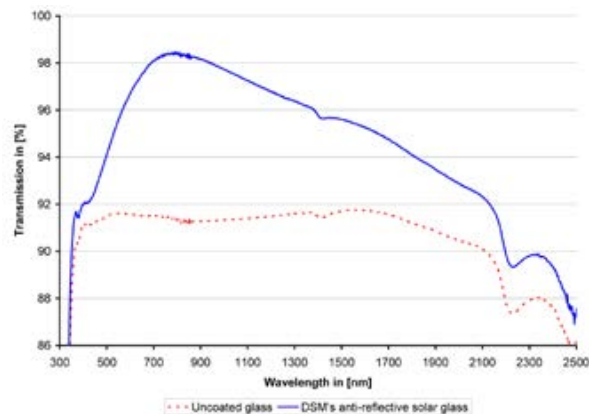


**Figure 3.5 The transmittance of uncoated glass compared to the transmittance of Khepricoat coated glass between 300 and 2500nm wavelength. Taken from Innovation at DSM: State of the Art Single Layer Anti-Reflective Coatings for Solar Cell Cover Glass [72].**

Khepricoat has undergone several tests to establish that the coating is robust. The coatings have undergone the following tests specifically: abrasion resistance (EN 1096-2), damp-heat (IEC 61215), humidity-freeze (IEC 61215), and thermal cycling (IEC 61215). The samples withstood all tests with minimal reduction in optical efficiency resulting in a loss of about 0.5% of the total inward flux. Damp heat tests were carried out at PI Berlin and showed a consistent transmission gain regardless of the duration of the test up to 1500 hours.

### 3.4 Glass substrate preparation

Soda-lime glass (SLG) substrates are used often throughout this thesis, as a deposition substrate and as a standard material used for modelling the glass layer within solar stacks. The SLG substrates (Menzel-Gläser, Germany) used to deposit both physical and sol-gel AR coatings, were 1mm thick with very low iron content. This gives the glass a transmission of over 90% across the usable PV wavelength range. Before deposition, the substrates were scrubbed and then cleaned in an ultrasonic bath with a 50%-50% solution of de-ionised (DI) water and isopropyl alcohol. The substrates were then removed from the solution, cleaned, and stored in DI water until ready for deposition. A pure nitrogen gun was used to dry the samples before deposition. This method gives exceptionally clean substrates fit for deposition, resulting in high quality films. The samples of AR1, a commercially available sol-gel AR coating from Prinz Optics, were prepared in a separate laboratory and so the cleaning method for these samples is unknown. However, it is the authors' opinion that the samples were prepared in such a manner to give the best quality films.

# 4 APPLICATION OF ANTI-REFLECTION COATINGS TO THIN FILM CdTe

CdTe has a band-gap that is close to the ideal ( $\sim 1.45\text{eV}$ ) for photovoltaic devices which, after considering absorption in the glass substrate, results in a wavelength range of 350nm-850nm. This places the useable wavelength range of CdTe at a midpoint compared to other PV technologies. In this chapter, anti-reflection coatings fabricated using reactive sputtering and sol-gel techniques both designed for thin film CdTe devices are examined and compared optically.

The first part of this study examines the effectiveness and optimisation of MARs for CdTe devices. The coatings are initially modelled and optimised. Once materials are chosen and the coating is optimised, the coatings are deposited using reactive magnetron sputtering and their performance measured using spectrophotometry. The second part of this study considers the performance of basic porous silicon sol-gel and commercially available sol-gel coatings for CdTe devices. These are deposited through dip coating and a sol-gel technique respectively.

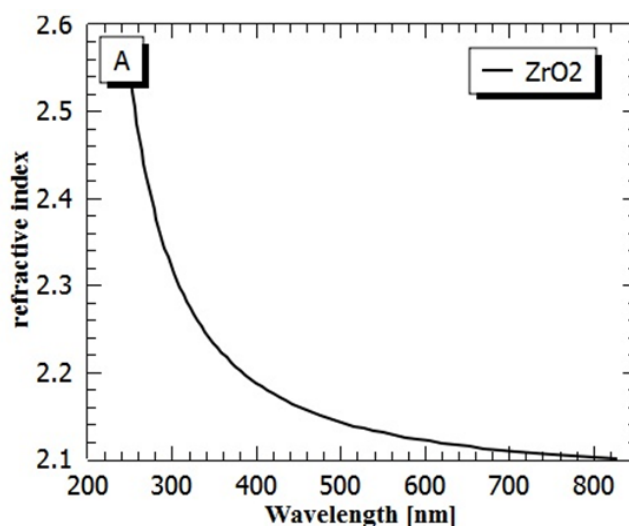
## 4.1 Thin film MAR coatings for CdTe

Thin Film CdTe, like all PV modules, experience reflection losses due to the difference between the refractive index of the glass superstrate and the air. The front surface reflections are responsible for losses of over 4% of the incident light. The reflection

losses can be reduced by the application of an anti-reflection (AR) coating. The simplest option is to deposit a single layer refractive index, matching AR with a material with a low refractive index.  $\text{MgF}_2$  has a low refractive index ( $n=1.34$  at  $550\text{nm}$ )[31]. A thin film of  $\text{MgF}_2$  provides an effective AR coating over a narrow range of wavelengths. However,  $\text{MgF}_2$  is a soft material and suitable for laboratory use only. Porous silica is another single layer option, although long-term stability can be an issue for this type of coating due to potential problems with water ingress[73]. Multilayer anti-reflection coating (MAR) is a more complex design, but is effective over a broader wavelength range. The design of a MAR is based on high/low refractive index material pairs and does not require a material with a refractive index lower than glass.

#### 4.1.1 Coating Design Principles

The design of a broadband anti-reflection coating uses a combination of materials with low and high refractive index. The low index material is always thin film Silicon dioxide ( $\text{SiO}_2$ ), with a refractive index of  $\sim 1.46$  at  $550\text{nm}$ . A wide choice of materials is available for the high index thin films, which are listed in Table 4.1 with their important optical and mechanical properties. The choice of high index material depends on the application, but there is often a compromise between optical properties, durability, and cost. As solar modules must last a long time in the outdoors, possibly in extreme weather conditions, durability is essential. For this reason, we have chosen to use zirconium dioxide ( $\text{ZrO}_2$ ) for fabrication of MAR coatings, because it has exceptional scratch resistance and is relatively abundant and cost effective.. The refractive index dispersion of thin films of zirconia and silica used for the MAR coating deposition is shown in Figure 4.1. The dispersion was measured by spectroscopic ellipsometry.



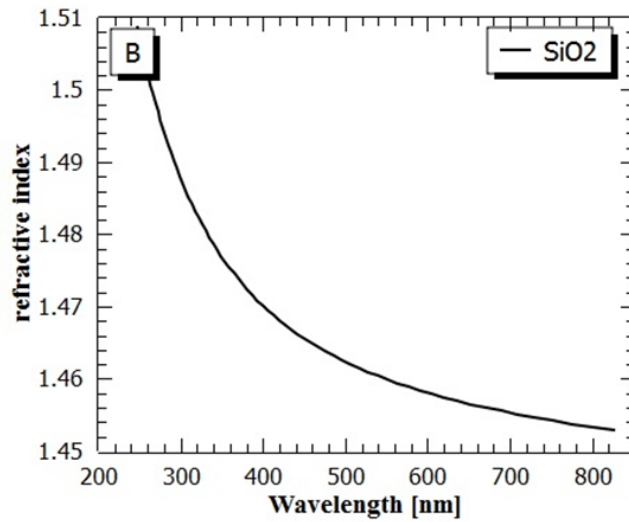


**Figure 4.1: The refractive index dispersion of (A) ZrO<sub>2</sub> and (B) SiO<sub>2</sub> used for the MAR deposition.**

However, titanium dioxide (TiO<sub>2</sub>) and other candidate materials are also considered here from a purely modelling standpoint. The optical and thermal properties of these materials are presented in Table 4.1.

**Table 4.1: The optical constants and important mechanical properties of candidate high index materials for use in MARs.**

Material	Coefficient of thermal expansion ( $10^{-6}/C$ )	Hardness Vickers (GPa)	– Refractive index (n) at 550nm	Extinction Coefficient (k) at 550nm
Silicon Dioxide (SiO <sub>2</sub> )	0.4 [74]	~12.4 [75]	1.46	0
Zirconium Dioxide (ZrO <sub>2</sub> )	13.5 [76]	~13.0 [77]	2.23	0
Titanium Dioxide-anatase (TiO <sub>2</sub> -a)	8.6 [78]	~11.0 [75]	2.49	0
Titanium Dioxide -rutile (TiO <sub>2</sub> -r)	8.4 [78]	~12.0 [79]	2.61	0
Hafnium-Oxide (HfO <sub>2</sub> )	5.9 [80]	~14.7 [81]	1.93	0
Tantalum Pentoxide (Ta <sub>2</sub> O <sub>5</sub> )	3.0 [82]	~13.7 [81]	2.15	0
Niobium Pentoxide (Nb <sub>2</sub> O <sub>5</sub> )	~3.0 (similar to Ta <sub>2</sub> O <sub>5</sub> )[82]	~15 [80]	2.32	0

The MAR requires accurate control of each layer thickness to maximize destructive interference and minimize the overall reflection. The coatings are designed using optical constants derived from spectroscopic ellipsometry measurements. The MAR coatings are designed to minimize average reflection over the specific spectral range corresponding to the PV absorber band gap. In the case of a CdTe absorber, the band gap is ~1.45eV which corresponds to a wavelength of ~855nm but CdTe begins to absorb light less efficiently at the higher wavelengths. Since glass begins to absorb at 350nm, the wavelength range used by CdTe devices is between 350nm and 850nm. In comparison, a single layer design optimizes at a single wavelength to create a ‘V-coat’ AR. MAR coatings are broadband and their use results in a much greater reduction in average reflection. The bandwidth can be tuned for the different band gaps used in various PV absorbers by controlling the thickness of the layers within the MAR[83].

The coating layer thicknesses were optimised to reduce reflection using the optical modelling package ‘Essential Macleod’, developed by the Thin Film Center Inc[28]. This package uses the transfer matrix method to calculate transmittance and reflectance in optical coating systems. The transfer matrix method allows an optical system that is a sum of optical matrices to be considered as a single matrix: a ‘transfer matrix,’ as outlined in chapter 2. The thickness of each layer in the four layer design was optimised to lower the weighted average reflection (WAR) from the glass-air interface. A WAR is the weighted average of reflection of all solar photons across the wavelength range of interest. To accurately calculate the WAR from bare glass and MAR coated glass, the relative flux of photons in the solar spectrum must be taken into consideration at each point in the 350nm to 850nm range. In addition, the wavelengths must be given appropriate weightings in accordance with the AM1.5 solar spectrum[83]. The WAR is described by equation (4.1) which shows the product of the AM1.5G solar spectrum ( $\Phi$ ) and the reflectance (R), integrated over the defined wavelength range ( $\lambda$ ).

$$WAR(\lambda_{max}, \lambda_{min}) = \frac{\int_{\lambda_{min}}^{\lambda_{max}} \Phi \cdot R d\lambda}{\int_{\lambda_{min}}^{\lambda_{max}} R d\lambda} \quad (4.1)$$

MAR coatings vary in the number of layers used. When designing MAR coatings, the addition of extra layers results in lower reflection. However, in terms of reflection reduction, the difference between a 6 layer and a 4 layer design is much less than the difference between a 4 layer and a 2 layer design. Evaluating the benefits of greater reduction in reflection against the greater material costs and increased coating complexity, a 4 layer design is optimum for the 350nm-850nm wavelength range.

#### 4.1.2 Modelled Coatings

Although  $ZrO_2$  was chosen as the high refractive index material for MAR coatings studied in this work, alternative materials were considered. Modelled designs using  $TiO_2$ ,  $HfO_2$ ,  $Nb_2O_5$ , and  $Ta_2O_5$  coatings are presented in this section.  $SiO_2/ZrO_2$  are presented in section 4.1.3, with modelled and measured reflectance shown in Figure 4.12.

When considering the glass substrate, the modelled spectrum of the reflection from a 1mm thick soda lime glass substrate is shown in Figure 4.2. The solid black curve shows the reflection when both (front and back) interfaces are considered; the total

incident energy loss is ~8%. The dotted red curve is the reflection characteristic of only the front glass/air surface, which accounts for ~4% energy loss of incident light.

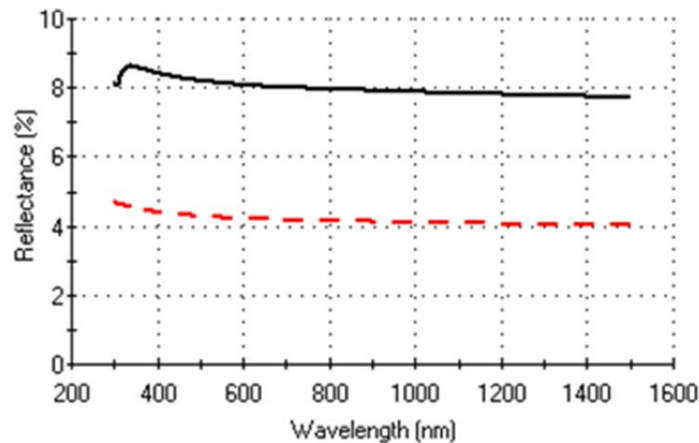


**Figure 4.2: The modelled reflection spectra of an uncoated 1mm glass surface. The black solid curve models the reflection from both the front and back glass surfaces. The red dotted curve represents the front surface losses only.**

The refractive indices of the modelled but not deposited MAR high refractive materials are shown in Figure 4.3. Figure 4.3 shows that the shape of dispersion between the materials varies considerably.  $\text{Nb}_2\text{O}_5$  has an exceptionally high refractive index but underperforms in modelled coatings. The materials that perform the best in an MAR coating ( $\text{HfO}_2$  and  $\text{Ta}_2\text{O}_5$ ) have a comparatively low refractive index across the entire usable wavelength range. In contrast, the refractive indices of  $\text{Nb}_2\text{O}_5$  and  $\text{TiO}_2$  increase between 500nm and 400nm. This compromises the effectiveness of the coating by making light of differing wavelengths difficult to accommodate.

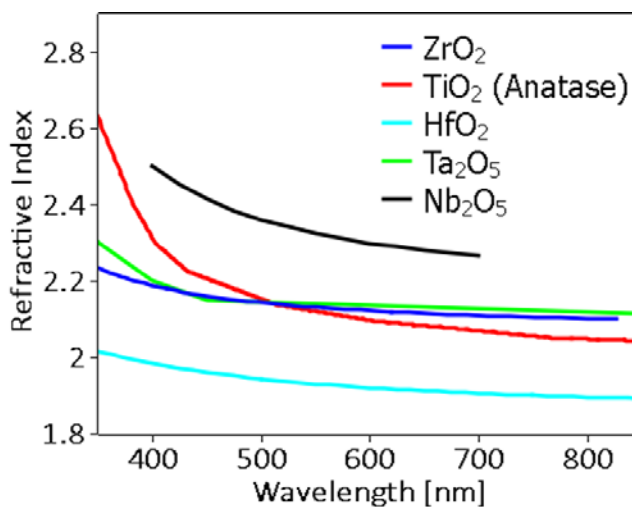


**Figure 4.3: The refractive index dispersions of high refractive index material candidates,  $\text{Nb}_2\text{O}_5$ ,  $\text{TiO}_2$ ,  $\text{Ta}_2\text{O}_5$ , and  $\text{HfO}_2$ .**

#### 4.1.2.1 Titanium Dioxide (TiO<sub>2</sub>)

A MAR coating designed for use on CdTe devices with a TiO<sub>2</sub> high refractive index layer is presented in Table 4.2. Overall, the coating is ~226nm thick. The design reduced the weighted average reflectance (WAR) at the glass interface to 1.92% from 4.22%.

**Table 4.2: The structure of a modelled MAR coating optimised for use on CdTe Solar cells, where TiO<sub>2</sub> is the high refractive index material.**

Layer	Designed d [nm]
SiO <sub>2</sub>	78.99
TiO <sub>2</sub>	115.94
SiO <sub>2</sub>	11.41
TiO <sub>2</sub>	19.53

The modelled reflection across the usable wavelength range of CdTe solar cells is shown in Figure 4.4. Figure 4.4 shows how the optimal design for TiO<sub>2</sub> MARs gives greater reflectance than bare glass when considering wavelengths greater than 800nm. However, this is compensated through reduction in reflection in other areas of the spectrum.

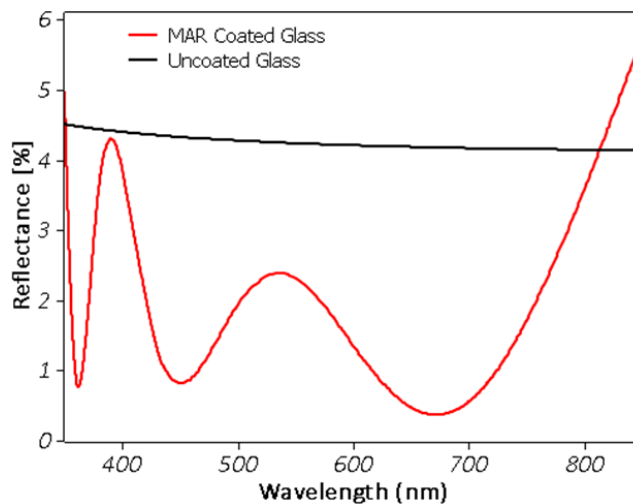


**Figure 4.4: Reflection at air glass interface with and without a SiO<sub>2</sub>/TiO<sub>2</sub> MAR coating.**

#### 4.1.2.2 Hafnium Dioxide (HfO<sub>2</sub>)

An MAR coating designed for use on CdTe devices with a HfO<sub>2</sub> high refractive index layer is presented in Table 4.3. Overall the coating is slightly thicker than that of TiO<sub>2</sub> at a total thickness of ~264nm. However, since the use of HfO<sub>2</sub> gives a greater reduction in WAR, the WAR at the glass interface is reduced to just 1.17%.

**Table 4.3: The structure of a modelled MAR coating optimised for use on CdTe Solar cells, where HfO<sub>2</sub> is the high refractive index material.**

Layer	Designed d [nm]
SiO <sub>2</sub>	85.22
TiO <sub>2</sub>	133.88
SiO <sub>2</sub>	23.04
TiO <sub>2</sub>	21.68

The modelled reflection across the usable wavelength range of CdTe solar cells is shown in Figure 4.5. The optimal design for HfO<sub>2</sub> results in a reduction of reflectance across the entire usable wavelength range of CdTe solar cells.

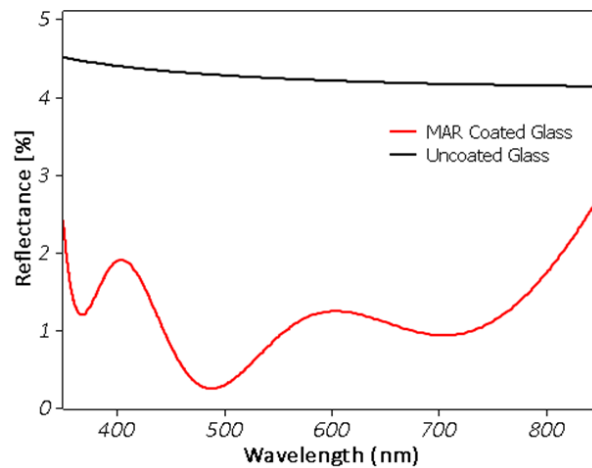


**Figure 4.5: Reflection at air /glass interface with and without a SiO<sub>2</sub>/HfO<sub>2</sub> MAR coating.**

#### 4.1.2.3 Tantalum Pentoxide (Ta<sub>2</sub>O<sub>5</sub>)

An MAR coating designed for use on CdTe devices with a Ta<sub>2</sub>O<sub>5</sub> high refractive index layer is presented in Table 4.4. Overall, the coating is slightly thicker than that of TiO<sub>2</sub>, but less so than HfO<sub>2</sub>, at a total thickness of ~244nm. Similarly, the use of Ta<sub>2</sub>O<sub>5</sub> gives a greater reduction in WAR than TiO<sub>2</sub>, but less than HfO<sub>2</sub> –the WAR at the glass interface is reduced to just 1.35%.

**Table 4.4: The structure of a modelled MAR coating optimised for use on CdTe Solar cells, where Ta<sub>2</sub>O<sub>5</sub> is the high refractive index material.**

Layer	Designed d [nm]
SiO <sub>2</sub>	83.56
Ta <sub>2</sub> O <sub>5</sub>	120.74
SiO <sub>2</sub>	18.21
Ta <sub>2</sub> O <sub>5</sub>	21.49

The modelled reflection across the usable wavelength range of CdTe solar cells is shown in Figure 4.6. The optimal design for Ta<sub>2</sub>O<sub>5</sub> results in a reduction of reflectance across the entire usable wavelength range of CdTe solar cells.

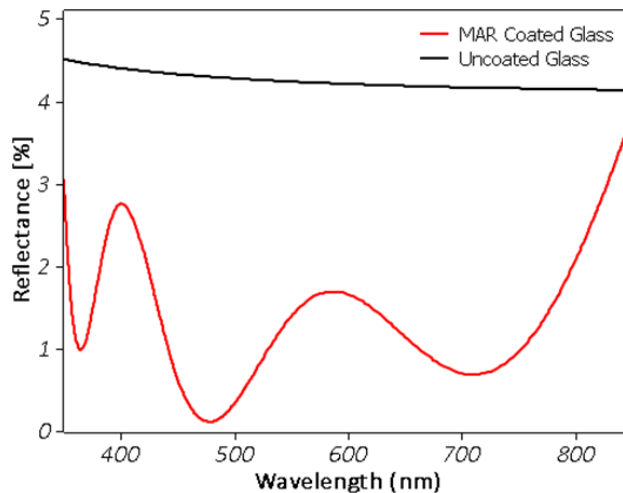


**Figure 4.6: Reflection at air glass interface with and without a SiO<sub>2</sub>/Ta<sub>2</sub>O<sub>5</sub> MAR coating.**

#### 4.1.2.4 Niobium Pentoxide (Nb<sub>2</sub>O<sub>5</sub>)

An MAR coating designed for use on CdTe devices with a Nb<sub>2</sub>O<sub>5</sub> high refractive index layer is presented in Table 4.5. Overall, the coating is ~233nm, only TiO<sub>2</sub> based coatings are thinner. Nb<sub>2</sub>O<sub>5</sub> gives a greater reduction in WAR than TiO<sub>2</sub>, to a lesser extent than Ta<sub>2</sub>O<sub>5</sub> and HfO<sub>2</sub>. The WAR at the glass interface is reduced to 1.80%.

**Table 4.5: The structure of a modelled MAR coating optimised for use on CdTe Solar cells, where Nb<sub>2</sub>O<sub>5</sub> is the high refractive index material.**

Layer	Designed d [nm]
SiO <sub>2</sub>	83.48
Nb <sub>2</sub> O <sub>5</sub>	111.69
SiO <sub>2</sub>	16.96
Nb <sub>2</sub> O <sub>5</sub>	20.45

The modelled reflection across the usable wavelength range of CdTe solar cells is shown in Figure 4.7. The optimal design for Nb<sub>2</sub>O<sub>5</sub> results in a reduction of reflectance up to ~820nm.

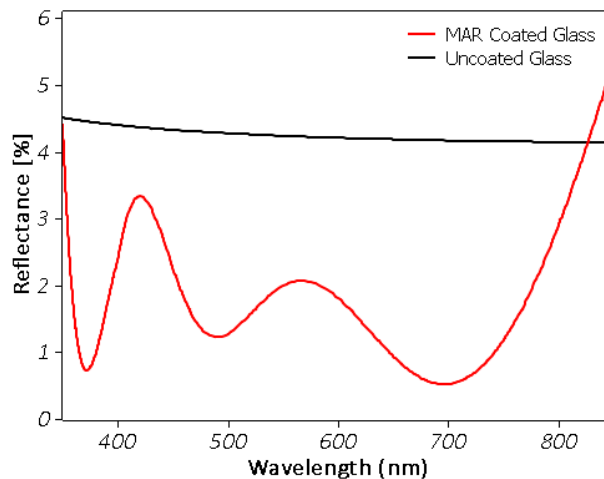


**Figure 4.7: Reflection at air glass interface with and without a SiO<sub>2</sub>/Nb<sub>2</sub>O<sub>5</sub> MAR coating.**

#### 4.1.2.5 Dependence on angle

Using different high refractive index materials changes the amount of light reflected from the air-glass interface at all angles. A side by side comparison of the coatings presented so far is shown in Figure 4.8. This point on the wavelength range was chosen across all coatings for a fair comparison. It is highly active in the am1.5 solar spectrum, and it is relatively close to a minimum for all coatings.

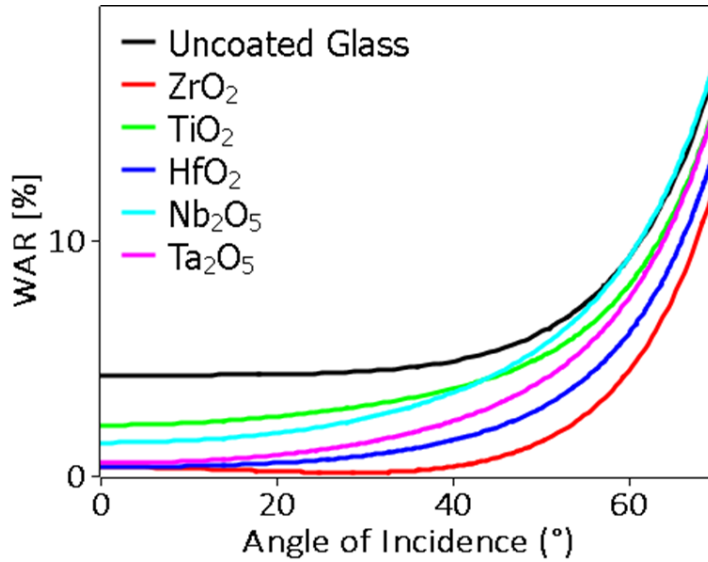


**Figure 4.8: Comparison of angular dependence of MAR coatings of varying high refractive index material.**

This data may initially seem unserviceable since it is unfair to compare only the wavelength 550nm across all the coatings. However, this data shows that the Nb<sub>2</sub>O<sub>5</sub> coating becomes drastically less effective as the angle of incidence is varied away from 0° (at ~60° it is better to have no coating at all than to have an Nb<sub>2</sub>O<sub>5</sub> MAR). It is also worth noting that HfO<sub>2</sub> performs very well in a MAR coating although not as good as ZrO<sub>2</sub>.

#### 4.1.3 Deposited SiO<sub>2</sub>/ZrO<sub>2</sub> Coatings for thin film CdTe photovoltaics

SiO<sub>2</sub>/ZrO<sub>2</sub> MAR coatings were modelled and optimised using Essential MacLeod and then deposited using magnetron sputtering (outlined in section 4.1.3.1) to test the effectiveness of the coatings. In this section the optical and electrical results of MAR application are presented.

Optical Macleod has a variety of optimisation techniques; in this work ‘simplex’ was used. Simplex involves changing the thickness of layers in the system by small increments and recording the reflectance/transmittance after each thickness. If the thickness change results in an increase to transmission the thickness is kept and the process begins again. Once incremental change results in greater reflectance, lower transmission (or any other undesired effect, depending on the application) the operation ceases. In this work the program was run for a maximum of 10000 iterations, it updated the thickness of the coating if a 0.00001% improvement was recorded, and the thickness was varied by 0.01nm at each instance. Although this program finds near perfect

designs for optical optimisation, it does not take into consideration the solar spectrum when considering gains. As such further gains were obtained by calculating the WAR or WAT of the system and changing the thicknesses manually to find WAT maxima and WAR minima.

Figure 4.9 shows the detailed structure of the MAR design on top of a simple CdTe PV stack. The decision to have a 4 layer design and ZrO<sub>2</sub> as the high refractive index material leads to a relatively thin multilayer stack (~277nm) which is affordable in material usage and fabrication time.

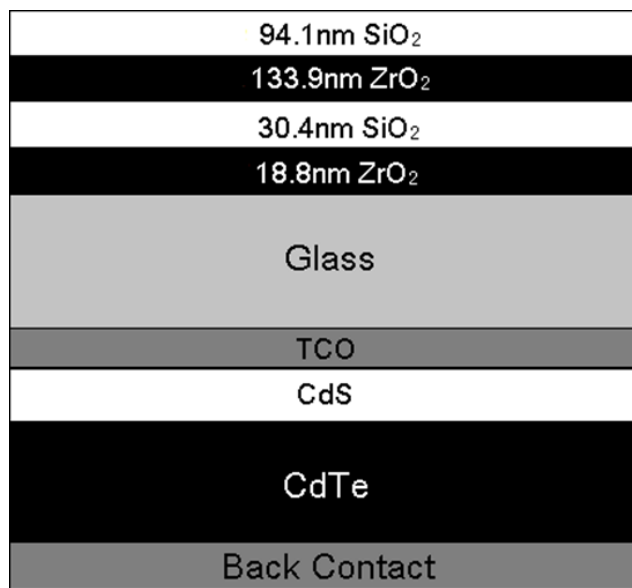


**Figure 4.9:** A schematic diagram of the MAR coating design on a CdTe device, the refractive index of the glass superstrate is  $n=1.51$  at 550nm. For modelling, the glass was assumed to be standard soda-lime glass.

#### 4.1.3.1 Multilayer Anti-Reflection Coating Deposition

Multilayer anti-reflection coatings can be deposited using a number of techniques, including electron beam evaporation with ion assist[38], ion beam sputtering[38], and magnetron sputtering[39]. These are relatively high energy techniques that deposit compact thin films with refractive indices close to bulk values.

The MAR coatings were deposited by reactive magnetron sputtering using a ‘PV Solar’ system from PowerVision Ltd. A 3-Dimensional layout of the system is shown in Figure 4.10. Prior to being loaded into the deposition chamber, soda lime glass substrates were cleaned in an ultrasonic bath in a 50%-50% solution of de-ionised water and isopropyl alcohol. After cleaning, the substrates were loaded into the deposition chamber via a load lock.

The system uses a vertical substrate carrier which rotates at ~120 rpm. The vacuum chamber is equipped with 3 vertically mounted 150 mm diameter circular magnetrons and a separate DC plasma source. The rotating carrier can accommodate up to six 5cm x 5cm glass substrates. Two of the magnetrons were fitted with Zirconium metal and Silicon planar targets. The deposition chamber is pumped using a turbomolecular pump (Edwards nEXT300D) mounted vertically, above the plasma source. The pre-process pressure is typically  $1 \times 10^{-5}$  mbar. Argon working gas is admitted in front of the magnetrons and the pressure (2.5mTorr) is controlled using mass flow controllers (MKS 1179A). Argon and oxygen gas flows into the plasma source were also controlled by mass flow controllers. During the SiO<sub>2</sub> deposition, the gas flow was set at 16 sccm (Ar) and 10 sccm (O<sub>2</sub>). For the deposition of ZrO<sub>2</sub>, the gas flow was set to 20 sccm (Ar) and 6 sccm (O<sub>2</sub>). The operation of each magnetron and all process parameters are under computer control.

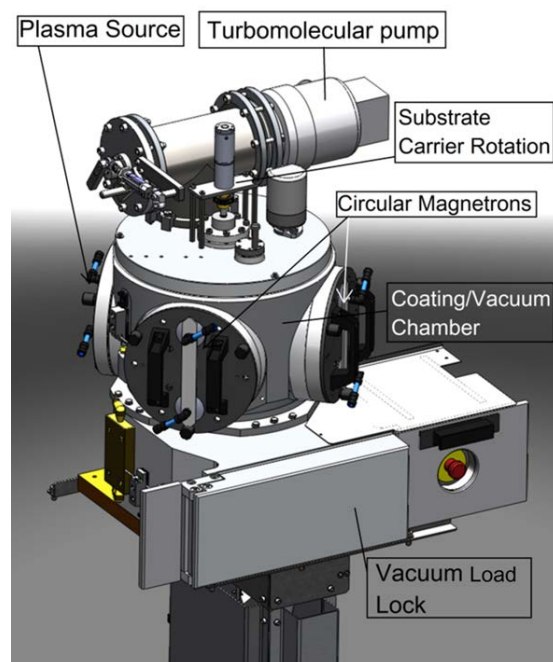


**Figure 4.10: A 3D schematic diagram of the reactive sputtering system used to deposit the MAR coatings.**

A 120 second argon/oxygen plasma pre-treatment was used for surface activation. This pre-treatment increases the substrate surface energy as determined by a water contact angle measurement. Surface activation improves adhesion. The argon flow to the plasma source was subsequently terminated to produce an oxygen plasma for oxidation of the Zirconium and Silicon layers. A thin layer of metal, typically ~1nm thickness, is deposited in each pass of the rotating carrier, which is fully oxidised as it passes through

the oxygen plasma to produce an optical quality oxide. High deposition rates can be achieved with this reactive sputtering strategy because the metal layer is deposited using a pulsed dc power supply (Advanced Energy Inc. Pinnacle Plus 5kW) and hysteresis effects are also avoided [56], [84], [85]. The frequency of the pulse was set to 150 kHz (6.6  $\mu$ s per pulse) for both materials. The zirconium was sputtered at 1kW using a 1.5 $\mu$ s (~ 25% reverse time), while the silicon was deposited at 1.5kW and 2.5 $\mu$ s (~50% reverse time). The deposition rate was 0.67nm/s for SiO<sub>2</sub> and 0.7nm/s for ZrO<sub>2</sub> films at each position on the rotating substrate carrier. The metal deposition zone and the plasma oxidation zone are separated by internal baffles to avoid poisoning of the metal targets. Layer thickness is controlled using time only since the metal sputtering rate is highly stable. Quartz crystal monitoring is not required. The computer control is set to switch between the magnetrons for pre-selected times corresponding to each layer thickness required. Further details of the deposition system and the deposition parameters are available elsewhere[39].

#### 4.1.3.2 Coating microstructure

Samples for Transmission Electron Microscopy (TEM) were prepared by Focused Ion Beam (FIB) milling using a dual beam FEI Nova 600 Nanolab. An electron beam evaporated platinum (e-Pt) over-layer was deposited followed by an ion assisted layer to define the surface and homogenize the final thinning of the samples down to ~100 nm. The TEM analysis was carried out using a Tecnai F20, operating at 200 kV to investigate the detailed microstructures of the MAR cross sections. Bright Field STEM images were obtained, revealing the layer thicknesses, uniformity and microstructure. Figure 4.11 shows a STEM image of a cross section of the MAR produced by FIB. The image shows that the coating is dense and uniformly covers the surface. No voids or pinholes are observed. Voids would degrade the optical performance by affecting the refractive index. Film density is also critical for achieving the coating durability required for the PV application. The presence of voids or pinholes provides access for water ingress and leads to degradation. The excellent coating uniformity observed is crucial for achieving and maintaining AR performance across large area PV modules. The SiO<sub>2</sub> appears amorphous while the structure in the ZrO<sub>2</sub> is columnar and typical for a sputtered thin film.

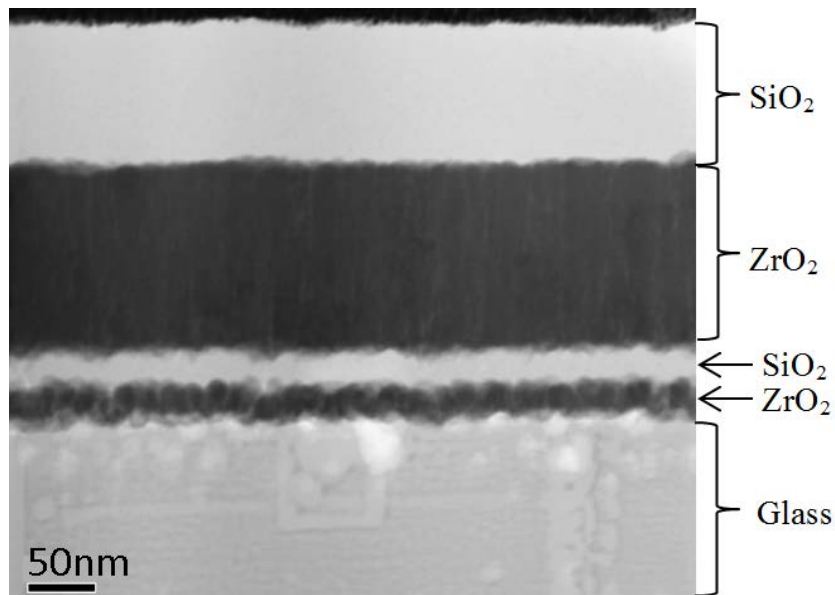


**Figure 4.11: STEM image of a cross –section of the MAR coating design presented in Figure 4.9, deposited using reactive sputtering. The SiO<sub>2</sub> is amorphous and the ZrO<sub>2</sub> has a columnar structure.**

#### 4.1.3.3 Increase in photocurrent and efficiency

MAR coatings were deposited on the glass superstrate of thin film CdTe devices to confirm that the cell performance improvement corresponds to the optical modelling. The thin film CdTe devices used in this study were fabricated at Colorado State University using their advanced research deposition system [86].

A 4 layer MAR corresponding to the design shown in Figure 4.9 was deposited sequentially using reactive magnetron sputtering. The reflection from the uncoated glass surface and the MAR coated surface was measured using a UV-vis spectrophotometer.

As shown in Figure 4.12 the application of the MAR reduces the WAR of soda lime glass by 2.9% in absolute terms, corresponding to a relative reduction in reflection of 69% [83]. In Figure 4.12 the modelled data does not include the reflection from the second air glass interface on the MAR samples, the accounts for the large discrepancy between measured and modelled reflectance data. Reducing reflectance and increasing transmission at the glass surface results in greater cell efficiency. Figure 4.13 shows the J-V characteristics of a thin film CdTe cell before and after application of the broadband anti-reflection coating. The maximum short circuit current density was increased by 0.65mA/cm<sup>2</sup> while the open-circuit voltage was unchanged. This increased the overall efficiency of the device from 10.6% to 10.9%, a useful relative increase of 3.6%.

Table 4.6 summarizes the design and performance of the MAR designed for CdTe and its effect on short circuit current.

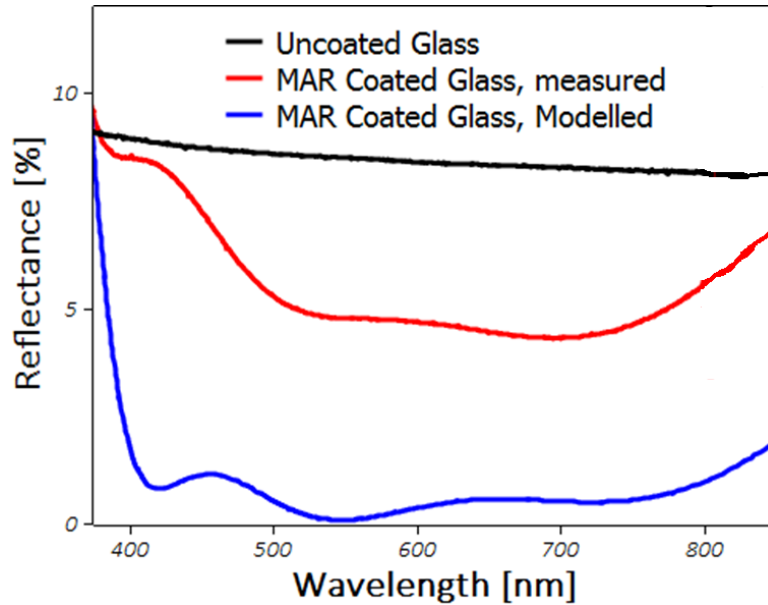


**Figure 4.12:** The modelled reflectance of MAR coated glass with no back reflectance, compared to the measured reflectance of bare glass and MAR coated glass.

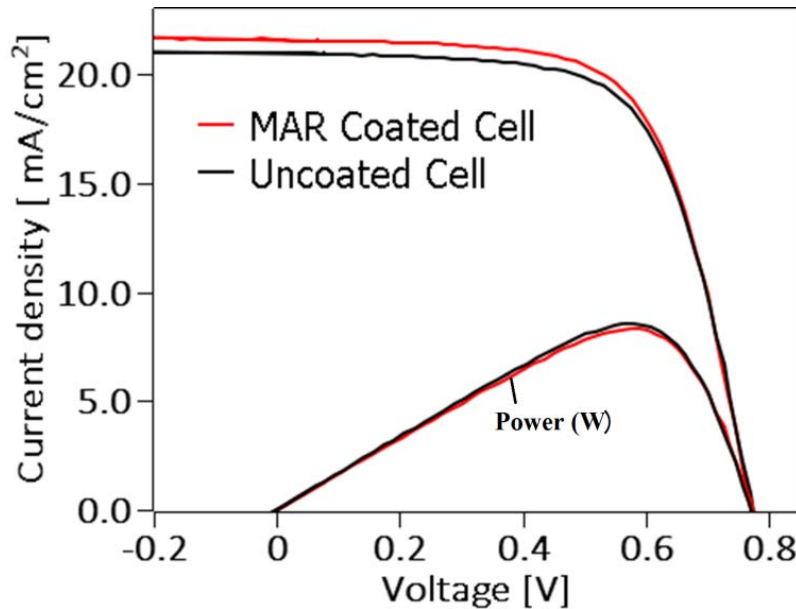


**Figure 4.13:** The J-V characteristics of a CdTe solar cell at full sun illumination, before and after the application of a MAR, also showing power decrease.

**Table 4.6: Measured performance of MAR for CdTe.**

	Layers	D [nm]	WAR [%]	Reflection reduction [%]	$J_{sc}$ [mA/cm <sup>2</sup> ]	Voc [mV]	Efficiency [%]
CdTe	4	277	1.30	69	29.88(+3.1%)	770	10.93(+3.6% relative increase)

#### 4.1.3.4 Performance with Angle of Incidence

The angle at which light enters a solar cell will vary depending on the position of the sun. As a result of the sun's changing position in the sky and diffuse conditions such as occurs in cloudy weather, the MAR must be functional over a broad range of angles of incidence. The MAR reduces reflection at all angles of incidence and is effective in both direct and in diffuse illumination. The effect of angle of incidence on WAR reflectance for the MAR design presented in Figure 4.9 is shown in Figure 4.14.

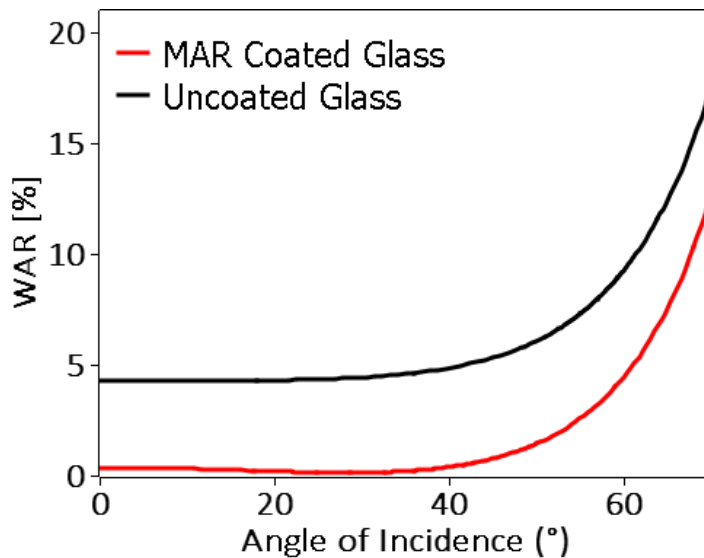


**Figure 4.14: The modelled WAR for the MAR design and compared with uncoated glass for a range of angles of incidence.**

#### 4.1.3.5 Effect of the optical properties of the CdTe stack

Designing an MAR coating for use across the CdTe wavelength range, without taking the whole stack into consideration, results in increased transmission. However, a slight benefit can be found when judging the MAR by how much light gets to the absorber rather than how little is reflected. To determine the best thicknesses of layers in the MAR it is necessary to model the entire CdTe device. In this work all deposited samples

designed for CdTe are based on the design shown in Figure 4.9, which considers only the air-glass interface. Considering the entire CdTe stack, to optimise transmission to the absorber, results in a slightly different design Table 4.7. The author wishes to stress that the coating design used for the CdTe wavelength range throughout the rest of the paper is that of Figure 4.9.

**Table 4.7: Modelled MAR coating design optimised for use on a specific CdTe solar cell.**

Layer Material	Thickness [nm]
SiO <sub>2</sub>	96
ZrO <sub>2</sub>	123
SiO <sub>2</sub>	26
ZrO <sub>2</sub>	17

Below is a comparison of transmission to the absorber (weighted average transmittance, WAT), WAR, and absorption (Weighted Average Absorption, WAA); between an MAR designed to reflect as little as possible from the glass surface and an MAR designed to transmit as much as possible to the absorber. Transmission only sees a 0.07% percent increase when taking the cell into consideration but an unexpected finding was that—when properly optimised for maximum transmission— the MAR’s reflection had increased at regions of the spectrum that are readily absorbed within the cell to allow for the transmission of less readily absorbed photon energy. Therefore a decrease in WAA is observed. A comparison of the different designs can be seen in Table 4.8.

**Table 4.8: MAR coating performance when optimised for different optical systems.**

Design focus	WAT [%]	WAR [%]	WAA [%]
Optimised AR for glass-air interface only	78.69	1.75	19.56
Optimised AR for use on CdTe stack	78.76	1.81	19.43

## 4.2 Single layer coatings

In this section, single layer coatings deposited at TWI (formerly The Welding Institute) in Cambridge and AR1 from Prinz Optic are compared over the wavelength range of CdTe solar cells.

### 4.2.1 Deposition methods

The TWI coatings were deposited using the dip coating method outlined in Chapter 3. The TWI coatings are a basic porous silica coating produced by drying a solution of silica nano-spheres, uniform in radius, into a coating. It was found that nano-spheres that result in a coating with ideal anti-reflective properties have a radius of 12nm. However, it is difficult to take images of nano-spheres this small, so an image taken with a scanning electron microscope (SEM) of silica particles with a larger radius (~200nm) is shown in Figure 4.15. A wetting agent is used to give the desired viscosity during deposition. The thickness of the coating can be controlled by changing the pull rate of the substrate, allowing for coatings designed for specific wavelengths. However, only a reflective minimum at a single point on the electro-magnetic spectrum can be manipulated by changing the thickness of a single layer design. Creating designs that accommodate for broader wavelength ranges is difficult without refractive index control and/or additional layers. The thickness of the coatings proved too difficult to control, but the most effective coatings were produced at a pull rate of 10mm per minute.

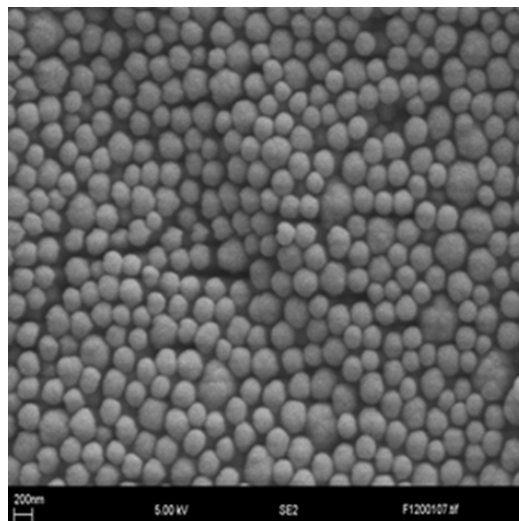


**Figure 4.15: SEM image of a porous silica coating with a sphere diameter of ~200nm. Sphere size varies, ideal AR properties were found using silica spheres of 12nm diameter.**

AR1, a commercial sol-gel hard coat, was sourced from Prinz Optic. AR 1 is designed to reduce reflection in the visible light wavelength range for solar and display glass application, however when considering the effectiveness of single layer coatings the performance depends on how close the refractive index is to the ideal and maintaining a quarter wavelength thickness. Across a larger spectrum these demands become more difficult to accommodate and optimisation involves selecting the wavelength to be the reflection minimum. Generally, no matter how broad the wavelength range being considered is, the minimum should be placed between 500nm-550nm, as this is the most energy dense region of the AM1.5 solar spectrum. Because of this, the same design can be used for most wavelength ranges and only lose slight gains in efficiency when compared to optimised ARCs.

The exact deposition technique for preparing the commercial AR 1 coatings is undisclosed. The coating is designed for use across the 380nm-780nm wavelength range. This is a similar wavelength range to that given by the band-gap of CdTe devices, which ends at ~850nm. The coatings use the hard coat method described in chapter 3 to reduce the refractive index of the coating. Although this is not an ideal coating it serves as a good chemical, commercial comparison with physically deposited MAR coatings for CdTe.

#### 4.2.2 TWI sol-gel coatings

The measured reflectance of TWI ARCs is shown in Figure 4.16. The measurement was taken using a spectrophotometer and demonstrates how the simple porous silica coating is effective in reducing reflection from the air glass interface. As the samples are dip coated, both sides of the glass are coated and so the reflection shown in Figure 4.16 is the cumulative reflection from both interfaces. It is worth noting that in the case of CdTe dip coating would not be an option as one side of the glass is already coating with a thin 2 layer anti-reflection coating and a transparent conducting oxide (TCO). However the effectiveness of this coating is indicative of similar coatings deposited through other sol-gel deposition methods that are capable of coating one side only. The TWI coating reduced the reflectance at the air-glass interface from ~8.4% to only ~3.6%. This is a total absolute reflection reduction of ~4.8%. The coatings were deposited on 1mm glass as with the MAR samples. In the case of TWI coatings, the reduction in reflection directly translates into gains in transmission, as shown in

Figure 4.17. The WAT of the glass rises from ~91.6% to ~96.4% across the 350nm-850nm wavelength range.

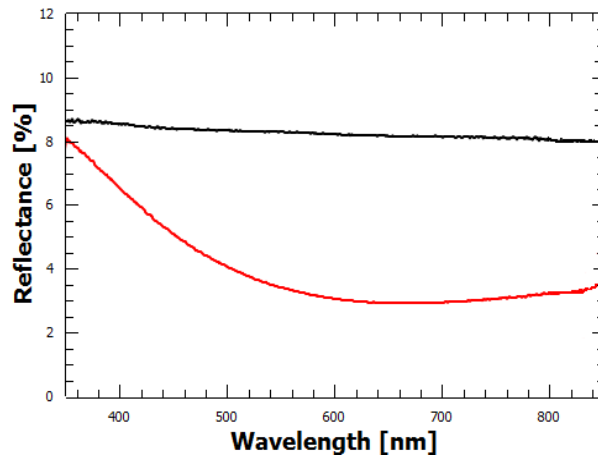


**Figure 4.16: Measured reflection of Sol-Gel Coated glass (Red) compared to uncoated glass (Black).**

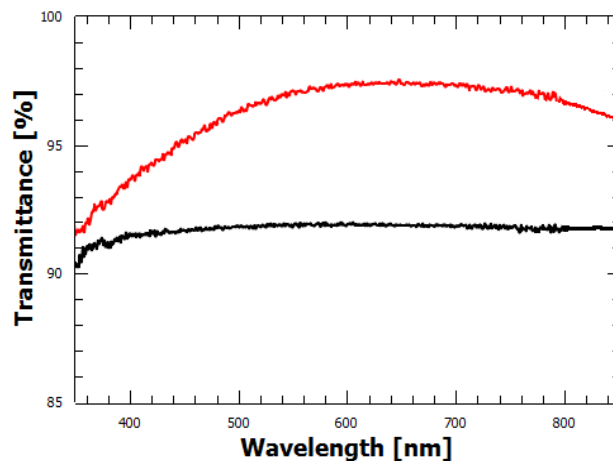


**Figure 4.17: Measured transmission of Sol-Gel coated glass (Red) compared to uncoated glass (Black).**

### 4.2.3 Commercial sol-gel hard coats

The spectrophotometer measured reflectance of the AR 1 hard coat is shown in Figure 4.18, compared to that of glass. Again, as with the TWI samples, the glass is coated on both sides and therefore the reflectance shown in Figure 4.18 is the cumulative reflection from both interfaces. AR 1 reduced reflectance from the basic ~8.4% to only ~2.2%. This is a reflection reduction of 6.2%, as this reduction is across 2 interfaces. However, transmittance measurement of AR1 samples shows possible issues with absorption or internal light scattering within the coating. Figure 4.19 shows the transmittance across the 350nm-850nm range. The WAT of the samples was 94.6%,

a gain of just 3.0% compared to the reduction in reflectance of 6.2%. This indicates a trade-off between the optical properties and the impressive damage resistance achieved with the hard coat technique. It is the author's opinion that absorption in the complex structure of hard coats reduces the transmission of coatings while achieving an impressively reflection. Both basic sol-gel coatings developed at TWI and MAR coatings developed at Loughborough University have this issue; the transmittance of MAR coatings for CdTe is ~97.4%. A consideration that may explain this absorption discrepancy is the substrate thickness: AR 1 was deposited on 3mm soda-lime glass, but exhibits far greater absorption – more than 3 times that of the other coatings.

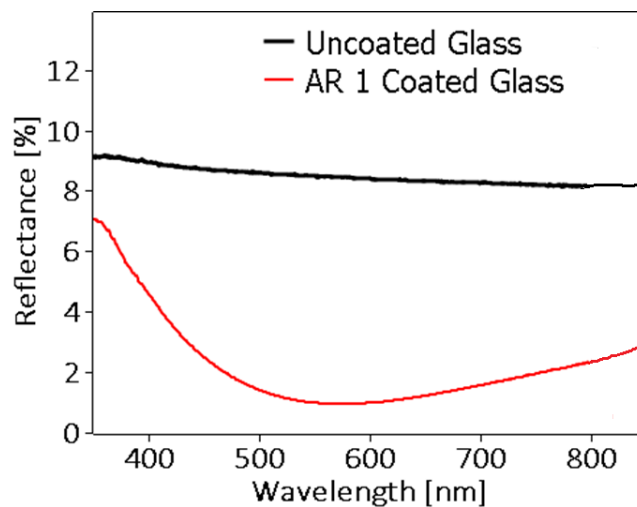


**Figure 4.18: Measured reflection AR 1 Coated glass (Red) compared to uncoated glass (Black).**

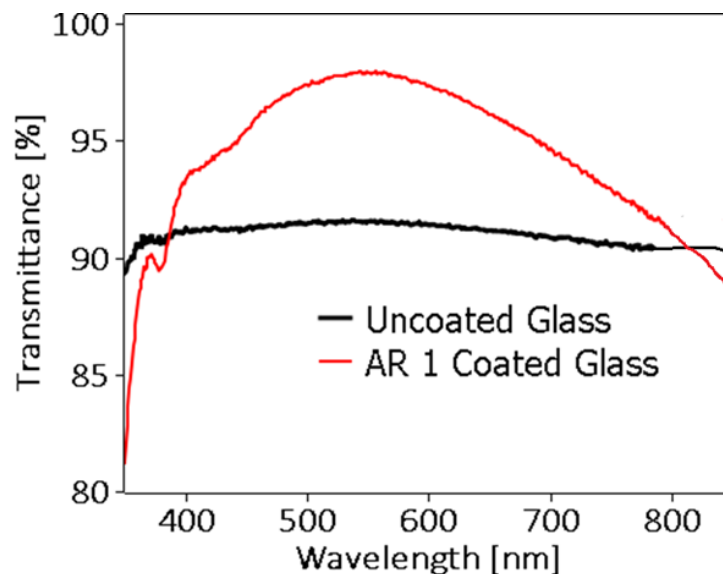


**Figure 4.19: Measured transmission of AR1 coated glass (Red) compared to uncoated glass (Black).**

### 4.3 Discussion

ARCs were produced through dip coating, reactive magnetron sputtering, and an unknown sol-gel method. All ARCs presented in this work are effective to different extents. MARs are the most effective coating; the reduction in reflection is directly translated to transmission due to the low absorption coefficients of silica and zirconia. Although the commercial sol-gel coating gives excellent reflection reduction, a direct improvement in transmission of the same magnitude has not been observed. This is likely due to absorption and scattering occurring in the coating because of the more complex structure of the coating. An optical comparison of the different coatings can be seen in Table 4.9. On a CdTe device only one air-glass interface need be considered, as such WAR values that represent transmission through a single interface are given in Table 4.9. This explains the discrepancy between the data shown Figure 4.18 and Figure 4.19, and the reflectance and transmittance given in Table 4.9

**Table 4.9: A comparison of the optical properties of the ARCs presented in this chapter.**

Design focus	Uncoated glass	MAR	Sol-gel TWI	AR1
Deposition method	None	Reactive magnetron sputtering	Dip coating	A sol-gel method (unknown)
Reflectance	8.4%	1.3%	1.8%	1.1%
Transmittance	91.6%	98.7%	98.2%	97.6%

Modelling was used effectively to predict optimal designs for MAR coatings, and deposited coatings gave reflection reduction as predicted.

# 5 APPLICATION OF ANTI-REFLECTION COATINGS TO OTHER PV TECHNOLOGIES

## 5.1 Introduction

In the previous chapter, the design and application of ARCs (including Multilayer Anti-Reflection (MAR) Coatings and sol-gel coatings) were evaluated for thin film CdTe photovoltaics (PV). The work showed that the STC efficiency of a thin film CdTe solar cell can be improved by 3.6% through the application of a MAR. However, thin film CdTe is only one kind of second generation PV device; other important types include CIGS, perovskite, and a-Si thin film PV. Perovskite is an emerging competitor in the solar PV landscape and has shown promising results in terms of high efficiency [87]. The cover glass on all PV devices suffers similar reflection losses. The reflection loss is dependent on the wavelength range utilised by the absorber layer. Coatings used for thin film CdTe are not optimal for the other technologies due to differences between their band gaps. The MAR coating design must accommodate these differences and adjust for a band gap of  $\sim 1.7\text{eV}$  (a-Si),  $\sim 1.5\text{eV}$  (perovskite),  $\sim 1.45\text{eV}$  (CdTe), and  $\sim 1.1\text{eV}$  (CIGS).). The coatings must be transparent across the entire wavelength range of the technology, with ideal refractive index.

As with the CdTe designs, MAR coatings utilise the interference of light at medium boundaries to reduce reflection and improve the light transmittance of glass. At any interface between media where there is a difference in the refractive index, a fraction of

the light is reflected and the rest is transmitted through the boundary. The amplitude of the transmitted and reflected waves can be calculated using the Fresnel equations. Multilayer thin film anti-reflective coatings utilise destructive interference of light waves reflecting at different medium boundaries to reduce the reflection. The interference is controlled using the phase difference of interfering waves, which is defined by the refractive index and the thickness of the layer.

## 5.2 Multilayer Anti-Reflection coatings

### 5.2.1 Multilayer anti-reflection experimental and Design

The structure of the MAR coatings was designed using optical modelling software similar to the CdTe design. The coatings were optimised to minimise the reflection based on destructive interference using the transfer matrix method [28]. The coatings were optimised for maximum performance in the wavelength ranges utilised by the thin films; CdTe, CIGS, a-Si, and perovskite solar cells.

The performance of the coatings was assessed by calculating their weighted average reflection (WAR).

Following the design, the thin film layers required for the MAR were deposited using a pulsed DC magnetron sputtering process, in a “PV Solar” deposition system from Power Vision Ltd., (Crewe, UK)[39]. The glass substrates were cleaned using the RCA cleaning procedure to ensure a good quality clean surface for the thin film deposition [88]. The refractive index, extinction coefficient, and thickness of the deposited films were measured using a Horiba Jobin Yvon UVISEL iHR320FGAS spectroscopic ellipsometer. The transmission and reflectance of the deposited films was measured using a spectrophotometer.

### 5.2.2 Multilayer Anti-Reflection coating for thin film a-Si PV

The band gap of the a-Si solar cell is  $\sim 1.7\text{eV}$  and is higher compared with CdTe. Therefore the wavelength range is narrowed to the range 350nm to 750nm. Table 5.1 shows the structure of a four layer anti-reflective coating designed for use on an a-Si solar cell. The total thickness of the MAR coating is only 248nm. The coating design shown in Table 5.1 reduces the WAR across the relevant wavelength range (350,700) to 0.61% in modelling from 4.25% for the uncoated glass. This is a relative 85% reduction in reflection. This WAR allows the a-Si solar cell to generate a maximum current

density of  $J_{sc}=24.47\text{mA}/\text{cm}^2$  which is 3.8% higher than using uncoated glass. Only  $0.14\text{mA}/\text{cm}^2$  is lost due to reflection at the front surface of the solar cell.

Table 5.1: The structure of the MAR designed for thin film a-Si solar cells.

Layer	Designed d [nm]
SiO <sub>2</sub>	87.03
ZrO <sub>2</sub>	117.59
SiO <sub>2</sub>	27.50
ZrO <sub>2</sub>	15.41

The modelled reflection spectra with and without an MAR coating are shown in Figure 5.1 the front reflection of the MAR coating (blue line), the front and back reflection (black line), and the front and back reflection of uncoated glass (red line).

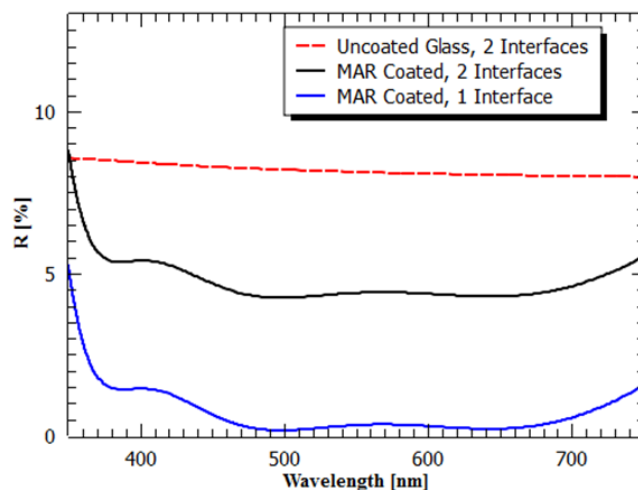


**Figure 5.1: Modelled performances of a four layer MAR coating for thin film a-Si PV.**

The film designed in Table 5.1 was deposited onto a 1mm thick soda lime glass slide, and the optical properties of the film were then measured using a spectrophotometer. The reflection spectrum of the deposited coating compared to the modelled data and uncoated glass is shown in Figure 5.2.

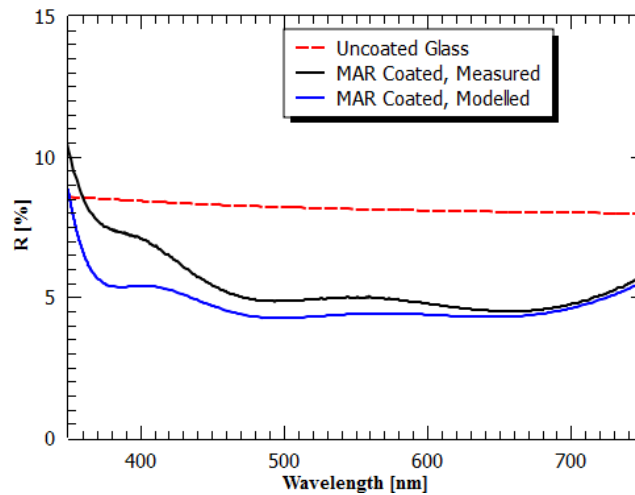


**Figure 5.2: The measured reflectance spectrum for 4layer MAR coating designed for a-Si solar cells (black line), the modelled reflectance (blue line), and that of uncoated glass (red line).**

The measured WAR for the MAR designed for use on a-Si solar cells was 5.32%. The WAR of uncoated glass over the same wavelength was measured at 8.58%. This result agrees well with the modelled data. The deposited MAR reduces the reflection by 3.36% compared to 3.8% modelled.

### 5.2.3 Multilayer Anti-Reflection coating for Perovskite PV

The band gap of Perovskite is  $\sim 1.5\text{eV}$ . The MAR was tailored to work in a wavelength range from 350nm to 800nm. Table 5.2 shows the structure of the four layer anti-reflective coating designed for use on perovskite solar cells. The total thickness of the MAR coating designed for perovskites is only 252nm. The coating design shown in Table 5.2 reduces the WAR over the perovskite usable wavelength range (350,800) to 0.8% in modelling from 4.24% for uncoated glass. This is a relative reduction in reflection of 81%. This WAR enables the perovskite solar cell to generate a maximum current density of  $J_{sc}=27.7\text{mA}/\text{cm}^2$ . This is 3.5% higher compared to uncoated glass and only  $0.24\text{mA}/\text{cm}^2$  is lost due to reflection at the front surface of the solar cell.

**Table 5.2: Structure of the MAR designed for use on perovskite solar cells.**

Layer	Designed d [nm]
SiO <sub>2</sub>	89.62
ZrO <sub>2</sub>	120.72
SiO <sub>2</sub>	25.07
ZrO <sub>2</sub>	16.64

The modelled reflection spectra of glass with and without a MAR coating are shown in Figure 5.3.

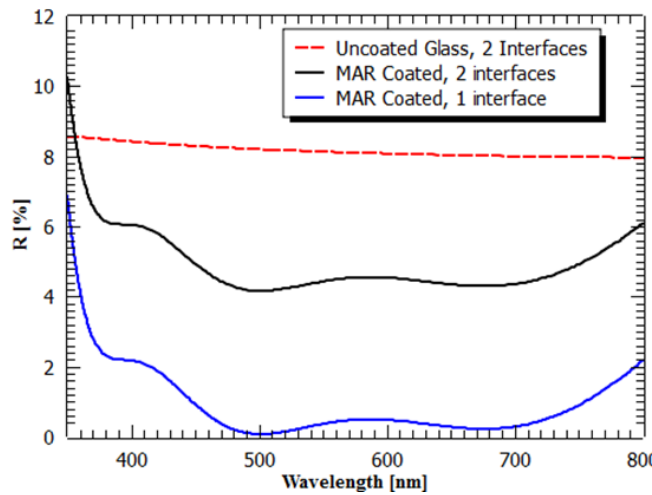


**Figure 5.3: Modelled performances of a four layered MAR coating for perovskite PV; the front reflection of the MAR coating (blue line), the front and back reflection (black line), and the front and back reflection of uncoated glass (red line).**

The designed MAR was deposited on to 1mm thick soda lime glass, and then the optical properties of the coating were measured. The reflection spectrum of the deposited coating compared to the modelled spectra, and to uncoated glass is shown in Figure 5.4.

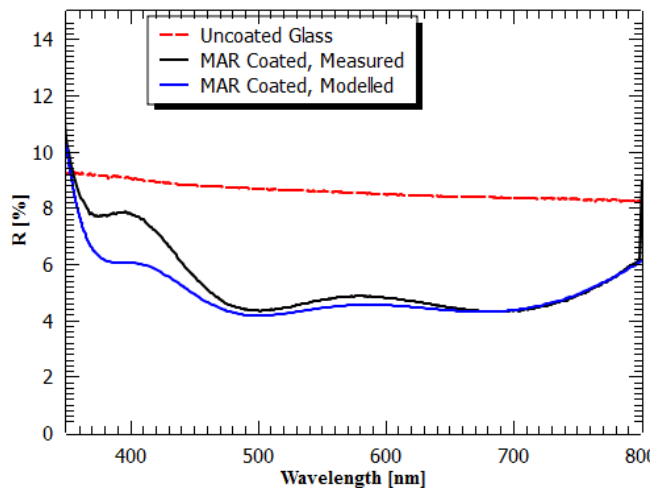


**Figure 5.4: The measured reflectance spectrum for six layer MAR coating designed for perovskite solar cells (black line), the modelled reflectance (blue line), and that of uncoated glass (red line).**

The measured WAR of the MAR designed for use on perovskite solar cells was 5.40%. Glass over the same wavelength range has a measured WAR of 8.54%. This result agrees with the modelled data. Without reflection from the back surface of the glass, the MAR reduces the reflection by 3.14% compared to the 3.5% modelled.

#### 5.2.4 Multilayer Anti-Reflection coating for CIGS

The CIGS material has a tuneable band gap. However, the high efficiency devices have a band gap of  $\sim 1.1\text{eV}$  [89]. This means the MAR used on a CIGS solar cell must reduce reflection from the surface of the cell between wavelengths of 350nm and 1100nm. This wavelength range is much broader than the range for CdTe, a-Si, or perovskite photovoltaics. Due to this extended bandwidth, an MAR for CIGS is more challenging. A four layer design was found to be ineffective. However, six layer designs are effective over this wavelength range, and therefore suitable for use with thin film CIGS. Table 5.4 lists the detailed structure of the 6 layer MAR coating designed for CIGS. The total thickness of this MAR coating is 335nm which is slightly thicker than the previous designs.

**Table 5.3: The structure of a six layer MAR designed for thin film CIGS solar cells.**

Layer	Designed d [nm]
SiO <sub>2</sub>	101.89
ZrO <sub>2</sub>	22.13
SiO <sub>2</sub>	17.75
ZrO <sub>2</sub>	143.95
SiO <sub>2</sub>	29.76
ZrO <sub>2</sub>	19.61

The six layer MAR design reduces the modelled WAR to only 1.49% from a WAR for the uncoated glass of 4.19% over the wavelength range used by CIGS solar cells (350, 1130). The modelled reflection spectra of MAR coated glass and uncoated glass are plotted in Figure 5.5. The reduced WAR predicts that the CIGS solar cell will generate a maximum current density of  $J_{sc}=44.25\text{mA}/\text{cm}^2$ , which is 2.8% higher than the use of uncoated glass.

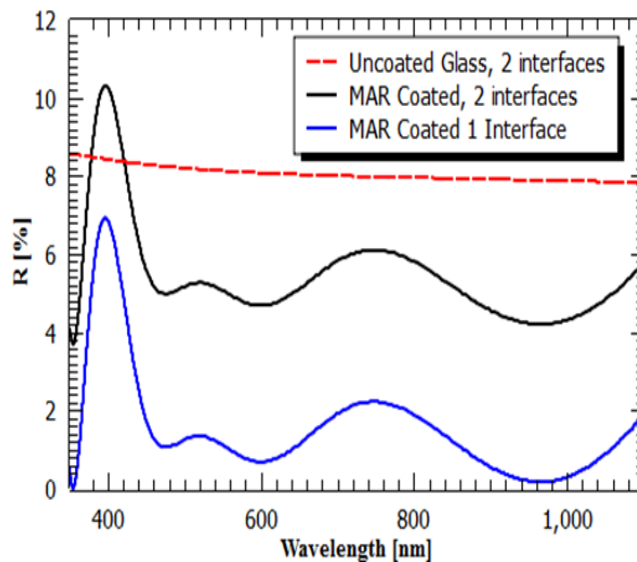


**Figure 5.5: Modelled performances of six layered MAR coating for thin film CIGS PV; the front reflection of the MAR coating (blue line), the front and back reflection (black line), and the front and back reflection of uncoated glass (red line).**

The designed coating was deposited on to a 1mm thick soda lime glass slide, and then the optical properties were measured using a spectrophotometer. A comparison of the reflection is shown in Figure 5.6.

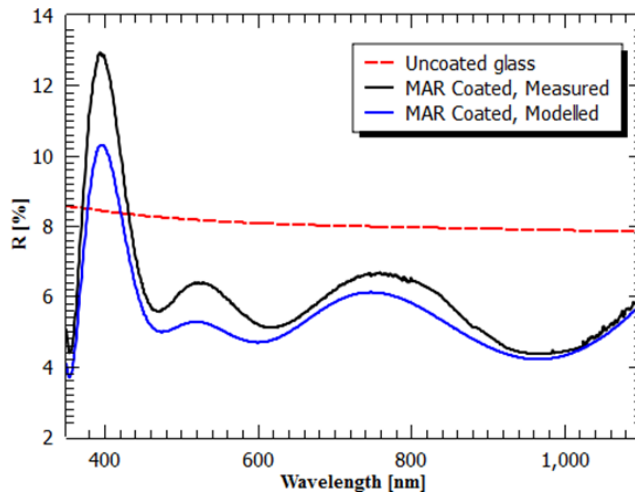


**Figure 5.6: The measured reflectance spectrum for a six layer MAR coating deposited for a CIGS solar cell (black line), compared to uncoated glass (red line), and the modelled reflectance (blue line).**

The measured WAR in the case of the six layer MAR designed for use on CIGS solar cells was 5.88%. The WAR for glass over the same wavelength range was measured to be 8.52%. This result agrees well with the modelled data. The MAR reduces light reflection by 2.64% compared to 2.8% for the modelled value.

### 5.2.5 MAR Comparison

MAR coatings have been designed for four types of thin film photovoltaics; CdTe, CIGS, a-Si, and perovskite. It has been shown for CdTe, perovskite, and a-Si devices that four layer designs are sufficient to suppress the reflection to 1.22%, 0.80%, and 0.61% respectively from optical modelling. The designs have been used to generate MAR coatings using a pulsed DC magnetron sputtering process, and their reflection has been measured using a spectrophotometer. The WAR for a-Si, Perovskite, and CdTe was 0.61%, 0.80 %, and 1.22% respectively, which corresponds to a reduction in light lost from the front surface of 85%, 81%, and 70%. However, in the case of CIGS, due to its extended wavelength bandwidth, a six layer coating was required to bring the WAR down to 1.49%. This is a 64% decrease in light loss from the front surface. The results are summarised in Table 5.4. All four types of coating are very thin and total thicknesses are less than 340nm.

**Table 5.4: The number of layers, the thickness, Weighted Average Reflection (WAR), relative reduction in reflection, and the increased maximum Jsc (improvement over uncoated glass in brackets).**

	Layers	Total d[nm]	WAR [%]	Reflection reduction [%]	Max Jsc [mA/cm <sup>2</sup> ]
a-Si	4	247	0.61	85	24.47 (+3.8%)
Perovskite	4	252	0.80	81	27.7 (+3.5%)
CdTe	4	277	1.22	70	29.88 (+3%)
CIGS	6	335	1.48	66	44.253 (+2.8%)

### 5.3 Sol-Gel anti-reflection coatings

The effectiveness of single layer coatings depends on the refractive index and thickness of the coating. When changing the wavelength range, the coating needs to be effective over changes to the most effective point on the spectrum in order to have a reflection minimum. However, as the solar spectrum is heavily weighted in the 350nm to 650nm wavelength range, the ideal coating changes minimally in terms of WAR. As a consequence, it is fair to use a coating designed for use in the visible light wavelength across broader wavelength ranges, as long as the coating does not heavily absorb light at these wavelength ranges. Both AR1 and TWI sol-gel coatings do not heavily absorb in the 350nm-1100nm wavelength range and can therefore be used in all solar applications. The candidate coating's performance was considered over different wavelength ranges by calculating the WAR across said ranges. The measured reflection from AR1 coated glass compared to uncoated glass is shown in Figure 5.7, and that of the TWI sol-gel ARC is shown in Figure 5.8.

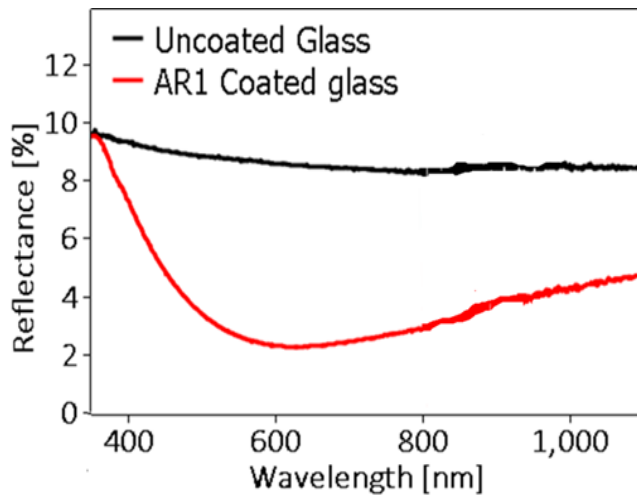


**Figure 5.7: A comparison of the measured reflectances at uncoated glass and AR1 coated glass surfaces, between 350nm and 1100nm.**

The reflectance of AR1 samples was measured using a spectrophotometer. The WAR from a 3mm soda-lime glass slide, coated on both sides with AR1, is reduced to 2.72% from 8.72% on bare glass, across the a-Si wavelength range (350nm, 750nm). Across the perovskite wavelength range (350nm, 800nm) WAR is reduced to 2.56% from 8.67%. Across the CIGS wavelength range (350nm, 1100nm) WAR is reduced to 2.71% from 8.62%.

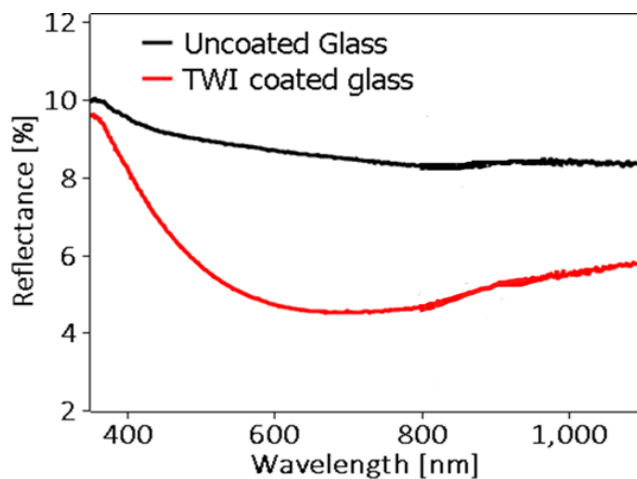


**Figure 5.8 A comparison of the measured reflectances at uncoated glass and TWI sol-gel coated glass surfaces, between 350nm and 1100nm.**

The reflectance of TWI sol-gel coatings on 1mm thick soda lime glass was measured over the same wavelength ranges. Across the a-Si wavelength range, the WAR was reduced to 5.67% from 8.91% without a coating. Across the perovskite wavelength range, the WAR was reduced to 5.40% from 8.78%. Across the CIGS wavelength range, WAR was reduced to 5.38% from 8.64%.

### 5.3.1 Comparison and discussion

The sol-gel coatings reduced the WAR across all wavelength ranges and therefore can be used on all PV technologies. The basic porous silicon AR was less effective than AR1; a side-by-side comparison is shown in Table 5.5. The results show that because the AM1.5 solar spectrum is so heavily weighted in the visible light region of the electro-magnetic spectrum, extending the wavelength range of interest has a negligible effect on the overall effectiveness of the coating. However when the sub 500nm wavelength range is a large percentage of the wavelength range, such as with a-Si, the WAR is greater, as with the very large wavelength range of CIGS. The commercial ARC was much more effective at reducing WAR than basic porous silica. However, both technologies had greater reflectances than glass coated by MARs designed for use over specific wavelength ranges.

**Table 5.5: Comparison of sol-gel coatings for various PV technologies.**

	TWI WAR [%]	AR1 WAR [%]	Percentage reduction TWI [%]	Percentage reduction AR1 [%]
a-Si	5.67	2.72	36	69
Perovskite	5.40	2.61	38	70
CIGS	5.38	2.71	38	69

# 6 DURABILITY OF ANTI-REFLECTION COATINGS

## 6.1 Introduction

Anti-reflection coatings are used in conjunction with photovoltaic technologies to reduce reflection from the air-glass interface. Commercial coatings for solar modules must be durable on a timescale comparable to the industry standard for solar panels, which are normally provided with a 25 year warranty. Any solar cell technology must undergo rigorous testing to ensure that the solar modules can endure decades of outdoor exposure. Any coating applied to solar modules must have an equivalent durability.

A variety of tests are available to assess the durability of ARCs. For example, micro-indentation scratch tests can be used to measure the scratch resistance of a coating[90], whereas the pull test and crosshatch test are useful to evaluate the adhesion of the coating. Additionally, in the case of pre-coated glass, resistance to the high temperatures involved in the solar stack deposition is necessary[91]. A coating resistant to all forms of mechanical and environmental damage can be considered durable. Resistance to weathering damage, related to use of the solar module in the field, can be determined using tests such as damp heat [92], cyclic humidity[92], and acid attack[93]. Acceptable durability is considered to be the ability of the coating to withstand exposure to subsequent module manufacturing processes, long term environmental exposure, and operational maintenance work.

Single layer anti-reflection coatings using magnesium fluoride ( $\text{MgF}_2$ ), or porous silica (with sufficiently low refractive index), have been used on solar cells and solar

modules. However, these coatings are only effective over a relatively narrow wavelength range. Additionally, because  $\text{MgF}_2$  is hydrophilic it has poor durability to weathering, so it is unsuitable for outside use.  $\text{MgF}_2$  has been used only to increase light transmission into champion devices[94]. Porous silica coatings, typically deposited by sol-gel deposition methods, integrate air pockets into the coating to lower the overall refractive index. This results in reduced scratch-resistance and coating hardness[63]. To address adhesion issues, commercially available porous sol-gel coatings use resins and coating microstructure to produce coatings with good adhesion. In comparison to bare glass, light transmission through the air-glass interface is improved. However, the improvements to adhesion and scratch-resistance of the coating may compromise the optical properties. When compared to basic porous silica, the more mechanically stable sol-gel coatings have reduced anti-reflective properties, as their complex porous/net-like structure increases light scattering and absorption due to increased density[63].

We report on the durability of broadband anti-reflection coatings, consisting of all dielectric multilayers of metal-oxides and sol-gel hard coat ARC, AR1 developed by Prinz Optic. We have investigated the performance, durability, heat resistance, microstructure, and adhesion of AR1 and silica/zirconia multilayer anti-reflection coatings, deposited using reactive magnetron sputtering. Some details of the stack design of the MAR, sputtering process parameters, and the optical and micro-structural properties of the layers are provided in chapter 4[39]. MARs avoid the mechanical issues that arise from reducing the packing density of a material because a layer with a very low refractive index is unnecessary. Metal-oxide dielectric coatings also have high hardness coefficients and very low extinction coefficients.

The MAR and AR1 coatings are examined separately for ease of reading, to allow the reader to focus on the performance of each coating separately. The coatings are compared in section 1.4, after the coating result sections.

## 6.2 Durability of the Multilayer Anti-Reflection Coatings

### 6.2.1 Adhesion

Adhesion is an important factor for coatings on thin-film PV modules. High adhesion results in a coating with greater durability since the coating is harder to remove from the glass. Adhesion of the MAR coatings was measured using the pull test and the cross hatch test. The samples were on 1mm thick soda lime glass.

## 6.2.1.1 Pull Test

Adhesion was measured using a Positest Adhesion tester in accordance with standards ISO 4624 and ASTM D4541[95], [96]. Aluminium dollies were fixed to the surface of the coating with an ethyl-2-cyanoacrylate based adhesive. The dollies were left to set and then loaded into the Positest adhesion tester and held firmly in place using a quick coupling mechanism. The Positest instrument was then used to apply a uniform and increasing force to remove the dolly from the surface of the coating. A stand-off is used to keep the substrate in place while the pull-off force is increased. A schematic diagram of the Positest is shown in Figure 6.1. The load is increased at a steady rate until the coating fails and delaminates from the substrate.

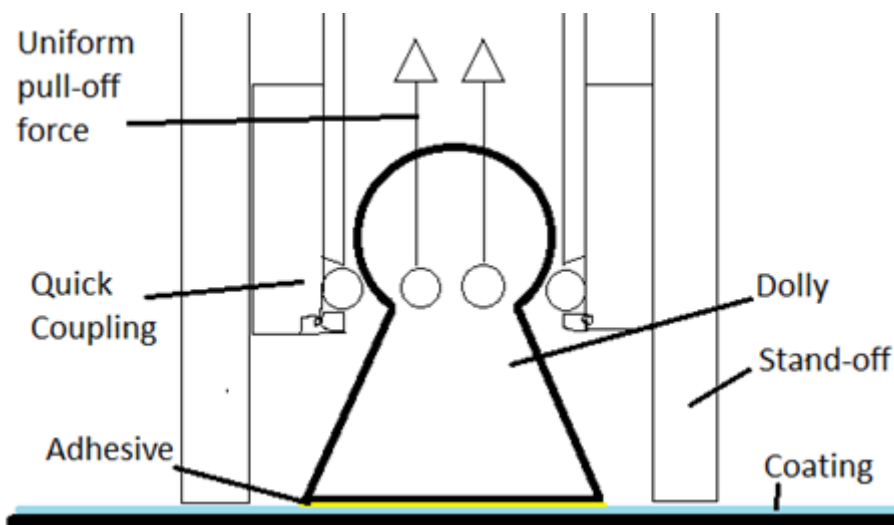


**Figure 6.1:** A schematic diagram of a dolly fixed to the coating surface using an adhesive, showing the dolly, stand-off, coupling, and uniform pull-off force lines.

Applying the pull test to the MAR surface failed to delaminate the coating from the surface of the glass. All experiments resulted in the glass substrate failing before the MAR delaminated, destroying the sample. Figure 6.2 shows the result of a test conducted with the highest recorded pull force of 0.98MPa. This demonstrates that the MAR coatings have excellent adhesion. However, applying the pull test to thicker – and therefore stronger – MAR coated glass could reveal the true failure point of the coating.

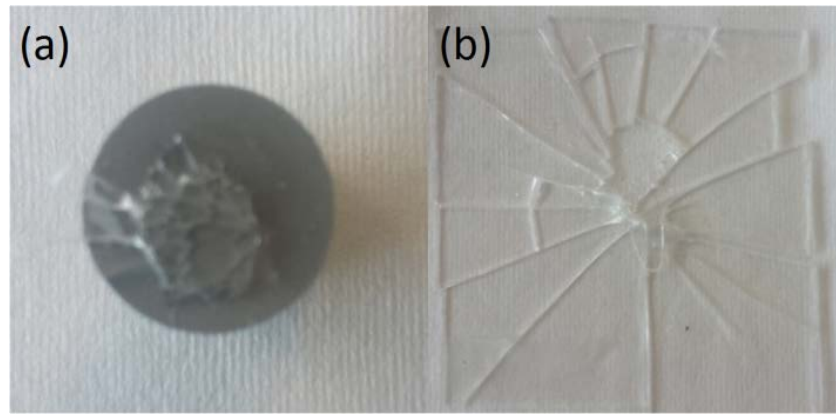


**Figure 6.2:** (a) The base of a dolly with glass adhered to the surface, indicating no coating delamination. (b) A fractured sample of the sputtered  $\text{SiO}_2/\text{ZrO}_2$  MAR coating on glass after a pull test. The coating remained undamaged.

#### 6.2.1.2 Cross-Hatch Test

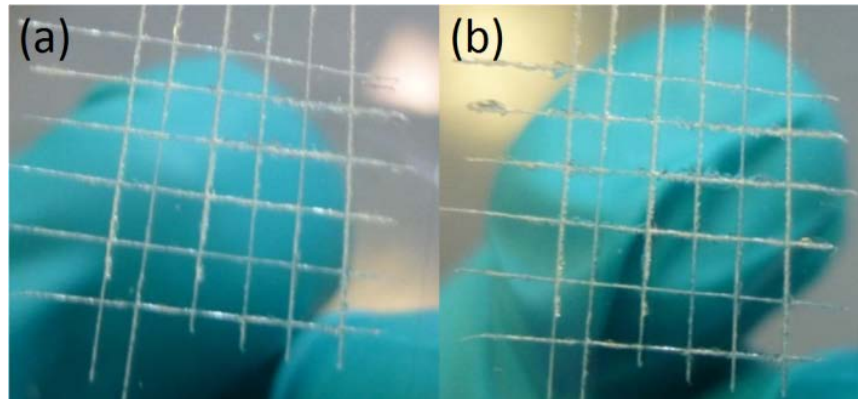


**Figure 6.3:** A cross-hatch test on the sputtered  $\text{SiO}_2/\text{ZrO}_2$  MAR coating before (a) and after the application of tape (b).

The standard test is to create a pattern consisting of 6 parallel lines by scratching the coating using a round, 6-bladed, steel cutting knife manufactured by Dyne Technology Inc. (model number: CC1000). Then, 6 parallel lines are scratched, intercepting the initial lines at  $90^\circ$  and creating a cross-hatch pattern. However, the coating was too hard to be scratched by the standard round, 6-bladed cutting knife, and a diamond scribe was used to scratch the samples instead. Semi-transparent pressure sensitive tape (manufactured by q-connect Ltd) was then applied to the cross-hatched area and removed at a  $90^\circ$  angle from the surface of the coating, as quickly as possible. The coating was then assessed in accordance with ISO 9211-4 [93]. The coating was given a rating between 0 and 5 based on observed delamination after the application and removal of tape. A score of 0 indicates excellent adhesion; a score of 5 indicates coating removal and extremely poor adhesion.

As shown in Figure 6.3 (b), the coatings showed minor damage after the application of tape: less than 5% of the total area was delaminated. However, some flaking can be observed at scratch intersections – this is caused by the diamond scribing and not by the tape. Therefore, the coating has an adhesion rating nearing 0. This confirms the MAR has excellent adhesion on glass. A full description of the classifications from the rating system is provided in the ISO 9211-4 specifications.

### 6.2.2 High temperature stability

Many processes in thin film CdTe solar cell manufacturing involve high temperatures, such as the CdTe deposition and the cadmium chloride ( $\text{CdCl}_2$ ) activation treatment. It is likely that module manufacturers would prefer to source glass with the MAR already applied. This would provide the benefit of improved module efficiency without the need to include another process step or incur its associated capital expenditure. Glass companies are familiar with magnetron sputtering processes and there should be no technical barrier for coating glass directly from a float line. However, this strategy is only feasible if the pre-coated MAR on glass can withstand the subsequent high PV manufacturing process temperatures. MAR glass samples were heated to increasingly high temperatures to test the heat resistance of the coatings.

Three types of substrate have been investigated: Soda lime glass, Eagle glass (EG), and TEC 7. The WAR on uncoated soda lime glass was 4.23%, for non-heated MAR the WAR was 1.6%; a reflection decrease of 2.63%. Figure 4.2 shows the modelled reflection of the deposited MAR coating used in this study. The measurements also confirmed excellent repeatability between the samples.

Variations in the WAR of as deposited samples are small and are caused by variations in the deposition conditions; the standard deviation of WAR of samples on Eagle glass, and TEC 7 is 0.077, and 0.073 percentage points respectively showing excellent reproducibility.

#### 6.2.2.1 Soda-Lime Glass

Figure 6.4 Shows SEM images of the surface of four MAR coated glass substrates; as deposited and then heat treated for 30min at 200°C, 400°C and 500°C. The images show that the surface of the as deposited samples was smooth and defect free. The surface was not damaged due to the exposure of the glass even up to 580°C. The reflection

measurements confirmed that the optical properties of the coatings remained unchanged.

The lowest temperature that caused signs of slight crazing to appear was 590°, in the form of isolated fissures in the surface of the MAR. An example of these fissures can be seen in Figure 6.6. Figure 6.7 shows an optical image of a coating exposed to a temperature of 600°C. Comparison with Figure 6.5 shows that at 600°C the coating has crazed completely.

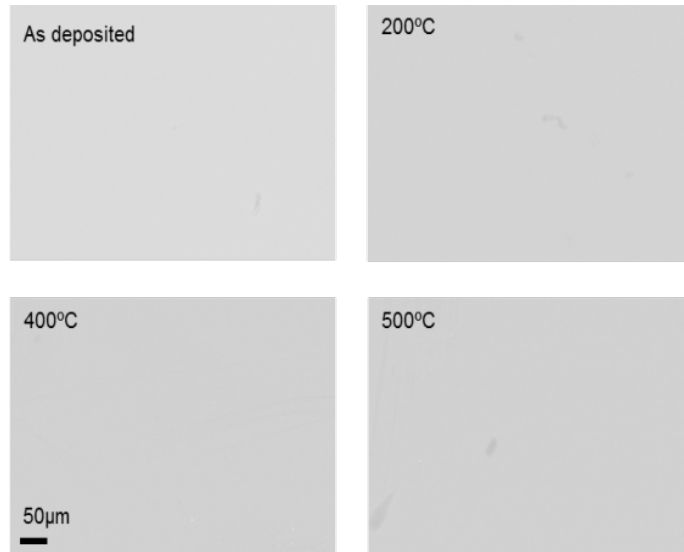


**Figure 6.4: SEM surface images of as deposited sputtered SiO<sub>2</sub>/ZrO<sub>2</sub> MAR coated glass surface and surfaces exposed to temperatures of 200°C, 400°C and 500°C for 30 min. No crazing is observed.**

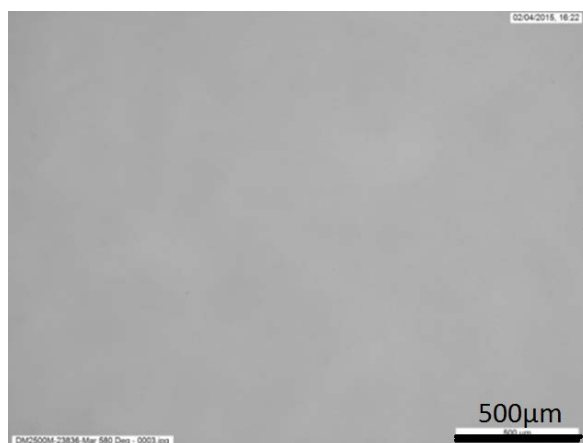


**Figure 6.5: An optical microscope image of a sputtered SiO<sub>2</sub>/ZrO<sub>2</sub> MAR sample exposed to 580 °C for 30 min, showing no visible damage.**



**Figure 6.6: Optical microscope images of a sputtered SiO<sub>2</sub>/ZrO<sub>2</sub> MAR sample exposed to 590°C for 30 min, showing an isolated fissure in the surface of the coating.**

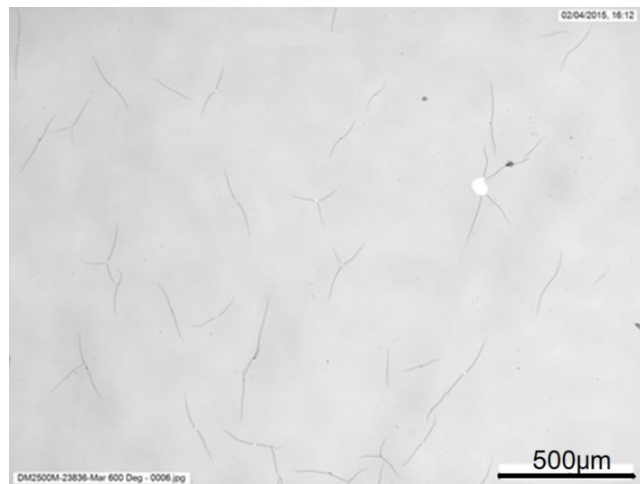


**Figure 6.7: Optical microscope image of a sputtered SiO<sub>2</sub>/ZrO<sub>2</sub> MAR sample exposed to 600°C for 30 min revealing the occurrence of mild crazing.**

A comparison of the reflectance of MAR coated glass after heat treatment at 500°C, 590°C and 600°C can be seen in Figure 6.8. The reflectance in terms of WAR for uncoated soda lime glass was 4.23%, for as deposited MAR the WAR was 1.61%, exposed to 500°C the WAR was 1.59%, exposed to 590°C the WAR was 1.41%, and exposure to 600°C the WAR was 1.36%. This suggests that heat treatment has a negligible effect on the WAR of the samples.

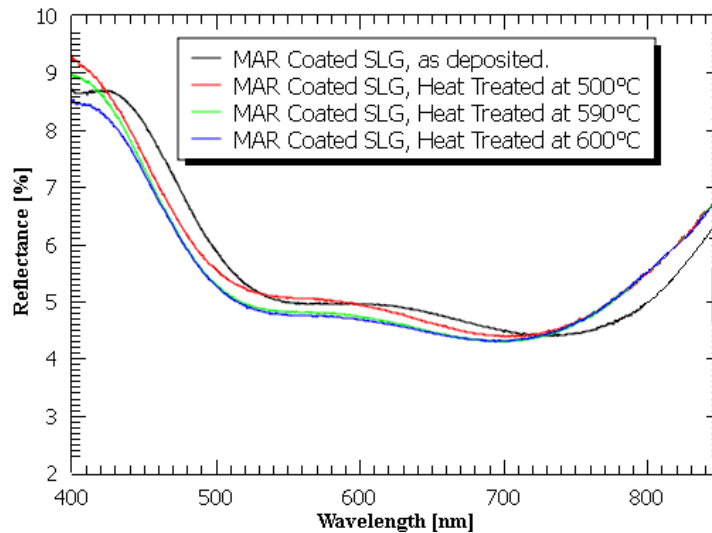
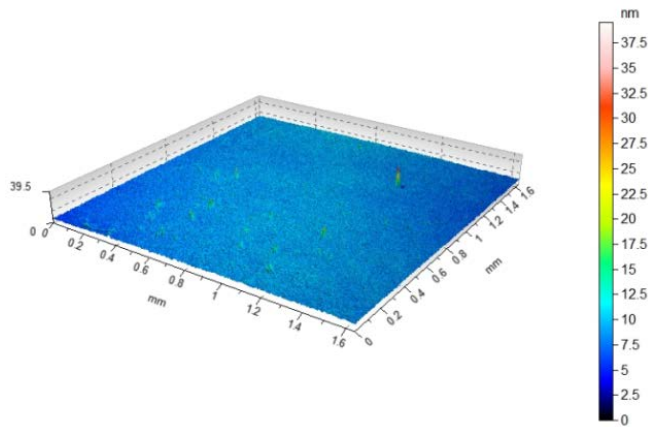


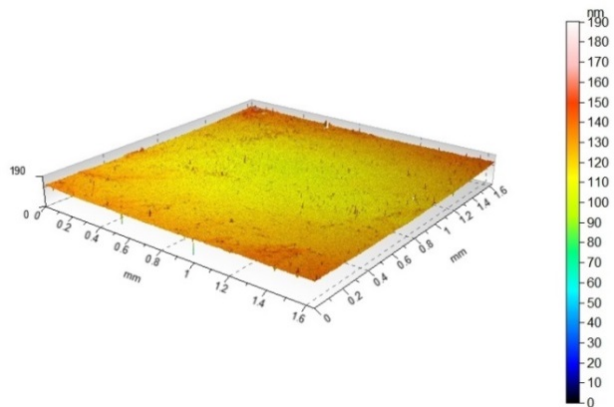
**Figure 6.8: Measured reflectance spectrum of as deposited sputtered  $\text{SiO}_2/\text{ZrO}_2$  MAR coated soda lime glass (SLG)(black line) and sputtered  $\text{SiO}_2/\text{ZrO}_2$  MAR coated glass heat treated to 500°C (red line), 590°C (green line) and 600°C (blue line) for 30min, including back surface reflectance.**

Fissures are produced in the surface of the MAR samples only after the soda lime glass has begun to warp due to the heat. Figure 6.9 provides a series of CCI images showing that the shape of the substrate changes depending on temperature. The corners curl up significantly, at this point the coating crazes and RMS roughness begins to increase. Experiments on Eagle glass were carried out to investigate the effect of using a high temperature glass substrate with a lower coefficient of thermal expansion on the surface roughness of the coating after heat treatment.

A. CCI Image of as deposited sample.



B. CCI Image of MAR sample on SLG exposed to 500°C.



C. CCI Image of MAR sample on SLG exposed to 600°C

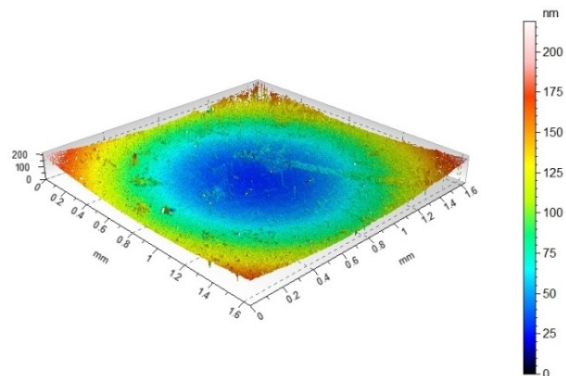


**Figure 6.9: CCI images of MAR samples. A: As deposited. B: Heat treated at 500°C. C: Heat treated at 600°C.**

#### 6.2.2.2 Pilkington TEC 7 Glass

Figure 6.10 shows a comparison of the surfaces of MAR coatings deposited onto Pilkington TEC 7 glass after heat treatment at 500°C, 580°C, 590°C, and 600°C. Again the images show that the surface of the as deposited samples was smooth and defect free

and the samples show no sign of crazing under SEM imaging. As the soda lime glass used in TEC7 is 3mm thick the glass warped less at temperatures approaching 600°C than the 1mm thick soda lime glass samples. Slight crazing could only be found at the edges of the sample at temperatures above 590°C. This supports the view that crazing in the coating is primarily caused by the mechanical movement of the substrate as it approached its melting point. An optical image of crazing at 590°C is shown in Figure 6.11.

The Transparent Conducting Oxide (TCO) on the opposing side of the glass to the MAR was unaffected by the heat treatment as inspection at all temperatures showed no signs of crazing.

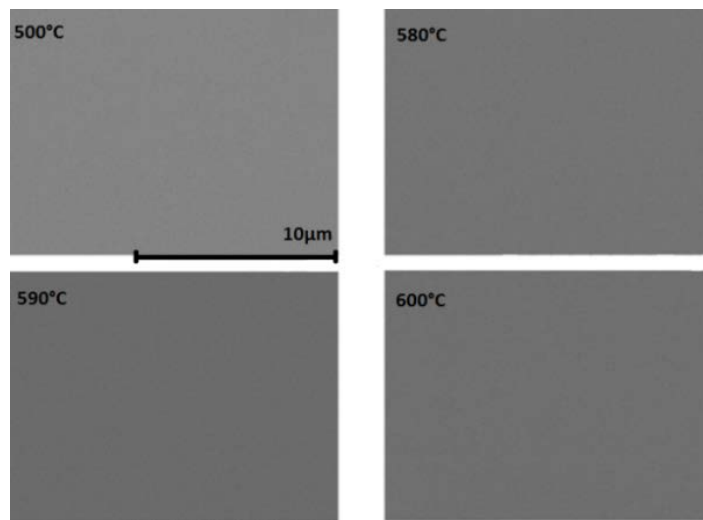


**Figure 6.10: SEM surface images of the central area of sputtered  $\text{SiO}_2/\text{ZrO}_2$  MAR coatings deposited on TEC 7 and then exposed to temperatures of 500°C (top left), 580°C (top right), 590°C (bottom left) and 600°C (bottom right). The coatings show no signs of crazing.**

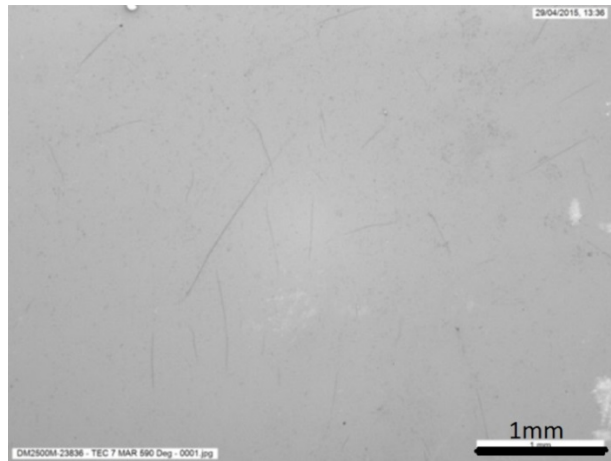


**Figure 6.11: Optical microscope image of a sputtered  $\text{SiO}_2/\text{ZrO}_2$  MAR coating deposited on TEC 7 and exposed to  $590^\circ\text{C}$  for 30 minutes showing very mild crazing at the warped edges of the glass.**

A comparison of the reflectance of MAR coated TEC 7 glass after heat treatment at  $500^\circ\text{C}$ ,  $590^\circ\text{C}$  and  $600^\circ\text{C}$  is shown in Figure 6.12. The reflectance in terms of WAR for non-heat treated MAR on TEC 7 was measured at 1.45%. Samples before and after heat treatment showed negligible difference in WAR.

**Table 6.1: Comparison of WAR of samples on TEC 7 before and after heat treatment at different temperatures. Numbers exclude back surface reflection.**

Heat treatment temperature [ $^\circ\text{C}$ ]	WAR As Deposited [%]	WAR Post Treatment[%]
500	1.46	1.72
580	1.45	1.46
590	1.47	1.60
600	1.38	1.73

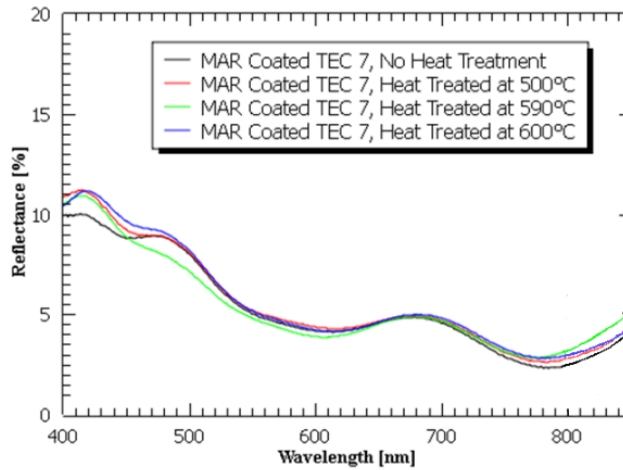
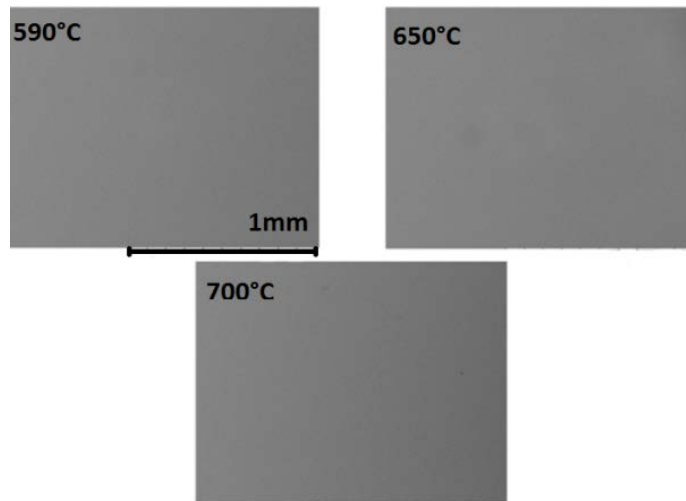


**Figure 6.12: Measured reflectance spectrum of as deposited sputtered  $\text{SiO}_2/\text{ZrO}_2$  MAR on TEC 7 glass (black line), and MAR coated glass heat treated to  $500^\circ\text{C}$  (red line),  $590^\circ\text{C}$  (green line) and  $600^\circ\text{C}$  (blue line), including back surface reflectance.**

#### 6.2.2.3 Corning Eagle Glass

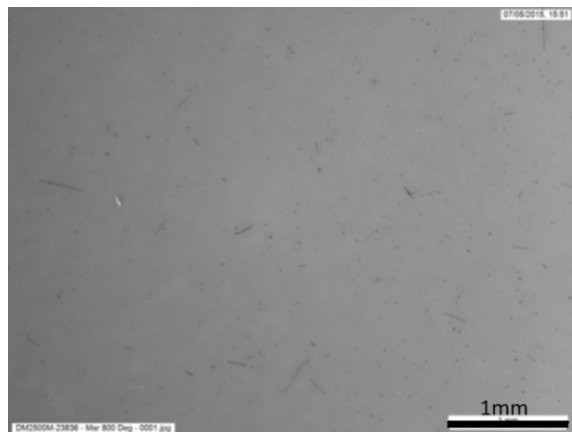
To distinguish whether the MAR coating on soda lime glass crazes due to the heat treatment or the deformation of the substrate, we repeated the tests using Corning Eagle Glass™. The annealing point of a glass is the temperature at which the glass is still hard to deform but has been softened enough to allow for stresses to relax within the glass. Eagle glass has an annealing point of  $722^\circ\text{C}$ , allowing for greater temperature heat treatment compared to soda lime glass which has an annealing point of  $546^\circ\text{C}$ .

Figure 6.13 shows a comparison of the surfaces of MAR coatings deposited onto Eagle glass after heat treatment at  $590^\circ\text{C}$ ,  $600^\circ\text{C}$ , and  $700^\circ\text{C}$ . The images show that the surface of the as deposited samples was smooth and defect free and the samples show no sign of crazing. Reflection measurements from the spectrophotometer show that heat treatment has a negligible effect on the WAR of the coated samples.



**Figure 6.13: SEM surface images of sputtered SiO<sub>2</sub>/ZrO<sub>2</sub> MAR samples deposited on Eagle Glass exposed to temperatures of 590°C, 650°C and 700°C. The samples show no signs of crazing.**

Figure 6.14 shows an optical image of a coating exposed to a temperature of 800°C. Comparison with Figure 6.13 shows that at 800°C the coating has begun to craze. However, only small examples of fissures in the coatings surface are observed at this stage. This difference in the damage compared with soda lime glass is due to the comparatively higher annealing point, higher melting point, and lower coefficient of thermal expansion of Eagle glass.



**Figure 6.14: Optical microscope images of a sputtered SiO<sub>2</sub>/ZrO<sub>2</sub> MAR sample deposited on Eagle glass exposed to 800°C for 30 minutes with no crazing occurring, revealing mild crazing.**

A comparison of the reflectance of MAR coated Eagle glass as deposited and after heat treatment at 590°C, 700°C, and 800°C can be seen below in Figure 6.15 and

Figure 6.16. The reflectance in terms of WAR for untreated MAR on Eagle glass was measured at 1.76%. The WAR after heat treatment is provided in Table 6.2.

**Table 6.2: Comparison of WAR of samples on EG before and after heat treatment at different temperatures.**

Heat treatment temperature [°C]	WAR As Deposited [%]	WAR Post Treatment[%]
590	1.76	1.70
650	1.71	1.62
700	1.89	1.77
800	1.76	1.50

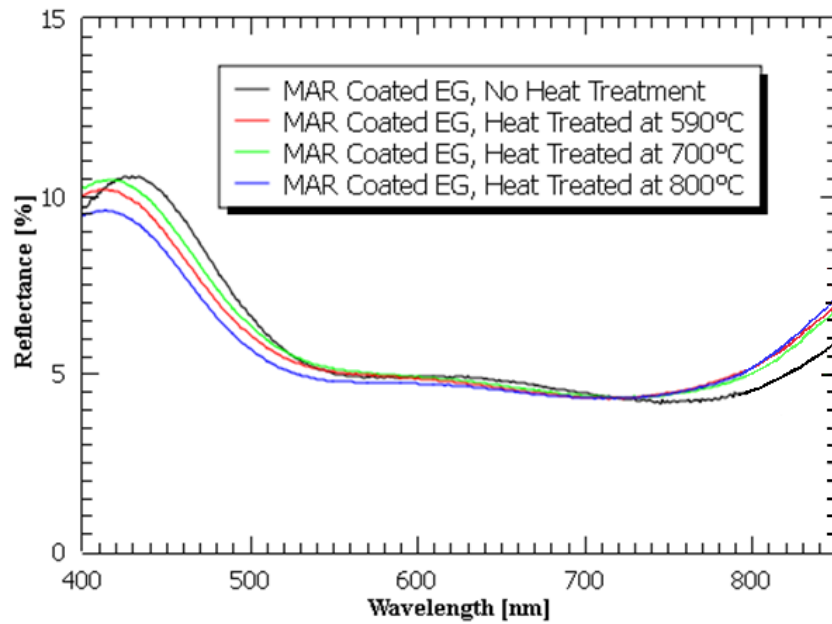


**Figure 6.15: Measured reflectance spectrum of uncoated glass (black line) MAR coated glass (red line), and MAR coated glass heat treated to 700°C (green line) and 800°C (blue line), including back surface reflectance.**

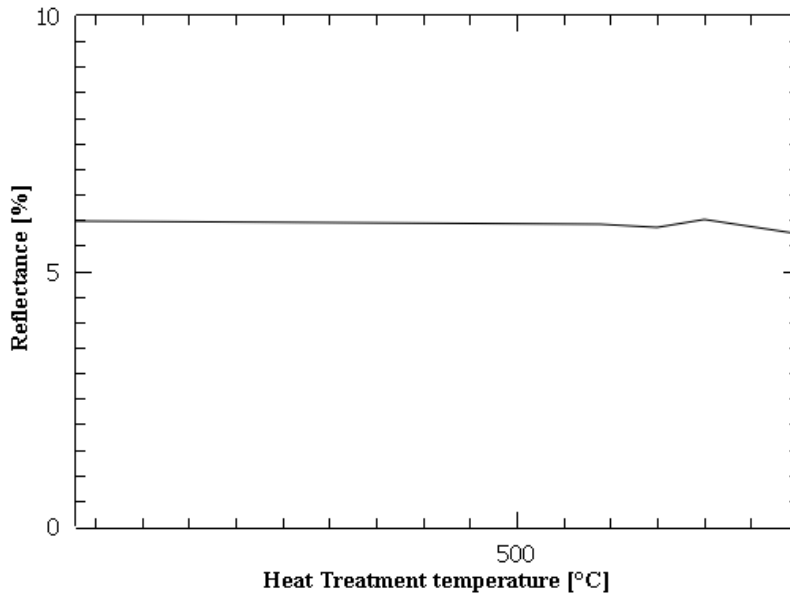


**Figure 6.16: Plot of heat treatment temperature against WAR for sputtered SiO<sub>2</sub>/ZrO<sub>2</sub> MAR coated Eagle glass.**

### 6.2.3 Resistance to temperature and humidity

Solar modules are used in many climates, some of which are particularly hot and humid such as occur in Equatorial regions. MAR coatings used on all solar cell technologies must be able to withstand high humidity, high temperatures, and temperature cycling.

A damp heat (DH) test was performed, in accordance with the IEC 61646 standard. The three samples were stressed in a Sanyo Gallenkamp HCC065 environmental chamber at 85°C and 85% relative humidity (RH) for a total of 1000 hours. Prior to the test, the samples were visually inspected and reflectance measurements were taken. The samples were then taken from the chamber for testing at 20, 85, 160, 250, 325, 420, 500, and 1000 hours. Figure 6.17 shows the measured WAR of the samples after each was exposed to damp heat up to 1000 hours.

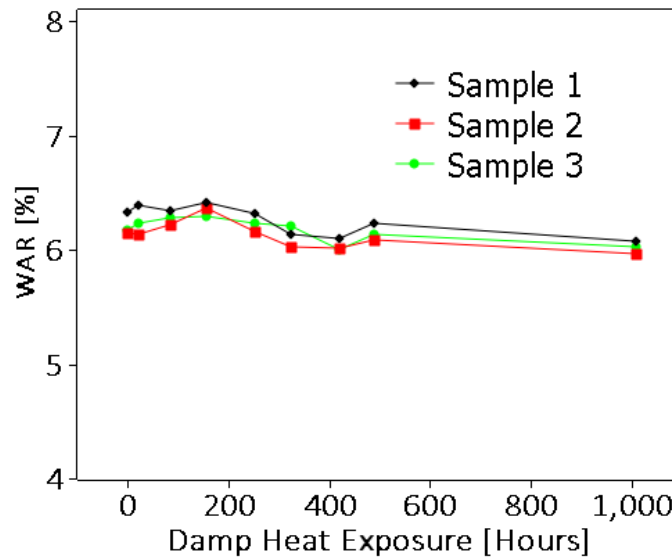


**Figure 6.17: Measured weighted average reflectance (WAR) of sputtered  $\text{SiO}_2/\text{ZrO}_2$  MAR samples after exposure to 85% humidity at a temperature of 85°C, for up to 1000 hours.**

The WAR remained relatively constant after 1000 hours of 85°C/85% Damp Heat testing carried out in accordance with the IEC 61646 test for Photovoltaics devices. These accelerated tests show that humidity has little effect on the coating stability and is unlikely to cause delamination or other damage in the field.

#### 6.2.4 Contact angle

Another quality used to measure the ability of a coating to resist water damage over long periods of time is the water contact angle. Contact angle is the angle at which a water droplet connects with the surface it is resting on. A high contact angle indicates high water repellence (hydrophobicity). A high contact angle indicates a lower run-off angle for water resting on a surface. This means that when a surface has high hydrophobicity, detritus and excess water is removed from the surface through gravity at a greater rate; maintaining a cleaner, drier surface. As ARCs are the outermost layer of the solar cell, it is therefore beneficial for ARCs to have a high contact angle. A water drop on the surface of a coating is shown in Figure 6.18, the contact angle is 35°. The application of a thin hydrophobic coating, (hexamethyldisilazane abbreviated to HMDS) to the surface of the MAR changes the contact angle from 72° to 107°, as shown in Figure 6.19.

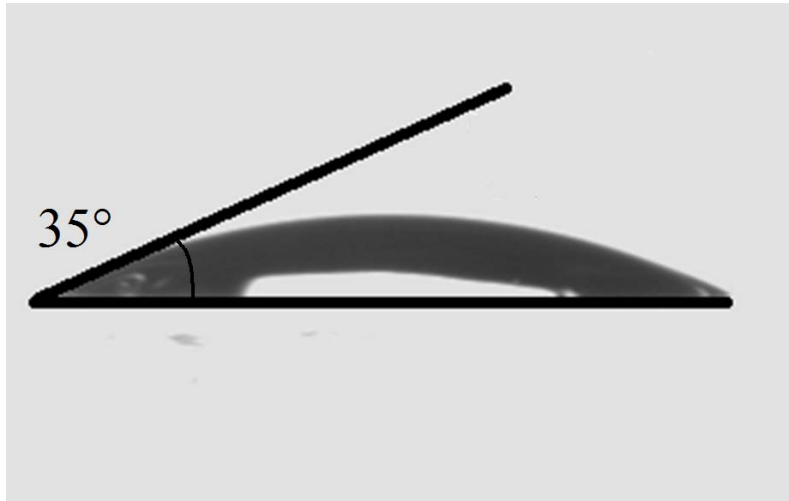


**Figure 6.18:** A water drop on the surface of a sputtered  $\text{SiO}_2/\text{ZrO}_2$  MAR coating with a contact angle of  $35^\circ$ .

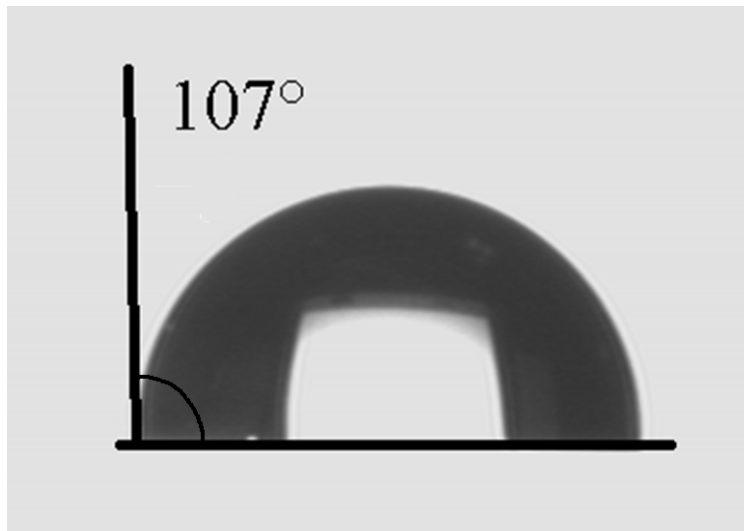


**Figure 6.19:** A water drop on the surface of a sputtered  $\text{SiO}_2/\text{ZrO}_2$  MAR coating, coated in HMDS. The contact angle is  $107^\circ$ .

### 6.2.5 Stability against thermal cycling

Solar modules in the field will experience changing temperatures over 24 hours due to the day/night cycle and the seasonal weather patterns. Accelerated lifetime testing of the MAR was performed by cycling the MAR coatings at  $-40^\circ\text{C}$  to  $85^\circ\text{C}$  in a Vötschtechnik VCS 7430-4 H climatic chamber, with a minimum dwell time of 10 minutes at each temperature extreme. The WAR of the samples was then measured after 0, 100, 150, and 200 cycles. Figure 6.20 shows the WAR measured for three samples, which were cycled 200 times in accordance with the IEC 61646 protocol.

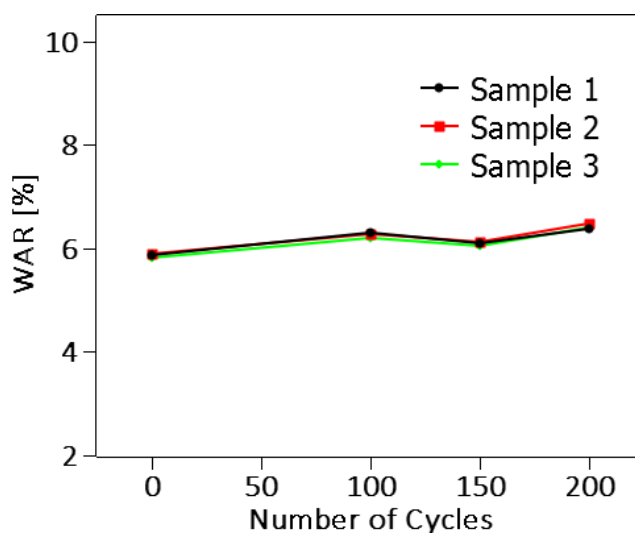


**Figure 6.20: The measured weighted average reflectance (WAR) of sputtered  $\text{SiO}_2/\text{ZrO}_2$  MARs cycled 0, 100, 150, and 200 times between  $-40^\circ\text{C}$  and  $85^\circ\text{C}$  in a climatic chamber. This is a minimum of 2000mins (~33hrs) at each temperature extreme.**

No coating degradation was observed as a result of the thermal cycling test, according to the IEC 61646 test for Photovoltaic devices. This qualifies the coating for use on photovoltaic modules and provides confidence that the coating will not be damaged by the day /night cycle.

### 6.2.6 Water solubility testing

MAR coatings must be resistant to prolonged exposure to water. MAR coated glass surfaces were exposed to different tests to measure the coating resistance to water, according to the ISO 9211-4:2012 protocol[93]. The standard test uses conditions of increasing severity. The least aggressive test involves immersion of the glass samples for 6 hours in de-ionised (DI) water. DI water is defined as water with a resistivity greater than  $0.2 \text{ M}\Omega\text{-cm}$ . This test is then extended to 24h and 96h. Tests increase in severity to involve immersing the samples in boiling DI water for 5, 15, and 30 minutes. The most severe test involves submerging the sample in boiling DI water for 2 minutes, and moving it immediately into a bath of DI water at room temperature for 1 minute. The tests were carried out using semiconductor grade DI water ( $18 \text{ M}\Omega\text{-cm}$  resistivity). A sample was exposed to boiling DI water for 5, 15 and 30 minutes. The sample showed no sign of physical degradation. Figure 6.21 shows recorded WAR values obtained using a spectrophotometer.

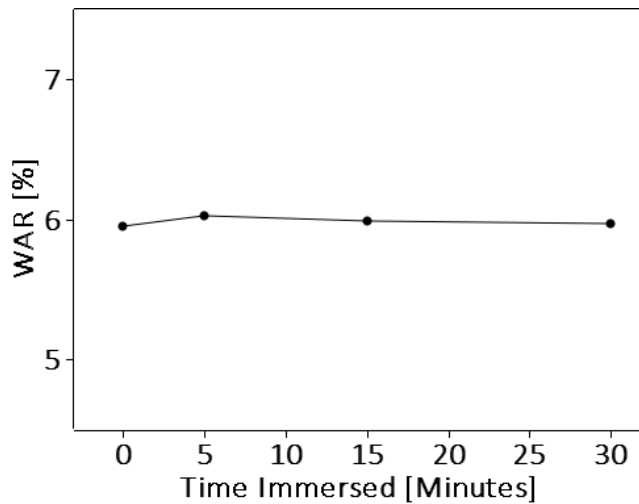


**Figure 6.21: The weighted average reflectance (WAR) of sputtered  $\text{SiO}_2/\text{ZrO}_2$  MAR samples after immersion in boiling DI water for 0, 5, 15, and 30mins.**

The samples were then placed in boiling water for 2 minutes and then placed in room temperature DI water for one minute. According to ISO 9211-4:2012, this process constitutes a single test cycle. Ten cycles were applied to the sample, followed by visual inspection and spectrophotometer measurements. No changes were observed visually after each cycle. The WAR measurements are shown in Figure 6.22. The samples passed the ISO 9211-4:2012 test with no sign of degradation. This result predicts that MAR coatings can withstand wet climates and extreme weather.

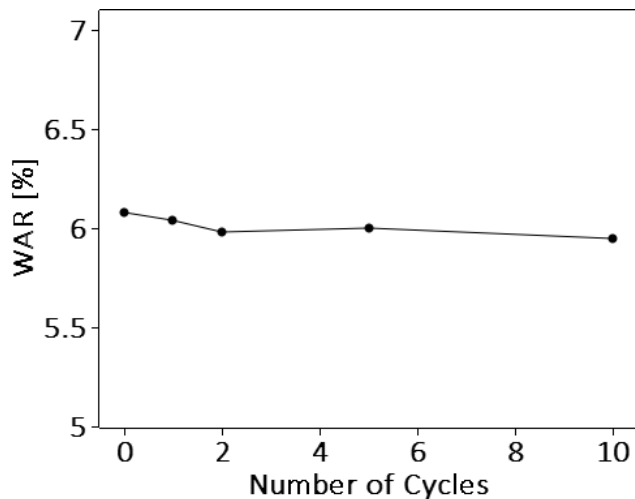


**Figure 6.22: The weighted average reflectance (WAR) of sputtered  $\text{SiO}_2/\text{ZrO}_2$  MAR coated glass after 0, 1, 2, 5 and 10 cycles of boiling water cycling. Cycles consisted of 2min of boiling DI water and 1min cooling in room temperature DI water.**

### 6.2.7 Acid attack

Acid rain is common in many cities around the world. To test the acid resistance of the MAR coatings, samples were submerged in dilute sulphuric acid[97] with ~3.5pH. The type of acid and pH were selected to simulate acid rainwater[98]. The pH was measured using an Accumet AB150 pH meter. The WAR of the coating was measured after every 30 minutes of exposure. Figure 6.23 shows that the WAR of the coatings was not reduced after acid attack and demonstrates that the coating is resistant to acid rain.

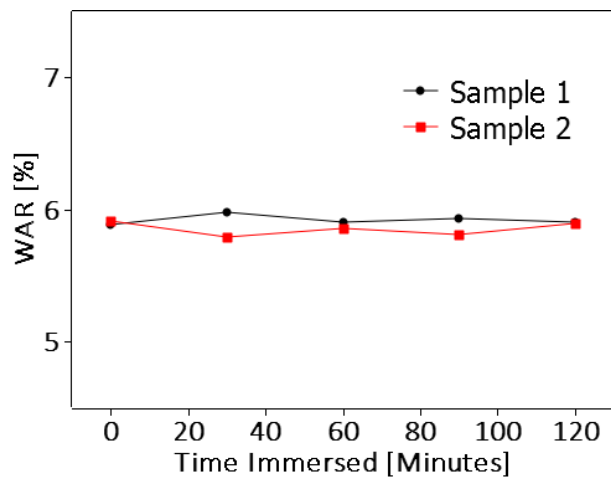


**Figure 6.23: The weighted average reflectance (WAR) of sputtered  $\text{SiO}_2/\text{ZrO}_2$  MAR samples after exposure to dilute sulphuric acid simulating the effect of acid rain for 0, 30, 60, 90, and 120mins.**

### 6.2.8 Abrasion resistance

It is necessary for MARs to be abrasion resistant to simulate the effect of transport, handling, maintenance, cleaning and falling debris in certain environments. Abrasion resistance was measured using a reciprocating abrader adapted from BS EN 1096-2[97]. Materials such as cheesecloth [93] and felt pads[97], are used as abrasers as industrial standards for optical coatings to simulate the effect of cleaning. A felt pad abrasion test from BS EN 1096-2 (which uses a slow turning circular abrader) was adapted into a linear abrasion test. In the adapted test, a felt abrader with a surface area of  $\sim 7.5\text{mm}^2$  was applied to the surface of the MAR coating with a force of 10N and passed across the surface 100 times, with a stroke length of 30mm and a speed of 60 cycles per minute. Though more aggressive than the circular test found in BS EN 1096-2, the felt pad test caused no visible damage and had no effect on the WAR of MAR coated samples.

A CS-10 abrader[99], a rubbery material with sand like grains within it, which produces a mild to medium abrasion, was used to further test the durability of MAR coatings. The CS-10 abrader was pressed to the surface of the MAR coated glass with a force of 5N and 10N. The abrader was then repeatedly passed over the sample surface at 60 cycles per minute with a stroke length of 30mm. After 100 cycles at each force, the coatings were cleaned in an ultrasonic bath and the WAR was measured.

After the abrader was applied to the surface of the MAR the WAR was slightly reduced, by 0.2% and 0.4% for 5N and 10N respectively. The reduction in WAR is due to minor damage to the MAR coating. CS-10 abrasion is an aggressive test for optical coatings but the coating sustained only minor scratches. This demonstrated that the coatings can pass all industrial abrasion resistance standards for optical coatings and confirms the excellent durability of the MAR coatings.

### 6.2.9 Scratch Resistance

The scratch-resistance of the MAR coatings was measured using micro-indentation with a micro-scratch test [100]. The micro-scratch test is used to measure hardness using a diamond micro-indenter which is pressed into the surface of the sample using an increasing load. The surface of the sample then moves relative to the micro-indenter, scratching the surface. Recording the force at which the coating is penetrated, deforms elastically and inelastically, and begins to flake, provides a quantitative measurement of the scratch-resistance of a coating. Additionally, images of the scratches provide qualitative evidence of the extent of the damage. For example, images show the size of flakes from the coating, and the size and number of fractures caused by the scratches.

A round end cone micro-indenter with a tip radius of  $5\mu\text{m}$  was used. Initially, the micro-indenter was held at a force of 0.1mN at the surface of the sample. The load was then increased at a rate of 1mN per  $1\mu\text{m}$  as the micro-indenter travelled across the surface. The micro-indenter travelled  $400\mu\text{m}$  and applied a maximum force of 400mN over the  $5\mu\text{m}$  micro-indenter tip,  $\sim 5\text{kPa}$  pressure.

An image of the resulting scratch from the micro-scratch test is shown in Figure 6.24. The image shows that debris begins to appear next to the scratch at about  $\sim 120\text{-}140\text{mN}$ : this is the point at which partial delamination of the sample begins to occur. This point on the scratch is indicated in Figure 6.24 with a label reading 'Delamination initiates'. It is probable that the top layers of the coating failed, and the debris observed is likely to be from the top layers of the coating. At  $\sim 200\text{-}220\text{mN}$  it appears that the debris from the

coating is much larger and displays interference effects, which indicates that the coating has begun to delaminate as a whole rather than in layers. In Figure 6.24, this point is indicated by the label reading ‘Total delamination occurs’. There are no cracks protruding from the scratch and the flake size is very small. This confirms the coating is very hard and structurally sound.

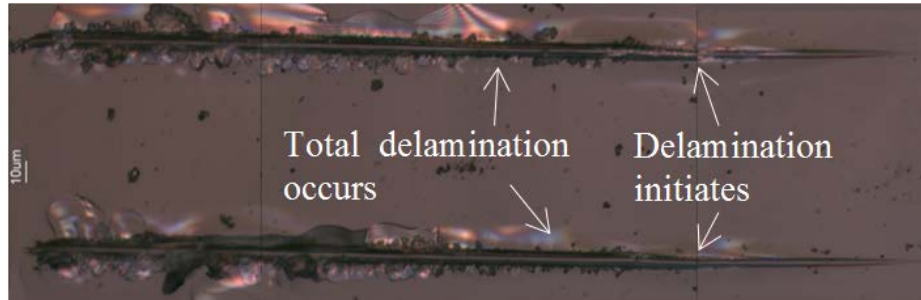


**Figure 6.24: Scratches in the surface of a sputtered  $\text{SiO}_2/\text{ZrO}_2$  MAR sample. The scratches were produced by pressing a micro-indenter into the surface of the coating and moving the sample as the load is increased.**

The dependence of the penetration depth on applied load is shown in Figure 6.25. Throughout the scratch process, the relationship between applied load and scratch depth remains linear, except for a few slight variations at the coating failure. This indicates that the resistance to deformation of the coating is similar to that of the glass substrate.

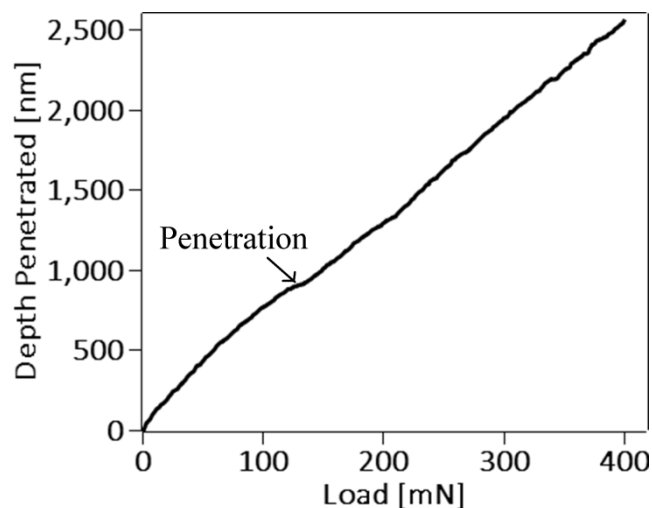


**Figure 6.25: Plot of the load applied to the micro-indenter against depth penetrated into the surface of the sputtered  $\text{SiO}_2/\text{ZrO}_2$  MAR sample.**

## 6.3 Durability of the Sol-gel Coatings

### 6.3.1 Adhesion

#### 6.3.1.1 Pull Test

As with the MAR coatings, the Positest Adhesion tester was applied to AR1 and the TWI porous silica coating. In both cases the glass substrate failed and the coating was not removed from the substrate surface. When testing the TWI coatings, the adhesive permeated the coating and adhered to the glass surface itself. The coating is extremely friable due to the porous nature of the coating.

Pull tests for AR1 were carried out using a dolly size of 20mm, with the standard ethyl-2-cyanoacrylate based adhesive. The dollies were sanded with 120 grit sandpaper and were glued 6 days prior to testing. The dollies were pulled at a rate of 0.7MPa/s. The coating withstood a maximum load of 4.92MPa before the glass substrate failed. Figure 6.26 shows the glass substrate cracked and still partially stuck to the dolly (~45%). The glue is on the remaining surface of the dolly and was removed from the surface of the coating. Across the entire surface of the glass the coating was still intact—this result shows that AR1 has impressive adhesion. The failure of the glass substrate happens at a greater pull load when compared to MAR coatings, as the substrate was 3mm rather than 1mm thick.

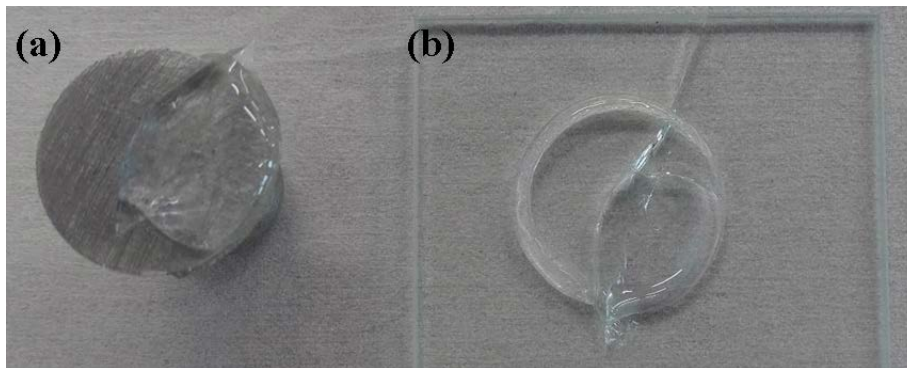


**Figure 6.26: (a) The base of a dolly with glass adhered to the surface, indicating no coating delamination. (b) A fractured sample of AR1 on glass after a pull test. The coating remained undamaged.**

#### 6.3.1.2 Cross-Hatch Test

The TWI porous silica coating was removed by the application of tape alone, resulting in an adhesion score of 5. In contrast, AR1 displayed no visible damage after the cross-hatch test. However, the coating could be scratched using the standard stainless steel 4-

bladed knife. AR1 has a score of 0 according to ISO 9211-4 [93], indicating excellent adhesion, as with the MAR.

### 6.3.2 High temperature stability

As the TWI coatings are simple dip-coated porous silica, heat treatment is used to aid the evaporation of the solvent. However, the effect of heat treatment has a negligible effect on the coating's effectiveness up to the temperature at which the glass melts. AR1 has a complex structure with internal bubbles. The AR1 coatings were heated at 100°C intervals up to 600°C. Untreated AR1 is featureless, but only minor heat treatment appears to damage the optical properties of the coating. Figure 6.27 shows that damage begins to occur in the coating after just 100°C heat treatment and Figure 6.28 shows that severe damage is established by 200°C.

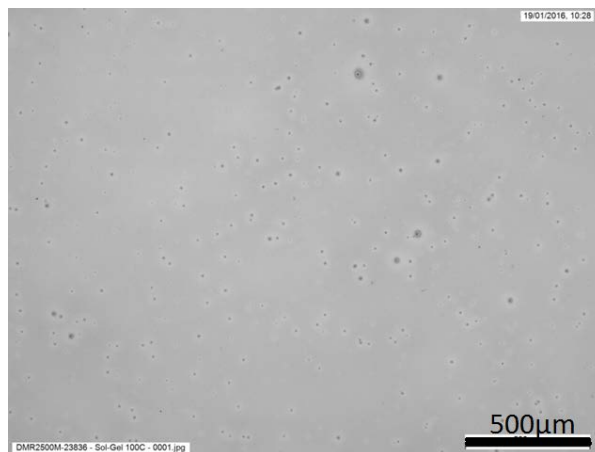


**Figure 6.27: The surface of an AR1 sample after heat treatment at 100°C for 30min.**

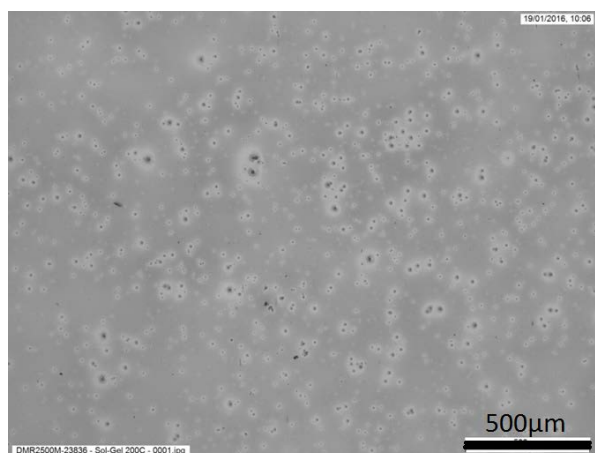


**Figure 6.28: The Surface of an AR1 sample after heat treatment at 200°C, showing high damage for 30min.**

However, across the 350nm to 850nm wavelength range, the WAR of the samples had decreased from 2.6% to 2.28% after exposure to 400°C and 2.02% after exposure to 500°C. Figure 6.29 shows that bubbles formed within the AR1 coating, causing the increase in WAR. After exposure to 700°C, the WAR had increased to 3.2%; a sample is shown in Figure 6.29.

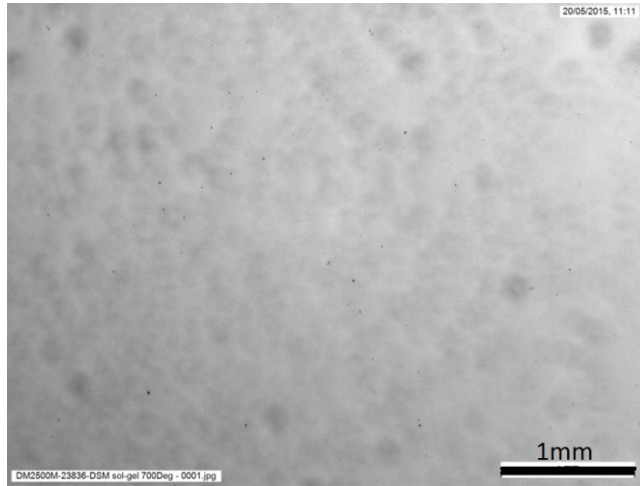


**Figure 6.29: The surface of an AR1 sample after exposure to 700°C for 30min.**

### 6.3.3 Resistance to temperature and humidity

In accordance with IEC 61646, 2 samples of AR1 were loaded into an environmental chamber (Sanyo Gallenkamp) and held at 85°C and 85% RH for a total of 1000 hours. The reflectance of the samples was measured using a spectrophotometer at the beginning and end of the 1000 hours, and at the mid-way point at 500 hours. Table 6.3 shows the result of DH exposure on 2 AR1 samples. Before each measurement the samples were cleaned in a 50-50 IPA and DI water mix, to localise the effect of the DH test.

**Table 6.3: Measured WAR of AR1 samples after DH exposure:**

	Sample 1	Sample 2
Initial	2.25%	2.35%
500 hours	2.25%	2.23%
1000 hours	3.19%	2.85%

After 500 hours, the change in WAR was negligible. After 1000 hours, the WAR of the samples had increased considerably. The WAR of sample 1 and 2 had increased by

0.94% and 0.62% —this indicates that the coating is susceptible to damage from hot and humid environments. The surfaces of the samples appeared to have collected impurities from the DH test. The WAR, after 500 hours, was not affected since these impurities were not abundant. However, after 1000 hours, the impurities are clearly visible with the naked eye, as shown in Figure 6.30.

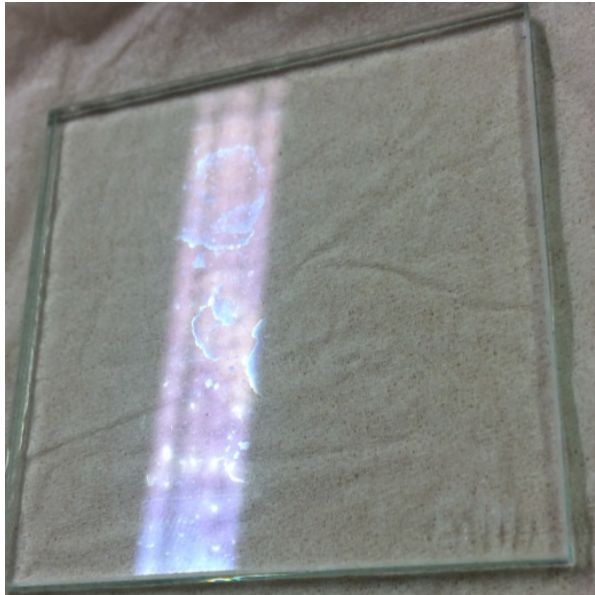


**Figure 6.30: Photograph of sample 1 showing signs of water damage after 1000hrs of DH exposure.**

#### 6.3.4 Contact angle

The contact angle of the TWI ARC was measured at  $100^\circ$  and slightly increased by the application of HMDS to  $111^\circ$ . Porous silica is the most hydrophobic coating studied in this work. A water drop on the surface of a TWI ARC before and after the application of HMDS can be seen in Figure 6.31 and Figure 6.32 respectively. The high hydrophobicity can be explained by the roughness of the coating on the glass preventing the water drop from moving on the surface. In the long term, however, the TWI coatings wash off the surface of the glass due to their high friability.

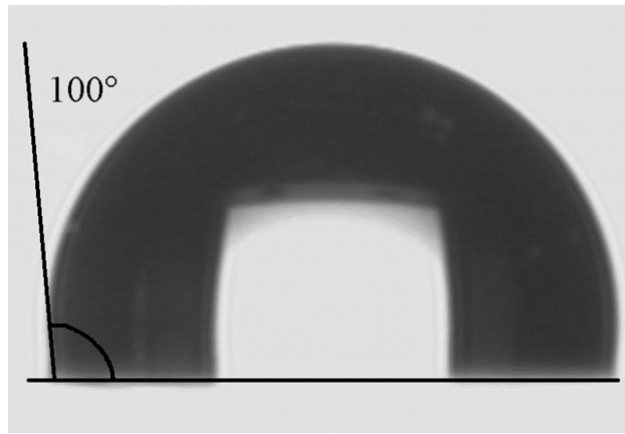


**Figure 6.31: A water drop on the surface of a TWI ARC with a contact angle of 100°.**

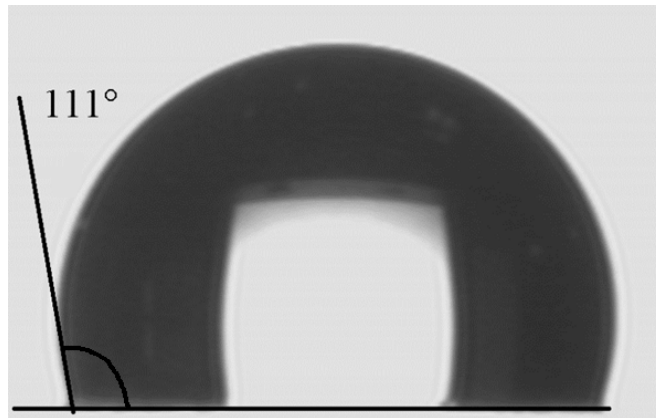


**Figure 6.32: A water drop on the surface of a TWI ARC coated in HMDS, the contact angle is 111°.**

The contact angle of AR1 was measured at 9°, which is very low. The coating appears to absorb water. This is a concern for the long term effectiveness of AR1 coatings: if the coating absorbs water, the optical properties are diminished as the presence of water raises the refractive index of the coating. The application of HMDS increased the contact angle drastically to 89°, so the application of a hydrophobic layer (thin enough to have a negligible effect on the optical properties of the ARC) may be a solution. A water drop on the surface of AR1 and HMDS coated AR1 is shown in Figure 6.33 and Figure 6.34 respectively.

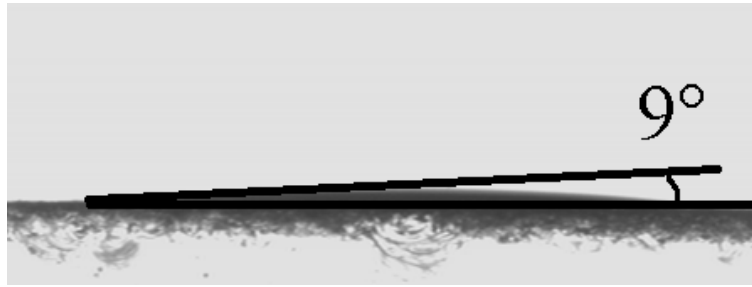


**Figure 6.33:** A water drop on the surface of an AR1 with a contact angle of 9°.

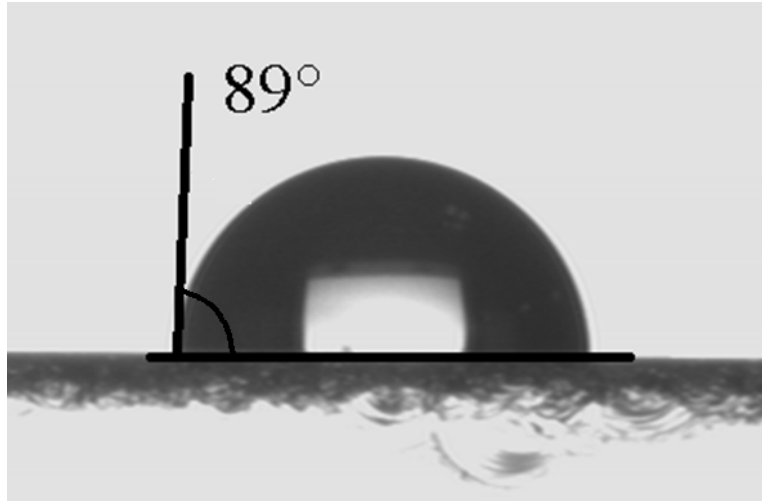


**Figure 6.34:** A water drop on the surface of an AR1 coated in HMDS. The contact angle is 89°.

### 6.3.5 Stability against thermal cycling

As with the MAR samples, samples of AR1 were exposed to thermal cycling in accordance with IEC 61646. The samples were loaded into a Vötschtechnik VCS 7430-4 environmental chamber and cycled between -40°C and 85°C, with a minimum dwell time of 10 minutes at each temperature. As shown in Figure 6.35, thermal cycling had a positive effect on the WAR of the samples, indicating that the samples are resistant to thermal damage. However, the change in WAR suggests the mechanical properties may have been compromised. This result agrees with the resistance to remarkably high temperatures demonstrated in section 6.3.2.

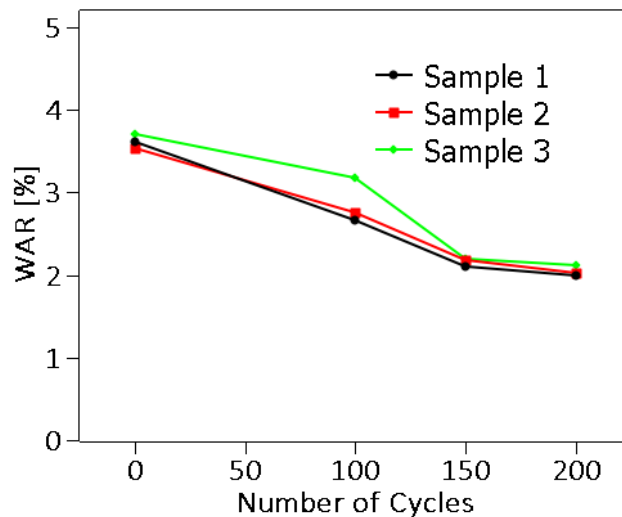


**Figure 6.35: The measured WAR of AR1 samples cycled 0, 100, 150, and 200 times between -40°C and 85°C in a climatic chamber (~33Hrs).**

Due to the small surface area of the AR1 samples (5cm<sup>2</sup>), irregularities in the coating can lead to the initial WAR can vary considerably from sample to sample. Nevertheless, when considering the effect of thermal cycling, the difference in WAR before and after the treatment is still meaningful when discussing the effects of thermal cycling.

### 6.3.6 Water Solubility Test

As with the MAR coatings, AR1 samples were exposed to solubility tests sequentially in accordance with ISO 9211-4. The least aggressive test is the immersion of the samples into DI water for up to 96 hours. After immersion the samples were dried and the reflectance of the sample was measured. The WAR of AR1 samples was raised slightly, as shown in Figure 6.36. The WAR is raised after 6 hours immersion, and then remains constant for the remainder of the experiment. This suggests that slight damage occurs after very little contact with water. The WAR of the sample was measured after 6, 24, and 96 hours.

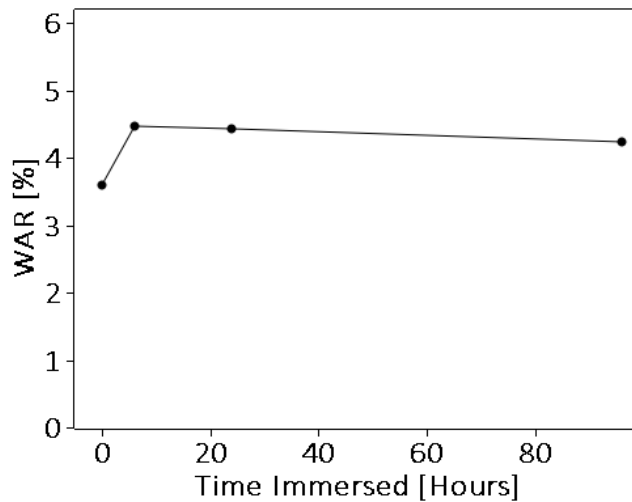


**Figure 6.36: The WAR of AR1 samples after immersion in DI water for 0, 6, 24, and 96Hrs.**

The samples were then placed in boiling DI water for 5, 15, and 30 minute periods. No physical degradation was observed after 30 minutes. The WAR of the sample improved after 5 minutes in boiling water, after this point a slight increase in WAR was observed, as shown in Figure 6.37. This is consistent with heat having a positive effect on coating uniformity and suggests that damage from water occurs in a timescale of hours.

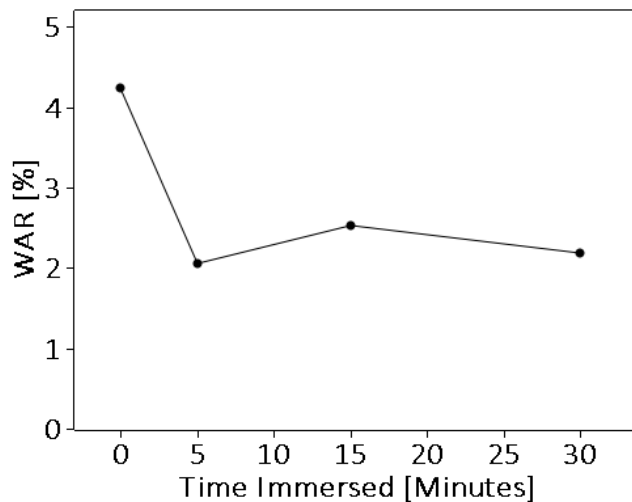


**Figure 6.37: The WAR of AR1 samples after immersion in boiling DI water for 0, 5, 15 and 30mins.**

Finally, the samples were placed in boiling DI water for 2 minutes and then immersed in room temperature DI water for 1 minute. This process was repeated 10 times and WAR measurements were taken after the 1<sup>st</sup>, 2<sup>nd</sup>, 5<sup>th</sup>, and 10<sup>th</sup> cycle. The samples displayed no visible degradation in quality. However, the WAR was increased after the first cycle. The WAR of the samples is shown in Figure 6.38.

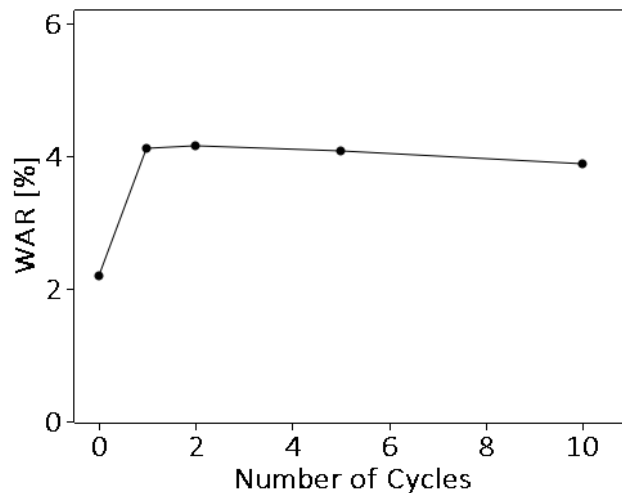


**Figure 6.38: The WAR of samples of AR1 after 0, 1, 2, 5, and 10 cycles of 2 minutes in boiling DI, followed by 1 minute in room temperature DI water.**

### 6.3.7 Abrasion Resistance

A felt pad abrasion test from BS EN 1096-2 [97] (which uses a slow turning circular abrader) was adapted into a linear abrasion test. In the adapted test, a felt abrader with a surface area of  $\sim 7.5\text{mm}^2$  was applied to the surface of the AR1 coating with a force of 10N and passed across the surface 100 times, with a stroke length of 30mm and a speed of 60 cycles per minute. This increased the WAR of the sample relatively by 33% from 2.75% to 3.65%.

The CS-10 abrader was pressed to the surface of AR1 samples with a force of 5N and 10N. The abrader was then repeatedly passed over the sample surface at 60 cycles per minute with a stroke length of 30mm. After 100 cycles at each force, the coatings were cleaned in an ultrasonic bath and the WAR was measured. This resulted in an absolute increase in WAR of 1.32% and 2.21% for 5N and 10N respectively. The reduction in WAR is due to severe damage to the AR1 coating. This result suggests damage from wear and tear during operational cleaning is to be expected when using AR1 as a commercial anti-reflective coating.

### 6.3.8 Scratch resistance

As with the MAR coatings, a round end cone micro-indenter with a tip radius of  $5\mu\text{m}$  was used. The micro-indenter was held at a force of 0.1mN at the surface of the sample, and then the load was increased at a rate of 1mN per  $1\mu\text{m}$  as the micro-indenter travelled across the surface. The micro-indenter travelled  $400\mu\text{m}$  and applied a maximum force of 400mN over the  $5\mu\text{m}$  micro-indenter tip,  $\sim 5\text{kPa}$  pressure.

An image of the resulting scratch from the micro-scratch test is shown in Figure 6.39. The resting pressure of 0.1mN deformed the coating considerably in comparison with MARs, deforming the coating by ~30nm compared to ~0.5nm with an MAR. Figure 6.39 shows that debris begins to appear next to the scratch very early, implying partial delamination at ~20-40mN. This point on the scratch is indicated in Figure 6.39, with a label reading 'Delamination initiates'. At ~180-200mN it appears that the debris from the coating is much larger and displays interference effects, which indicates that the coating has begun to delaminate completely. In Figure 6.40, this point is indicated by the label reading 'Total delamination occurs'. There are no cracks extending from the scratch, implying the coating is structurally sound. However, the flake size is larger than that produced by the MAR scratch test. The greater amount of debris is explained by the greater thickness of the AR1, and the deeper penetration into the softer AR1 surface.

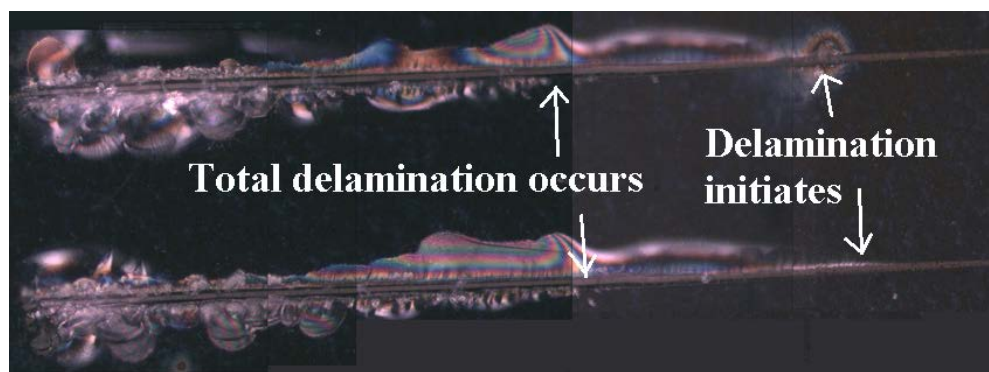


**Figure 6.39: Scratches in the surface of an AR1 sample. The scratches were produced by pressing a micro-indenter into the surface of the coating and moving the sample as the load is increased.**

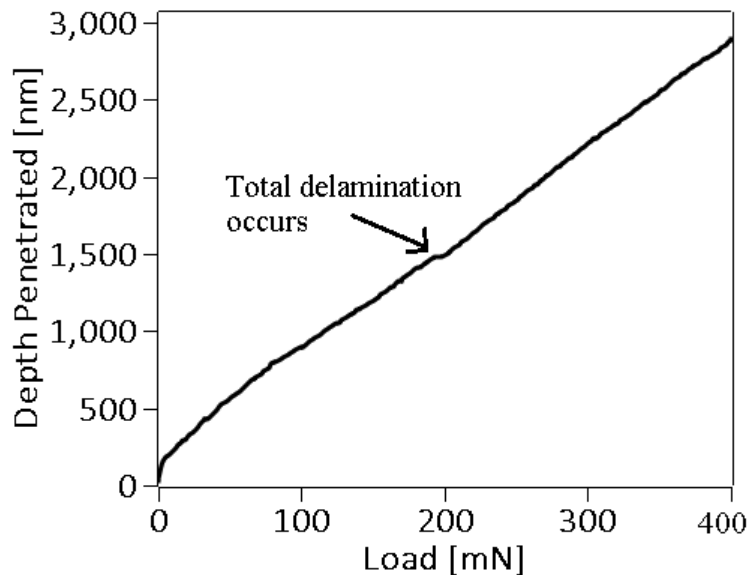


**Figure 6.40:** Plot of the load applied to the micro-indenter against depth penetrated into the surface of the AR1 sample.

## 6.4 Summary and Conclusions

The adhesion and durability of the coating is a primary concern. Solar modules are installed with a 25 year warranty even in countries with harsh climates. Not only is the coating expected to withstand humidity and temperature cycling, it may also endure dilute acid attack from atmospheric pollution. Furthermore, the coating must have sufficient scratch resistance to withstand regular cleaning and maintenance.

The adhesion of the MAR and AR1 coatings have been tested using a battery of standardised tests. The pull test (ISO 4624) failed to remove both types of coatings from the substrate. The highest recorded pull strength that the coating survived was 0.98MPa for MAR and 4.92MPa for AR1 (due to a thicker substrate). The substrate was destroyed in both instances. The cross-hatch test (ISO 9211-4), typically requires a 4-bladed steel knife to scratch the samples, but this had to be adapted and a diamond tool was used to scratch the grid pattern into the coating. Very little delamination from the application and removal of tape was observed in both coatings. In addition to these standard test methods, a micro-indentation scratch test was carried out on the candidate coatings. The micro-indentation scratch test showed that the MAR coating has similar hardness to the glass substrate, confirming exceptional adhesion to the glass surface. AR1 was more easily penetrated and deformed by the scratch test.

It may be cost-effective for MAR coatings used on solar modules to be readily available to PV manufacturers on pre-coated glass. This would be ideal for cover glass

applications for crystalline silicon, thin film amorphous silicon, CIGS, CZTS, or superstrate perovskite devices. However, for this to be feasible for thin film CdTe devices using the conventional superstrate configuration, the coatings must be resistant to the temperature levels used at every stage of the thin film CdTe PV manufacturing process. This study has shown that both the magnetron sputtered coatings and the commercial sol-gel coatings are heat resistant and begin to craze at temperatures greater than those used in the CdTe absorber deposition and activation processes (~500°C). The first signs of crazing of MAR samples on soda lime glass were observed at 590°C, as the glass substrate began to deform beneath the coating, applying mechanical stress. Applying the coating to Eagle glass<sup>®</sup> (which has a lower coefficient of thermal expansion) confirms that the coating crazes once the underlying glass deforms at 800°C. The WAR of the MAR coated surfaces was unaffected by heat treatment, even after crazing. The resistance of the MAR coatings to extreme heat makes its application attractive for all PV technologies. Heat treatment of samples of AR1 coatings had no adverse effect on WAR, until heat treatment temperatures well exceeded 500°C. Beyond 700°C, bubbles within the coating appeared to form.

Temperature and humidity thermal cycling, contact angle, and acid attack tests resulted in no degradation of the MAR coating quality. This confirms that MAR coatings are suitable for use in any climate —tropical or otherwise— and are even suitable for use in areas of high ambient pollution. AR1 performed well in all experiments that involved exposure to high temperatures; however, the coating is vulnerable to water ingress and has a very low contact angle.

The combination of tests presented in this work demonstrates the remarkable robustness of MAR coatings. The 3.6% increase in relative conversion efficiency, available by using pre-coated glass superstrates, is also an attractive feature. Its use would add a further ~100MW of capacity to the current ~3GW of thin film CdTe production without any physical modification to the manufacturing line. It would also have no effect on the manufacturing time.

The cost of MAR coatings on cover glass or superstrate glass configurations could be reduced dramatically at high volumes. Although we have used planar magnetrons, it is feasible to use sputtering sources such as rotatable magnetrons with higher target utilization and deposition rates. These are the standard in large scale industrial glass coaters[101].

The dielectric metal-oxide multilayers used in MARS have remarkable durability, adhesion, and resistance to environmental factors. Not only do they increase the power output of solar modules, their mechanical properties are consistent with a long warranty—even when exposed to regular cleaning cycles and maintenance.

# 7 MODELLING OF INTERFERENCE EFFECTS IN CdTe

## 7.1 Introduction

Thin film CdTe solar cells have achieved commercial success through low manufacturing costs and increasingly high efficiencies. Energy conversion efficiencies of 22.1% have been reported for thin film CdTe solar cells [102]. However, the theoretical efficiency limit for this type of device is ~30% [103]. Both optical and electrical losses occur in CdTe solar cells. Electrical losses are normally of greater magnitude than optical losses, but if light fails to reach the active layer of the stack, a photocurrent is not generated. As such, optical losses precede electrical losses, imposing limitations on photocurrent if not addressed. The losses occur due to reflection and light absorption in layers which do not contribute to the photocurrent, such as the CdS window layer [104].

Light interference effects occur in the multilayer structure of the cell. The reflection losses can be controlled and reduced by tuning the thickness of individual layers to achieve an interference minimum. The absorption losses in the window layer can be reduced by thinning the window layer thickness, which usually requires use of a high resistance transparent layer to prevent voltage and shunt losses [105]. Optical modelling has been used to assess the optical losses within the CdTe solar stack in a simpler model [106], and to evaluate internal reflection losses in a-Si solar cells [107]. In this work,

optical modelling was used to investigate how optimizing the various layer thicknesses can increase light transmission to the CdTe absorber layer to increase the photocurrent generated.

### 7.1.1 The thin film CdTe solar cell

The CdTe solar cell is a thin film stack with a total thickness typically  $\sim 3\mu\text{m}$ . For commercial modules, the layers are deposited on to a low cost soda lime glass substrate coated with a transparent conducting oxide (TCO). NSG Pilkington TEC glass is an industrial standard substrate. The TEC glass consists of  $\text{SnO}_2$ ,  $\text{SiO}_2$  and  $\text{SnO}_2:\text{F}$  layers deposited on 3.2mm thick float glass. Depending on the properties required, there are different types of TEC glass characterised by different light transmission, sheet resistance, and surface roughness. TEC 10 glass is an option for CdTe solar cells. The glass is characterised by 70% light transmission in the AM1.5 solar spectrum and a  $9\ \Omega/\square$  sheet resistance [108].

The CdTe solar cell is deposited onto a TCO coated glass. A simple cell structure consists of CdS-CdTe hetero-junction and a back contact. The CdS layer is usually  $\sim 100\text{nm}$  thick. The CdS acts as an n-type semiconductor and enables the photovoltaic effect in the solar cell. The band-gap of CdS is 2.4eV which corresponds to an absorption edge at  $\sim 500\text{nm}$ . The photons absorbed in the window layer do not contribute to the photocurrent of the solar cell, as recombination is very likely to occur, resulting in scattering of light. Therefore, absorption in the CdS layer is a source of significant loss. In a typical cell utilizing CdS, the photocurrent is limited to  $22\text{--}23\text{mA}/\text{cm}^2$ , although  $31\text{mA}/\text{cm}^2$  is available in the spectrum utilised by CdTe absorber [109], [110].

CdTe is a semiconductor material with a band-gap of 1.45eV which corresponds to an 850nm absorption edge. Soda lime glass absorbs light at wavelengths of 350nm and below [111]. Optically, therefore, the CdTe device absorbs wavelengths between 350nm and 850nm.

The ideal refractive index of a typical single layer anti-reflection coating, to maximise transmission, is the product of the refractive indices of the materials at the media interface, square rooted as seen in equation (2.26).

### 7.1.2 High resistance transparent (HRT) buffer layers

High resistance transparent buffer layers have been shown to improve solar cell efficiencies by reducing the necessary thickness of the CdS layer and reducing shorting through the CdS layer [113], [114].

The buffer layer is located between the CdS layer and the fluorine doped tin oxide TCO layer. The refractive indices are 1.9 and 2.5 respectively, at the maximum in the AM1.5 spectrum  $\sim 550\text{nm}$  wavelength. Using equation (7.1, the ideal refractive index to maximize transmission at a wavelength of  $550\text{nm}$  is  $\sim 2.2$ . The refractive indices of ZnO and SnO<sub>2</sub> are 2.0 and 1.9 respectively. As the refractive index of ZnO is closer to that of an ideal anti-reflection layer in the  $350\text{nm}$  to  $850\text{nm}$  region, the destructive interference of reflections from different interfaces within the system is more complete. This results in lower reflection minima when ZnO is implemented as the buffer layer.

Bulk SnO<sub>2</sub> is a transparent n-type semiconductor with a band-gap of  $3.6\text{eV}$  and a refractive index of  $\sim 1.9$  at  $550\text{nm}$  [115], [116]. Thin film SnO<sub>2</sub> has been used as a HRT buffer layer in CdTe solar cells at a variety of thicknesses between  $12.5\text{nm}$  and  $100\text{nm}$  [117]. Figure 7.1 shows the structure of a thin film CdTe solar cell incorporating an HRT buffer layer. It has been shown that the inclusion of a SnO<sub>2</sub> HRT buffer layer in a standard CdTe/CdS solar cell, with Fluorine doped tin oxide transparent conducting oxide, leads to a  $90\text{mV}$  improvement to open-circuit voltage ( $V_{oc}$ ) and a  $6\%$  improvement in Fill Factor [117]. The inclusion of a SnO<sub>2</sub> HRT buffer layer has a negligible effect on spectral response and  $J_{sc}$ , whilst raising the shunt resistance of the device [117].

An alternative HRT buffer layer material to SnO<sub>2</sub> is Zinc Oxide (ZnO). The refractive index of ZnO at  $550\text{nm}$  is  $\sim 2.0$  and the band-gap of ZnO is  $\sim 3.3\text{eV}$  [118]. ZnO has been modelled previously as a HRT buffer layer in CdTe solar cells using a thickness of  $115\text{nm}$  [119]. The addition of a ZnO HRT buffer layer has been shown to be beneficial to CdS/CdTe solar cell efficiency [120]. ZnO has also been used as a HRT buffer layer in Cu(InGa)Se<sub>2</sub> (CIGS) solar cell devices [121].

The dispersion relationships and absorption coefficients of SnO<sub>2</sub> and ZnO are shown in Figure 7.2 and Figure 7.3 respectively.



**Figure 7.1:** A schematic diagram of the CdTe solar cell structure showing the position of (from bottom to the top), the back contact, the CdTe absorber, the CdS window layer, the buffer layer, the TCO layer, and the glass substrate.

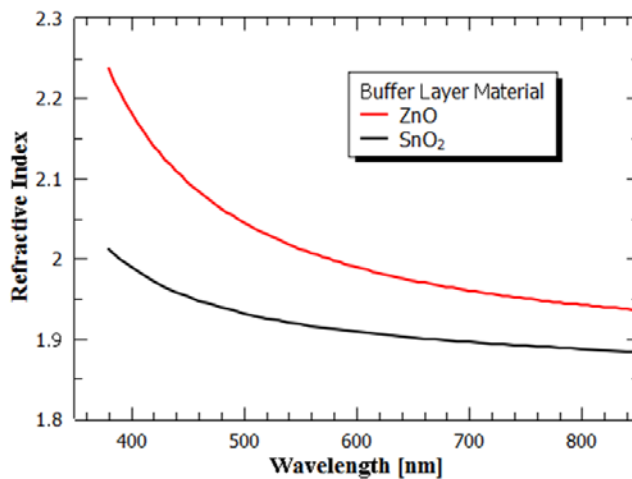


**Figure 7.2:** The refractive index dispersion for SnO<sub>2</sub> and ZnO, the candidate high resistance buffer layer materials.

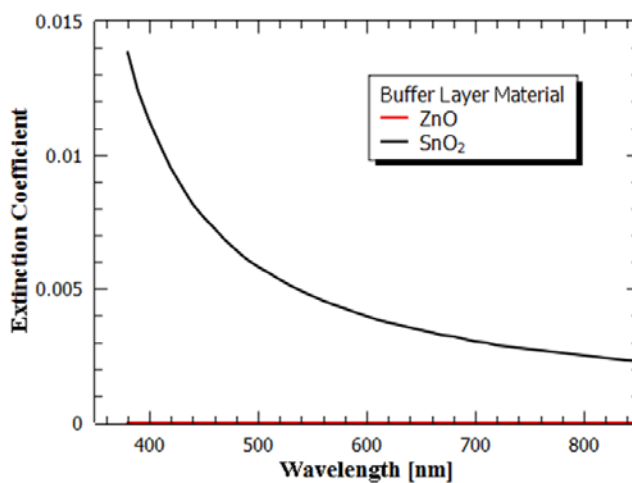


**Figure 7.3:** The extinction coefficients of SnO<sub>2</sub> and ZnO, the candidate high resistance buffer layer materials.

## 7.2 Optical modelling

The thin film CdTe solar cell was modelled and optimised for maximum light transmission to the CdTe layer, using software based on the transfer matrix method [28]. The performance of the solar cells was assessed by calculating the weighted average transmission (WAT) of light into the CdTe absorber in the 350nm – 850nm spectral range, by incorporating the photon flux in the AM1.5g solar spectrum ( $\Phi$ ) [83].

$$WAT(\lambda_{max}, \lambda_{min}) = \frac{\int_{\lambda_{min}}^{\lambda_{max}} \Phi \cdot T d\lambda}{\int_{\lambda_{min}}^{\lambda_{max}} T d\lambda} \quad (7.1)$$

Initially, a simple solar cell consisting of TEC10 substrate with a CdS (thickness 50nm - 300nm) and CdTe junction was modelled for comparison. Complete light absorption in the CdTe layer was assumed. Such devices can usually achieve ~12% conversion efficiency with a photocurrent of 22mA/cm<sup>2</sup> [103], [105]. The effect of the addition of a HRT buffer layer on the optical performance was then modelled. Because thicknesses below 50nm are not electrically viable, the buffer layer materials initially were investigated at thicknesses in the range 50nm to 500nm. However, low thickness HRT buffer layer interference effects were investigated at select thicknesses of CdS, despite being electronically unsuitable. TEC 10 glass has a sheet of fluorine doped tin oxide (FTO) with a sheet resistance of 9Ω/□ and a thickness of 350nm. Therefore, to create an accurate model of a possible CdTe cell design the TCO layer was modelled as a FTO layer at a thickness of 350nm.

The refractive index and extinction coefficient data for CdS and SnO<sub>2</sub> were measured using a Horiba, Jobin Yvon, UVISEL Spectroscopic ellipsometer. The refractive index and extinction coefficient for ZnO was obtained from Sun and Kwok [122]. The refractive index and extinction coefficient values for CdTe were taken from the Handbook of the Optical Constants of Solids I [123].

## 7.3 Results

### 7.3.1 Varying the thickness of the CdS layer

The effect of modelling the variation in the thickness of the CdS layer was investigated. The effect of varying thickness was first modelled in a stack without a HRT buffer layer. The results are shown in Figure 7.4. The CdS thickness reduces light transmittance to the CdTe layer at all thicknesses. The thin film CdS is usually between

50nm and 150nm thick in CdTe devices [124]. Figure 7.4 shows that the optical transmission is highly sensitive to the thickness of the CdS layer. Transmittance is 77.9% at 50nm thickness, but at 300nm it reduces dramatically to 59.4%.

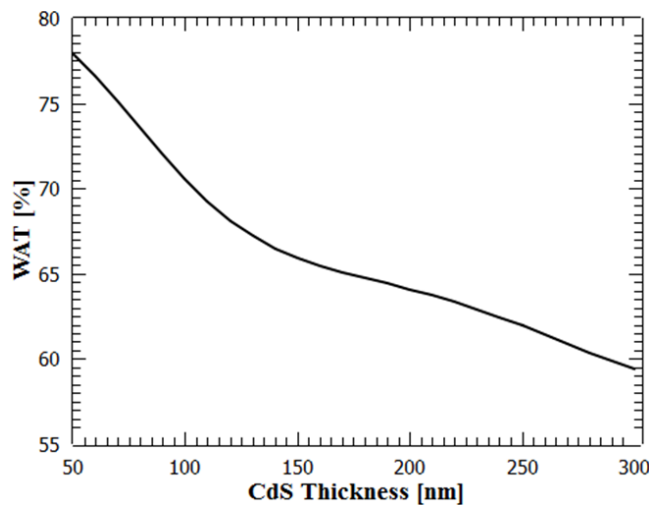


**Figure 7.4: The modelled optical weighted average transmission (WAT) to the CdTe layer in a CdTe photovoltaic device, plotted against the thickness of the CdS layer. The effect of a high resistance buffer layer is not included.**

### 7.3.2 Varying the thickness of the SnO<sub>2</sub> High Resistance Transparent buffer layer

The effect of a SnO<sub>2</sub> HRT buffer layer on transmittance was calculated by varying the thickness of the CdS layer between 50nm and 300nm at 10nm intervals, and by varying the thickness of the SnO<sub>2</sub> layer up to 500nm at 10nm intervals. The optical transmission into the active layer was calculated at each point and a 3D grid was generated from the data. The 3D plot is shown in Figure 7.5.

A maximum transmittance at a CdS thickness of 50nm was calculated to be 78.0% at a SnO<sub>2</sub> layer thickness of 50nm. At thicknesses greater than 70nm the absorbing properties of SnO<sub>2</sub> become more influential and the transmission to the absorber is reduced. Reducing the thickness of the CdS layer to below 50nm increases the transmittance. However, CdS thicknesses below 50nm have not been considered since layers this thin are likely to be discontinuous and lead to shorting of the cell [125].

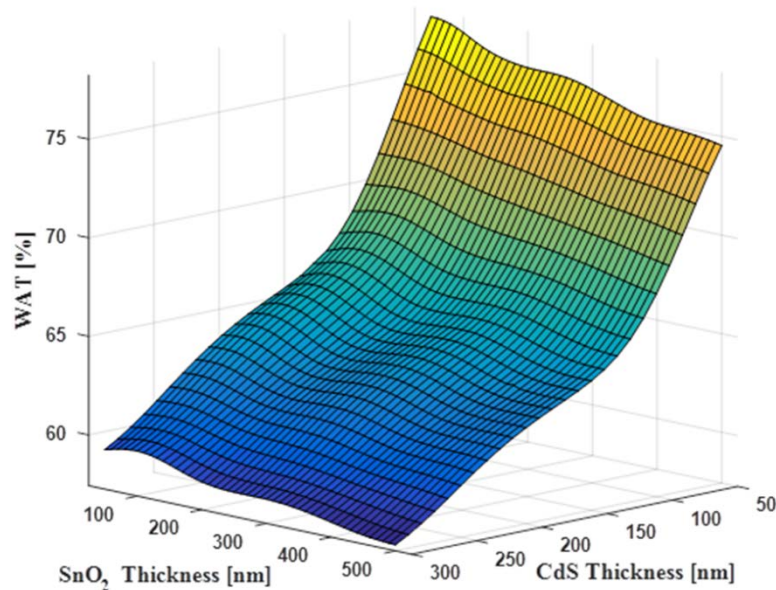


**Figure 7.5: The modelled WAT to the absorbing layer of a CdTe solar cell as a function of CdS and the SnO<sub>2</sub> layer thickness. Thicknesses of CdS and SnO<sub>2</sub> layers (nm) are plotted on the X-Y plane and the modelled value for WAT is plotted along the Z-axis. In this region a maximum transmission occurs at 50nm CdS and 48nm SnO<sub>2</sub>.**

In practice, it is important to be aware of the effect of thickness tolerance on transmission. It is possible to achieve thickness accuracy, using time control, of  $\pm 2\%$  with magnetron sputtering. Evaporation (thermal or electron beam) can be achieved with similar accuracy using quartz crystal control. Varying the thickness of the CdS and HRT buffer layer around the transmission maximum by 1nm (a variation of  $\pm 2\%$ ) results in an insignificant relative loss of 0.002% transmittance. This illustrates the sensitivity of transmission on layer thickness and also confirms that transmission is most sensitive to the CdS layer thickness. The dependence is predominantly flat, indicating that although there is an interference effect, it is not significant in terms of device design. The use of a SnO<sub>2</sub> HRT buffer layer is dictated more on its effect on Voc than any increase in transmission caused by engineering layer thicknesses.

### 7.3.3 Varying the thickness of the ZnO High Resistance Transparent buffer layer

The thickness of the CdS layer was again varied between 50nm and 300nm at 10nm intervals and the ZnO HRT buffer layer thickness was varied between 50nm and 500nm at 10nm intervals. A value for transmission to the active layer was calculated at each point and a 3D grid was generated from the data. The 3D plot in Figure 7.6 shows how

the use of ZnO as a buffer layer results in more significant interference effects. These effects maintain the transmission nearly level across all thicknesses of ZnO. Only a slight decrease in transmission is observed as the ZnO layer thickness is increased. It is also shown that, as with a SnO<sub>2</sub> HRT buffer, the CdS thickness has the greatest effect on transmission to the absorber when a ZnO HRT buffer is used.

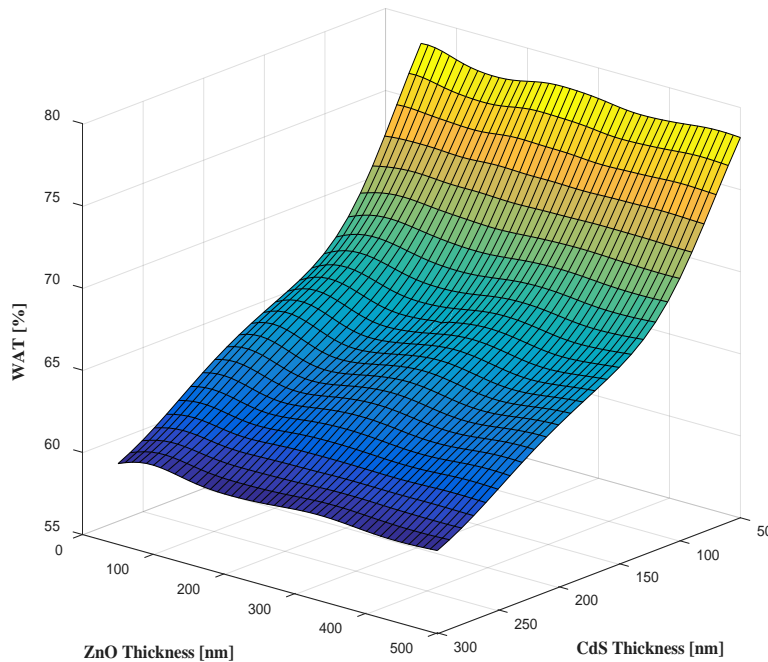


**Figure 7.6: The modelled WAT to the absorber layer for a CdTe solar cell with CdS window and a ZnO high resistance buffer layer. The thickness of the CdS and ZnO layers (nm) are plotted on the X-Y plane and the modelled value for WAT is plotted along the Z-axis.**

In general, the addition of a ZnO HRT buffer layer improves light transmission to the absorbing layer, with interference effects resulting in maximum transmission occurring at non-zero thicknesses. Interference effects result in maxima in transmittance at different thicknesses of ZnO at each thickness of the CdS layer. The ZnO layer does not suffer from significant absorption losses as occurs with SnO<sub>2</sub>, and therefore thicker HRT buffer layers can be used without significant losses.

A maximum transmittance at a CdS thickness of 50nm was calculated to be 78.5% at a ZnO thickness of 58nm. As with a SnO<sub>2</sub> HRT buffer layer, transmission values can be greater at CdS thicknesses less than 50nm due to the absorbing effect of the CdS layer, but these are disregarded as they are not considered practical. As with SnO<sub>2</sub>, variation of +/-2% in ZnO layer thicknesses results in an insignificant relative loss of 0.002%.

Therefore, the accuracy of layer thickness control during deposition is achievable with magnetron sputtering or evaporation techniques allied with quartz crystal monitoring.

The addition of a ZnO HRT buffer layer is beneficial to transmission at both 50nm and 100nm CdS thicknesses. The benefits are still present at ZnO thicknesses greater than 100nm, but interference effect maxima occur at different thicknesses of ZnO depending on the thickness of CdS. Consequently, a HRT buffer layer thickness that is beneficial at a CdS thickness of 100nm might be slightly detrimental or relatively less effective at a CdS thickness of 50nm.

#### 7.3.4 A comparison of the optical effects of introducing SnO<sub>2</sub> and ZnO high resistance buffer layers

A direct comparison of transmission to the absorbing layer with a ZnO HRT layer and a SnO<sub>2</sub> HRT layer is provided in Figure 7.7. Although buffer layer thicknesses below 50nm are usually unsuitable, for clarity Figure 7.8 draws out the comparison of the 2 candidate HRT buffer layer materials, highlighting the effect of interference when using thin layers.

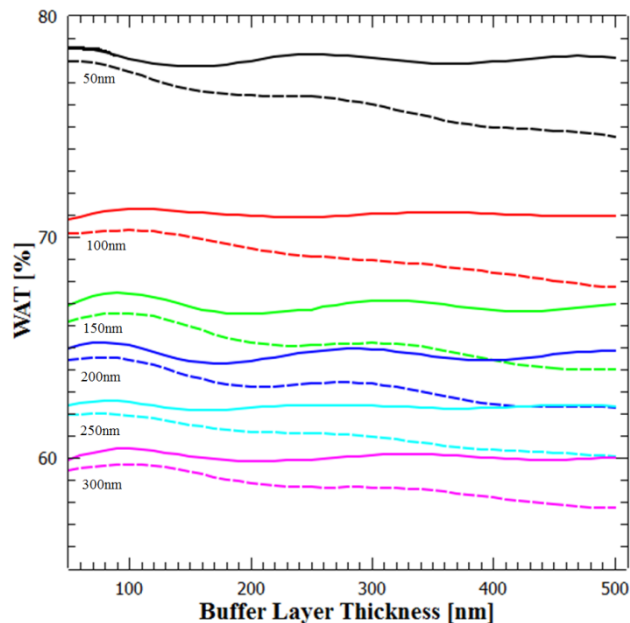


**Figure 7.7: Modelled WAT to the absorber layer of the CdTe stack plotted against thickness for the two candidate HRT layers. ZnO data is represented by solid lines and SnO<sub>2</sub> data is represented by dashed lines. Values are given at selected thicknesses of CdS layer; 50, 100, 150, 200, 250 and 300nm.**

The HRT buffer layer materials are compared at two CdS layer thicknesses often used in devices, 50nm and 100nm. The comparison shows that the use of ZnO as a HRT

buffer layer results in a greater transmission to the CdTe absorber, regardless of the respective thickness of the HRT buffer layer and the CdS layer. The use of SnO<sub>2</sub> is optically beneficial only at certain layer thicknesses.

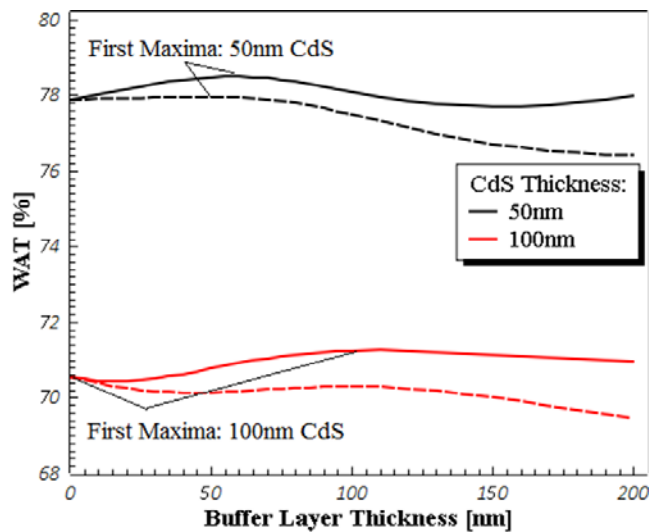


**Figure 7.8: Comparison of modelled WAT to the CdTe layer in the solar cell plotted against the thickness of the ZnO and SnO<sub>2</sub> buffer layers. The ZnO data is represented by solid lines and SnO<sub>2</sub> data is represented by dashed lines. Values are given at selected thicknesses of CdS layer; 50nm and 100nm.**

## 7.4 Conclusions

Table 7.1 provides a comparison of the optimization of the optical effects using a SnO<sub>2</sub> or ZnO high resistance transparent buffer layer above the transparent conductor in a thin film CdTe device. Optical interference occurs in the multilayer thin film stack design structure used in thin film CdTe photovoltaic devices. It also occurs in other thin film device structures such as CIGS, CZTS, amorphous Silicon, and perovskite solar cells. It is important to optimize layer thicknesses within the stack to engineer maximum light transmission to the absorber layer so that the highest possible photocurrent is produced. In order to achieve the thickness tolerance required in these optically active layers, control of the deposition rate is key to this process. When considering only optical effects, thickness control in the absorber layer is unimportant once complete absorption is achieved.

**Table 7.1: Comparison of HRT layer performance**

	ZnO	SnO <sub>2</sub>
Maximum WAT (CdS 50nm)	78.5%	78.0%
Buffer layer thickness at maximum WAT (optimum)	58nm	48nm
WAT at buffer layer 50nm thickness (CdS50nm)	78.5%	78.0%
Absolute transmission gain at optimum HRT layer thickness compared to no buffer layer at 50nm CdS	0.6%	0.1%
Relative maximum transmission loss due to a +/-2% thickness variation at maximum transmission	0.002%	0.002%

The maximum transmission possible using a SnO<sub>2</sub> HRT buffer layer was calculated to occur with 50nm of CdS and 48nm of SnO<sub>2</sub>. At these values, the beneficial interference effects of incorporating a SnO<sub>2</sub> layer increases transmission and outweighs the absorption effects within the SnO<sub>2</sub> layer. The transmission gained by optimising HRT and CdS layer thicknesses would lead to a gain in photocurrent of 0.6% for ZnO and 0.1% for SnO<sub>2</sub>. Incorporation of the optimised SnO<sub>2</sub> layer leads to a maximum weighted average transmission (WAT) of 78.0%. Varying the thickness of the HRT and CdS layers around maximum transmission by +/-2%, results in an insignificant transmittance loss of 0.002%. This tolerance is achievable by using magnetron sputtering, or thermal/electron beam evaporation using quartz crystal control.

The maximum WAT of 78.5%, using a ZnO buffer layer with a 50nm CdS layer, was calculated to occur using a thickness of 58nm. Therefore it is possible to use a thicker HRT layer for ZnO than SnO<sub>2</sub> which could have electrical benefits. Varying thickness of a ZnO HRT layer around maximum transmission by +/-2% also resulted in negligible losses, similar to those calculated for SnO<sub>2</sub> (0.002%). However, testing a layer thickness tolerance of +/-5nm (~+/-10%) resulted in an absolute WAT loss of 1%, which is significant. Therefore, layer thickness control is important.

The anti-reflection properties of a ZnO HRT layer are more pronounced than those for the SnO<sub>2</sub> HRT layer. This is due to better refractive index matching between the HRT layer, the window layer, and the TCO. Moreover, the ZnO HRT layer has low

absorption losses, so the interference effect can be exploited at greater thickness to minimize the reflection losses.

The work presented here has shown that the use of a ZnO HRT buffer generally results in a higher WAT than SnO<sub>2</sub> at all layer thicknesses. The maximum WAT transmission achievable is 78.5% which is 0.5% greater than the maximum achievable with SnO<sub>2</sub>. ZnO also has a greater maximum transmission at 58nm thickness compared to SnO<sub>2</sub> at 48nm thickness. The layer thickness of ZnO can be increased while still retaining increases in transmission. This is important in practice because one of the benefits of incorporating a high resistance layer is the prevention of shorting. This is more likely to be successful as the thickness of the high resistance layer increases.

It should be recognised that this work has considered only optical interference effects to maximize light transmission to the absorber layer, thereby maximising the current density. Electrical benefits also accrue from the insertion of a high resistance transparent buffer layer which increases Voc. Consequently, the choice of material will be influenced by a combination of optical and electrical effects.

# 8 OPTIMISATION OF PEROVSKITE SOLAR CELL STRUCTURE FOR MAXIMUM CURRENT COLLECTION

High conversion efficiencies have recently been demonstrated for perovskite thin film photovoltaic devices. Perovskite thin film solar cells are multilayer opto-electrical structures in which light interference occurs. This phenomenon can be exploited to maximise the light transmission into the absorber material and increase the device efficiency. Fine tuning of layer thicknesses within the stack can be used to control interference at the interfaces. Optical reflection losses can be reduced by achieving destructive interference within the structure of the cell. The light transmission to the perovskite absorber of a thin film solar cell using a fluorine doped tin oxide (FTO) transparent conductor has been modelled using the transfer matrix method. Alternative transparent conductor materials have also been investigated including aluminium doped zinc oxide (AZO) and indium tin oxide (ITO). The model showed that replacing FTO with ITO could increase the photocurrent by as much as 4.5%. This gain can be further increased to 6.5% by using AZO as the TCO material. Fine tuning of the TiO<sub>2</sub> layer thickness can increase the current density by 0.3%. Furthermore, the current density of a Perovskite solar cell can be increased by another 3.5% by application of a multilayer

anti-reflective coating. Optical optimisation of the stack design offers a significant increase in conversion efficiency.

## 8.1 Introduction

Photovoltaic (PV) devices are becoming an attractive energy source even without subsidies. Grid parity has been reached in a number of locations around the world and it is only a matter of time before PV technology will be economically viable globally [126]. The market is currently dominated by crystalline silicon based devices. At the same time new technologies are being developed which can offer additional cost and performance advantages. The most important recent innovation is the discovery of solar cells based on metal-organic perovskite materials [87]. The astonishing rate of increase of device efficiency for these cells has not been observed for any other type of PV device. Long term stability remains an issue for the technology [127]. It is still an immature technology however; it has scope for significant future impact.

Perovskite solar cells in common with all other PV materials suffer from a range of electrical and optical losses. As the optical losses occur prior to exploitation of the photovoltaic effect, it is important to reduce them as much as possible. Optical losses in PV are associated with light reflection and absorption in the solar cell structure [128], [129]. Reflection losses can be eliminated through interference, which is controlled by the layer thickness and the refractive index of materials used. Absorption can only be addressed by thinning the responsible layer or by replacement with a more transparent material.

## 8.2 Experimental details

The perovskite solar cell was modelled as a thin film stack. The structure reported by Ball has been used as the model for this work, and is shown in Figure 8.1 [128]. The cell is deposited on FTO coated glass and comprises layers of  $\text{TiO}_2$  and methyl-ammonium lead iodide perovskite. First, the model was used to investigate interference effects within the model solar cell structure. We then focused on the performance of the Transparent Conductive Oxide (TCO) by investigating the effects of replacing the FTO layer with indium doped tin oxide (ITO) or aluminium doped zinc oxide (AZO) [130]. The modelling was completed by adding a multilayer anti-reflective coating (MAR) on the surface of the cover glass. The calculations were carried out using software based on the transfer matrix method [28]. In all calculations, the transmission into the perovskite

layer was considered. Based on the maximum transmitted light, estimates of the corresponding attainable current have been calculated.

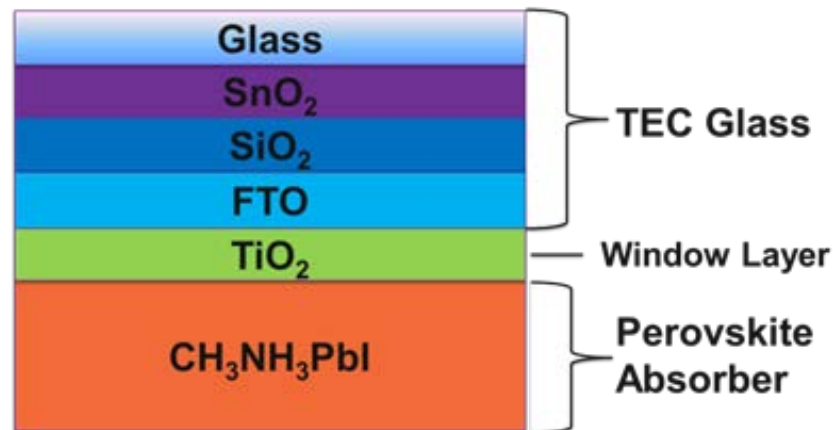


**Figure 8.1: Structure of perovskite solar cell used for optical modelling.**

### 8.3 Results

Figure 8.2 shows the modelled reflection losses at the glass surface and transmission to the absorber layer for the perovskite cell structure shown in Figure 8.1. The average transmission weighted by photon flux in the AM1.5 spectrum to the absorber layer for wavelength between 350nm and 800nm was calculated to be 86.55%.

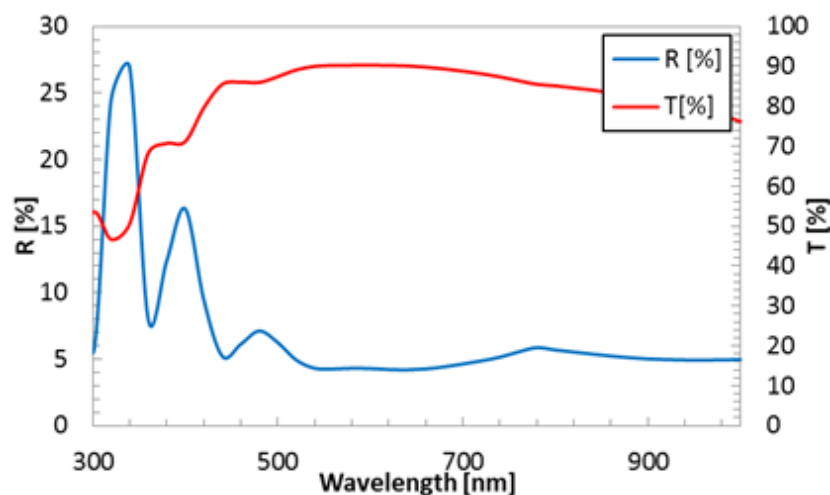


**Figure 8.2: Performance of standard solar cell. Light reflections at the glass surface and the transmission into absorber layer have been modelled.**

#### 8.3.1 TiO<sub>2</sub>

The TiO<sub>2</sub> layer is located between the front contact and the absorber layer. To investigate the effect on transmission to the absorbing layer, the thickness of the TiO<sub>2</sub> layer within the model was varied between 30nm and 70nm; the FTO layer was held at

a thickness of 340nm. Figure 8.3 shows a plot of the transmission as a function of both wavelength and thickness of the TiO<sub>2</sub> layer. The transmission data were then used to calculate the resulting photocurrent density at each thickness of TiO<sub>2</sub>. A plot of current density against TiO<sub>2</sub> is shown in Figure 8.4.

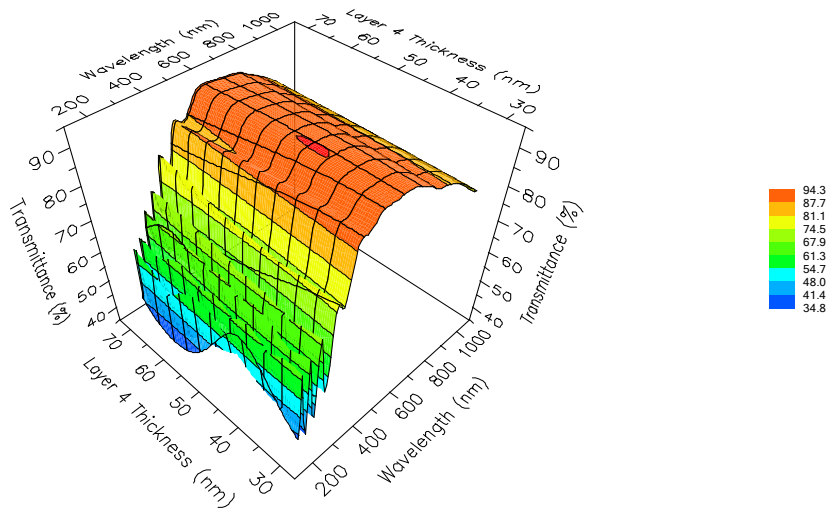


**Figure 8.3:** A 3D plot of transmittance against TiO<sub>2</sub> layer thickness and wavelength.

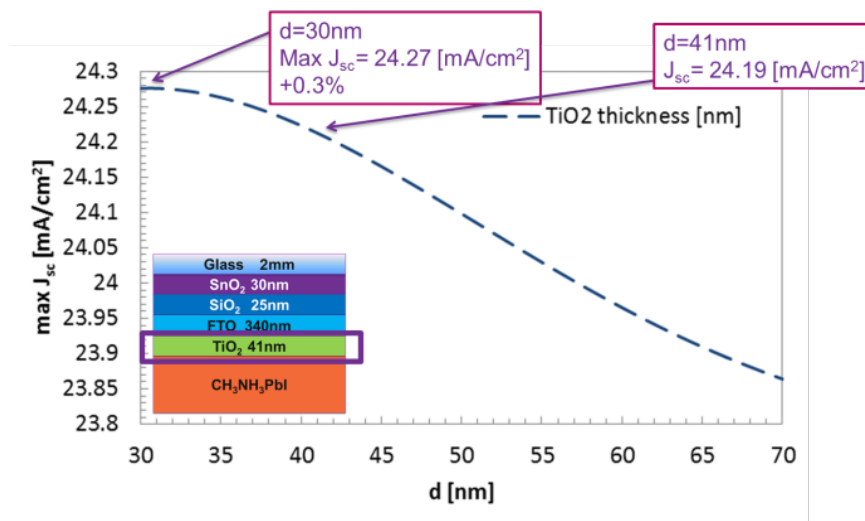


**Figure 8.4:** A graph showing the photocurrent density [mA/cm<sup>2</sup>] dependence on the thickness of the TiO<sub>2</sub> layer [nm].

Figure 8.4 shows that a 41nm thick TiO<sub>2</sub> layer as reported by Ball, has near optimal thickness [128]. It achieves current densities up to 24.19mA/cm<sup>2</sup>. The results show scope for a modest increase of the attainable current density. A 0.3% gain, increasing the limit to 24.27mA.cm<sup>2</sup>, can be obtained if the thickness of the layer is reduced to 30nm.

### 8.3.2 Transparent conductor selection

Transparent conductors play a vital role in any thin film solar cell [131], [132]. The choice is usually dictated by a compromise between the conductivity of the front contact and transparency. Increasing the thickness of the TCO layer improves electrical performance but may reduce the light transmission into the absorber. In this work, the modelled reference cell is built on NSG-Pilkington TEC 15 glass substrate. The refractive index, extinction coefficient and the thickness of the TCO layer can be very important for the photocurrent of the solar cell. Alternative TCO materials have therefore been investigated in order to identify any potential gains over FTO. Two of the most popular TCO materials, ITO and AZO, are examined in this study.

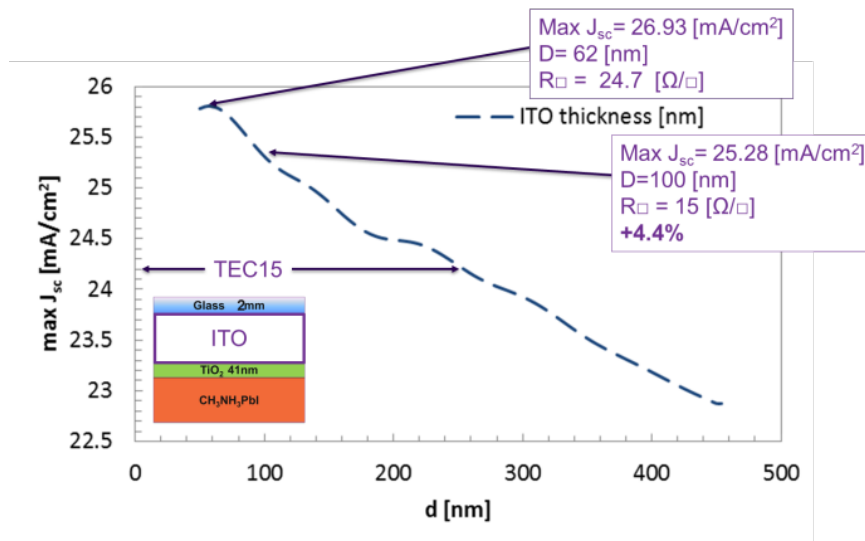
The conductivity of TCO materials is achieved by the introduction of free electrons through doping [133]. This leads to more efficient extraction of current from the device. Unfortunately, the adverse effects of doping include additional absorption and hugely increased reflectivity in some parts of the spectrum. The spectral properties are specific for each TCO material. The refractive index of the TCO depends on the host material and is altered by the dopant [134], [135]. Selecting the material with optimal optical properties can significantly improve light transmission into the absorber layer [136]. Increasing the thickness of the TCO layer improves electrical performance but may have a negative influence on the light transmission into the absorber.

The conductivity of a TCO is material specific, defined by the dopant and the doping concentration. The starting point in TCO modelling was therefore to choose the material thickness that delivers the same  $R_{\square}$  as the reference FTO layer. The required thickness was calculated to be 100nm for ITO ( $\rho=1.5 \cdot 10^{-4}\Omega\text{-cm}$ ) and 233nm for AZO ( $\rho=3.5 \cdot 10^{-4}\Omega\text{-cm}$ ). Both materials required a much thinner layer to achieve same sheet resistance as FTO. The refractive index matching structures, which are used in TEC15 glass, were not included in AZO and ITO models.

### 8.3.3 ITO

ITO is a very commonly used transparent conductor in both PV devices and consumer electronics applications [137]. It is a highly conductive material and hence at  $15\Omega/\square$  (100nm) it is thinner than AZO and FTO. To investigate the effect of varying the ITO layer thickness, the thickness of the  $\text{TiO}_2$  layer was held constant at 41nm. The thickness of the ITO layer was varied between 50nm ( $30 \Omega/\square$ ) and 450nm ( $3 \Omega/\square$ ), and

the photocurrent density was calculated from the resulting transmission data. Current density was plotted against the thickness of the ITO layer (Figure 8.5).



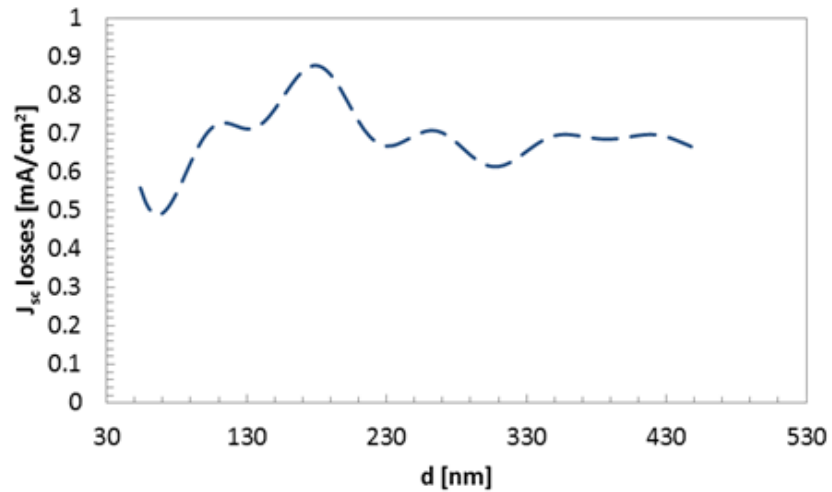
**Figure 8.5: Dependence of the photocurrent density [mA/cm<sup>2</sup>] on the thickness of the ITO layer [nm].**

Figure 8.5 shows that the transmission into the absorber layer decreases with increased ITO thickness. The loss is a result of increased absorption losses. The maximum transmission was found at a thickness of 62nm; this gave a photocurrent density of 26.93mA/cm<sup>2</sup>. At 100nm (corresponding to the reference 15  $\Omega/\square$ ) replacing FTO with ITO results in a 1.17mA/cm<sup>2</sup> (4.5%) increase in current density.

Though the effect of increasing the ITO layer thickness results in a lower photocurrent density the rate at which the current decreases is not constant due to interference effects.

Figure 8.6 shows the modelled current density loss based on the reflection from the ITO back to the cover glass. Using interference enables the thickness of ITO to be increased without optical losses. In a solar cell this reduces electrical losses without affecting the optical properties of the stack.

The optical performance of ITO in perovskite solar cells is driven by absorption which dominates the characteristics. Interference can however be used to reduce the losses. Thickness variation between 175nm and 200nm has little effect on the light transmission into the cell. In this thickness range the interference compensates for the absorption losses. This allows a reduction in TCO sheet resistance from 10 $\Omega/\square$  to 7.5 $\Omega/\square$  with no corresponding increase in optical losses. For ITO thickness between 140nm and 175nm increased reflection and absorption losses result in a reduction of current density.



**Figure 8.6: Reflection losses as function of ITO thickness.**

### 8.3.4 AZO

AZO is a transparent conducting oxide which has received increasing interest in recent years [130]. The model was altered to incorporate a layer of AZO as the TCO to compare the optical and electrical qualities of the materials. Figure 8.7 shows a 3D plot of the transmission as function of light wavelength in range from 200nm to 1000nm and thicknesses of AZO between 50nm and 500nm. The data presented in Figure 8.7 were used to calculate the resulting photocurrent in the perovskite solar cell. A plot of photocurrent against AZO thickness can be seen in Figure 8.8.

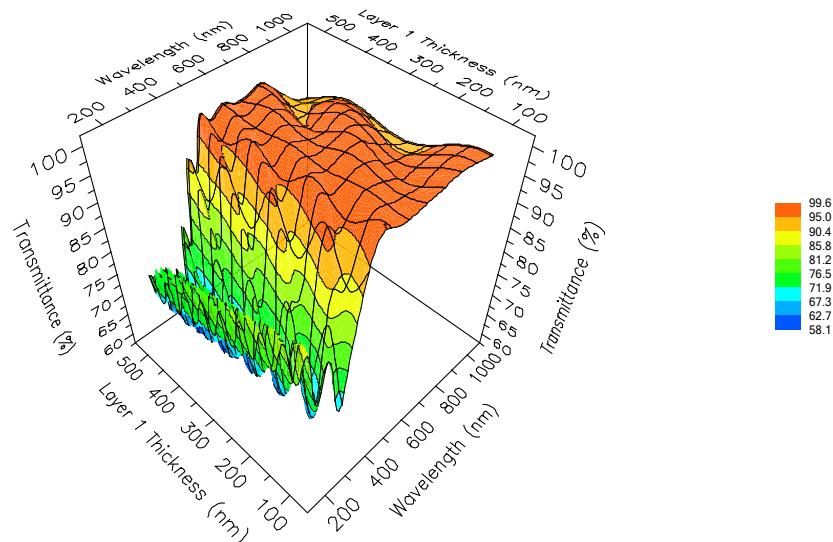


**Figure 8.7: A 3D plot of transmittance against AZO layer thickness and wavelength.**

Figure 8.8 shows photocurrent as a function of AZO layer thickness. For AZO a sheet resistance of  $15 \Omega/\square$  is achieved at 232nm; at this thickness the current density is  $1.58\text{mA}/\text{cm}^2$  higher than in the FTO based cell. The maximum is achieved for a 244nm thick AZO layer. This gives both a small increase in photocurrent and a minor reduction in sheet resistance to  $14.3\Omega/\square$ . AZO has the lowest optical losses amongst the commonly considered TCO materials. Current losses due to absorption and reflection for different AZO thicknesses are plotted in Figure 8.9. The analysis shows that AZO has larger interference effects within the perovskite stack than ITO. Compared to FTO the use of AZO resulted in a 6.5% increase in current density.

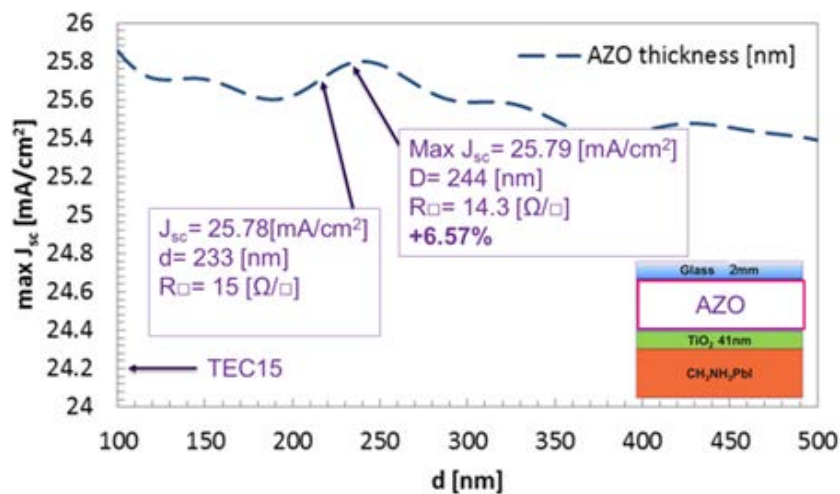


**Figure 8.8:** A graph showing the photocurrent [ $\text{mA}/\text{cm}^2$ ] dependence on the thickness of the AZO layer [nm].

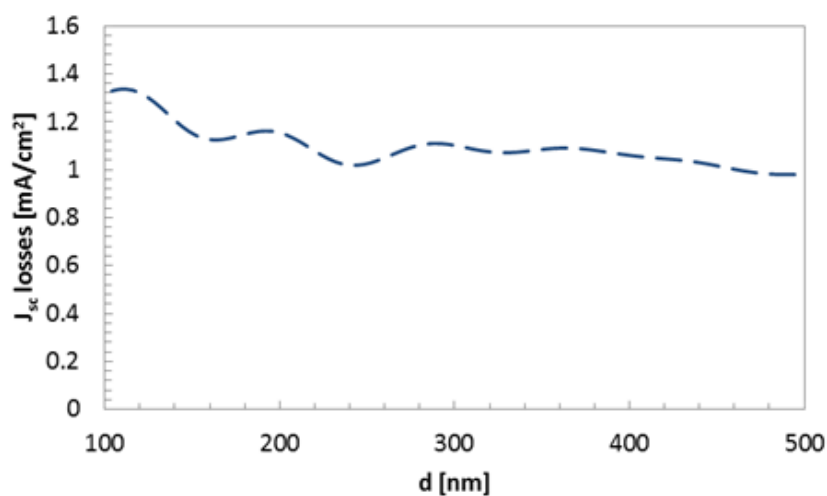


**Figure 8.9:** Reflection losses modelled for perovskite solar cells as a function of AZO thickness.

Figure 8.10 shows comparisons between the FTO and AZO T% and R% characteristics. AZO offers higher transmission despite higher reflection losses in some region of the spectrum.

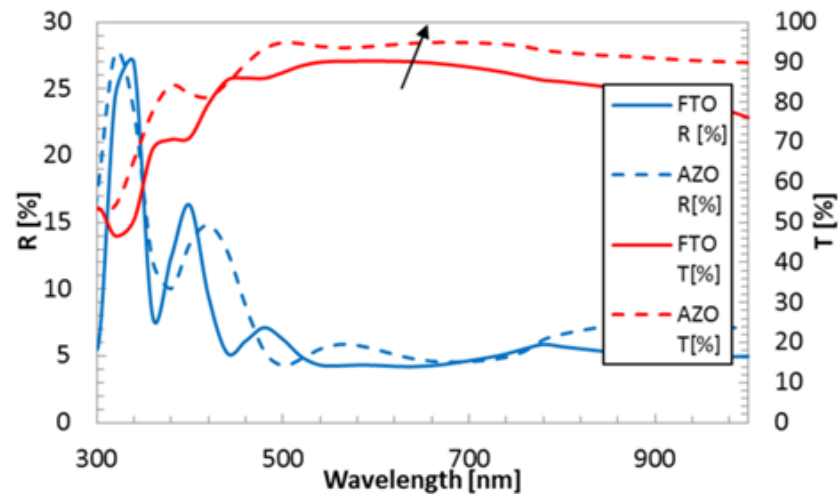


**Figure 8.10: Optical properties of perovskite solar cells using AZO (dotted lines) and FTO (solid lines) as TCO.**

#### 8.4 Multi-Layer AR

Figure 8.11 shows reflection modelled for uncoated glass and values recorded for multi-layer antireflective (MAR) coated glass. The design details of the MAR coating can be found in chapter 5 [83]. Applying an MAR coating to perovskite solar cells could achieve an additional 3.5% gain in power from the cell.

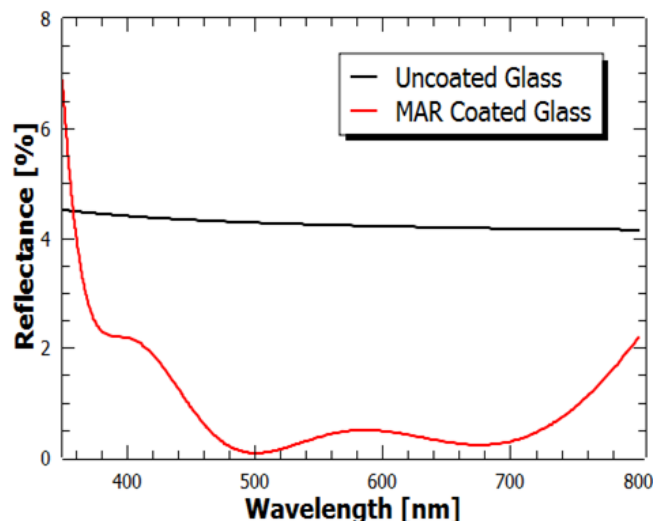


**Figure 8.11: Reflection spectra of MAR-coated glass designed for perovskite solar cells.**

## 8.5 Summary

The optical performance of perovskite solar cells has been modelled. Altering the layer thicknesses within the perovskite solar cell showed that modest gains can be achieved by reducing the  $\text{TiO}_2$  layer thickness to 32nm. This would increase photocurrent by 0.3%.

The influence of the TCO has been investigated. TEC15 was used as the reference, and the maximum performance was compared to that for cells using different thicknesses of ITO and AZO as the TCO layer. The optical properties of these alternative materials enable increases in photocurrent. The calculated gains were 4.5% for ITO and 6.5% for AZO.

For AZO it was possible to increase the TCO thickness to reduce resistance losses without any corresponding reduction in the transmission. This offered relatively small optical gains, but because of the reduced sheet resistance could be industrially significant. During the thin film PV manufacturing process the PV material is divided into cells which are interconnected in series to avoid resistance losses and ensure efficient generation [138]. The pitch used during the solar cell formation defines the number of interconnects required per  $\text{m}^2$  of module. The interconnects are required to avoid resistance losses but introduce dead areas into the module. The choice of pitch used for interconnect formation is a compromise between resistance and optical losses. With high quality PV devices the resistive losses should mainly rely on the TCO properties. Thus TCOs with higher conductivity could enable reduced losses at the interconnect level.

The above benefits can be further improved by application of an anti-reflective coating, which can provide additional 3.5% gains. This is in addition to the 6.8% gain possible with replacing the FTO with AZO and using thinner  $\text{TiO}_2$ . Combining AZO with MAR coatings and thinner  $\text{TiO}_2$  could increase the photocurrent of the cell by up to 10.3%.

# 9 CONCLUSIONS AND FUTURE WORK

Anti-reflection coatings (ARCs) have a wide range of applications. The possible increase in transmission through the glass superstrate or cover glass of solar technologies, through the reduction of reflection at the air glass interface, is significant. The application of ARCs to solar panels has been shown to increase energy output. ARCs would therefore increase the impact of solar installations in combating global climate change by reducing the cost per watt. The financial case for investment in ARCs is therefore compelling. However, achieving durable, low cost and efficient anti-reflection solutions has proved challenging. The ideal AR solution for each circumstance is unique, as each PV technology and environment brings different technical demands. ARCs have proven effective in reducing reflectance, however further research can be done on optimising interference based coatings in different environments, such as in space or at the equator. MAR can be effectively optimised on an installation by installation basis; however the benefits from only small differences in installation environment would be minimal. Single layer coatings are a less complicated and often cheaper alternative but less effective than MAR coatings at reflection reduction. In this work, a selection of novel ARCs are designed and compared to an ARC currently used in the solar industry.

Zirconia/silica MAR coatings developed at Loughborough University were optically optimised to maximise transmission through the air-glass interface. Designs were created for a variety of solar cell technologies including, CdTe, Perovskite, a-Si, and

CIGS. These designs were then deposited onto glass substrates and the WAT of the samples was measured. To further prove the effectiveness of MARs, samples were used in conjunction with CdTe cells produced at Colorado State University. The coating was compared to alternative ARCs produced through sol-gel deposition methods. The WAT of sol-gel coatings developed at TWI Ltd and the commercially available AR1 from Prinz Optic were compared across the usable wavelength ranges of the technologies. This allowed for a direct comparison between all three types of ARC. In addition to the deposited zirconia/silica coatings, alternative high refractive index materials to zirconia were modelled to compare their performance theoretically. The most effective MARs used zirconia according to modelled transmission of optimised MAR designs, despite the relatively low refractive index of zirconia. This is explained by the shape of the dispersion relationship of the candidate high index materials.

ARCs used on solar installations will need to endure weathering and mechanical damage over a period of decades. MARs and AR1 samples underwent several experiments, in accordance with industry standards, to determine the durability of the coatings. MAR coatings were found to be more durable than or just as durable as AR1 samples. MAR coatings also proved suitable for use on solar installations, as the longevity of the coatings is likely greater than 25 years. Additionally the hydrophobicity of the coatings was measured using the water contact angle. A high contact angle correlates with low surface energy. A hydrophobic surface is less likely to adhere to soiling and should also ease the task of cleaning. In this regard MARs are considerably more hydrophobic than the AR1 (35° contact angle compared to 9°), however greater hydrophobicity would be desirable in an ARC. In future it would be interesting to research the optical and mechanical effects of the application of hydrophobic coatings in conjunction with MARs and ARCs in general. These results could then be compared and contrasted with competing anti-reflection solutions in terms of cost, friability, susceptibility to weathering damage, and effectiveness. All things considered silica-zirconia MAR coatings appear to be damage resistant and durable to all forms of weathering damage, passing all industry standards for solar cells and optical coatings.

In addition to the reflection at the air-glass interface, thin film solar cell technologies experience optical losses from material absorption and reflected light at media boundaries within the solar stack. The implementation of electronically sound designs, that take advantage of optical interference within the solar stack, has been shown to improve transmission to the absorbing layer. The ground work for the optical

optimisation of CdTe and perovskite solar cells has been developed. The optimisation of the transparent conducting oxide layer in CdTe solar cells and internal anti-reflection layers may be suitable for crystalline silicon solar cells. A summary of the findings of this work is shown in Table 9.1.

**Table 9.1: Summary of candidate ARCs. The coatings are compared on anti-reflective performance, durability, hydrophobicity, and deposition expense.**

	Uncoated soda-Lime Glass	TWI Sol-Gel Coating	Commercial Sol-Gel hard coat, AR1	Silica and Zirconia Multilayer ARC
Cost	N/A	Very cheap	Cheap	Moderate cost
Transmittance	91.6%	96.4%	94.6%	97.4%
Reflectance	8.4%	3.6%	2.0%	2.6%
Deposition Method	N/A	Dip coating	An established Sol-Gel deposition method	Reactive magnetron sputtering
Adhesion	N/A	Poor	Very good	Excellent
Contact angle	11°	100° (111° with HMDS)	9°	35°

The thickness and material of the buffer layer in CdTe devices was shown to be influential over the transmission of light to the absorbing layer. ZnO and TiO<sub>2</sub> buffer layer were compared and contrasted with one another. ZnO gave greater transmission to the absorber at all modelled thicknesses. ZnO was also thicker at maximum transmission, with a thickness of 58nm compared to the thickness of TiO<sub>2</sub> at 48nm. The maximum transmission to the absorber when using ZnO as a buffer layer was 78.5%, for TiO<sub>2</sub> the maximum transmission was 78.0%. The results suggest that ZnO benefits from having more pronounced interference effects and lower absorption. The more pronounced interference effect allows for a thicker buffer layer compared to layers of TiO<sub>2</sub>, which is electronically desirable to reduce the risk of shorting.

Modelling the perovskite stack showed a small improvement to transmission can be made by optimizing the thickness of the TiO<sub>2</sub> layer. Alternative TCO materials showed significant increases in photocurrent when thickness is optically optimised. The

calculated photocurrent using the candidate materials in perovskite stack resulted in photocurrent increases of 4.5% for ITO and 6.5% for AZO. Coupled with a MAR coating this gave a maximum photocurrent increase of 10% for optimised perovskite devices.

Looking forward the author would like to point out some possible research opportunities. The development of an ARC that transmits visible light, but blocks infrared, would allow for solar installations to remain cooler in hot weather. Additionally, MARs designed to maximise transmission through crystalline silicon cover glass are an interesting prospect. Finally, MARs designed for use in the AM0 solar spectrum, for use on space installations, may prove to be a light weight and therefore viable choice for extra-terrestrial solar installations.

# 10 REFERENCES

- [1] D. J. C. Mackay, *Sustainable Energy — without the hot air*. Cambridge, UK: UIT Cambridge Ltd, 2009.
- [2] BP, “BP Statistical Review of World Energy,” no. June, 2016.
- [3] T. Stocker, D. Qin, G.-K. Plattner, M. M. B. Tignor, S. K. Allen, J. Boschung, A. Nauels, Y. Xia, V. Bex, and P. M. Midgley, “IPCC 2013: Climate Change 2013 : The Physical Science Basis.” Cambridge University Press, Cambridge, UK and New York, USA, 2014.
- [4] L. Dusonchet and E. Telaretti, “Comparative economic analysis of support policies for solar PV in the most representative EU countries,” *Renew. Sustain. Energy Rev.*, vol. 42, pp. 986–998, 2015.
- [5] A. Luque and S. Hegedus, *Handbook of Photovoltaic Science*. 2003.
- [6] M. Grätzel, “Photoelectrochemical cells,” vol. 414, no. November, 2001.
- [7] C. G. Granqvist, “Transparent conductors as solar energy materials: a panoramic review,” *Sol. Energy Mater. Sol. Cells*, vol. 91, no. October, pp. 1529–1598, 2007.
- [8] J. Lorente, A. Redaño, and X. De Cabo, “Influence of urban aerosol on spectral solar irradiance,” *J. Appl. Meteorol.*, vol. 33, pp. 406–415, 1994.
- [9] C. Riordan and R. Hulstron, “What is an air mass 1.5 spectrum?,” in *Conference Record of the Twenty First IEEE Photovoltaic Specialists Conference*, 1990, pp. 1085–1088.
- [10] D. R. Myers, K. Emery, and C. Gueymard, “Revising and Validating Spectral Irradiance Reference Standards for Photovoltaic Performance Evaluation,” *J. Sol. Energy Eng.*, vol. 126, no. 1, p. 567, 2004.

- [11] J. Nelson, *The Physics of solar cells*. London: Imperial College Press, 2003.
- [12] J. P. Colinge and C. A. Colinge, *Physics of semiconductor devices*. New York Boston, Dordrecht, London, Moscow: Kluwer Academic Publishers, 2002.
- [13] C. Kittel, *Introduction to Solid State Physics*, 8th ed. New York: John Wiley & Sons, 1995.
- [14] L. L. Kazmerski, “Solar photovoltaics R&D at the tipping point: A 2005 technology overview,” *J. Electron Spectros. Relat. Phenomena*, vol. 150, no. 2, pp. 105–135, 2006.
- [15] B. Burger, K. Kiefer, C. Kost, S. Nold, S. Philipps, R. Preu, J. Rentsch, T. Schlegl, G. Stryi-Hipp, G. Willeke, H. Wirth, I. Brucker, A. Häberle, and W. Warmuth, “Photovoltaics Report,” 2015.
- [16] M. A. Green, *Silicon Solar Cells: Advanced Principles & Practice*. Center for Photovoltaic Devices and Systems, 1995.
- [17] M. A. Green, K. Emery, Y. Hishikawa, W. Warta, E. D. Dunlop, D. H. Levi, and A. W. Y. Ho-Baillie, “Solar cell efficiency tables (version 49),” *Prog. Photovolt Res. Appl.*, vol. 25, no. 1, pp. 3–13, 2017.
- [18] T. Tiedje, E. Yablonovitch, G. D. Cody, and B. G. Brooks, “Limiting efficiency of silicon solar cells,” *IEEE Trans. Electron Devices*, vol. 31, no. 5, pp. 711–716, 1984.
- [19] Energy Trend, “Price Quotes,” <http://pv.energytrend.com/pricequotes.html>, 2016. .
- [20] M. A. Green, K. Emery, Y. Hishikawa, W. Warta, and E. D. Dunlop, “Solar cell efficiency tables (version 48),” *Prog. Photovolt Res. Appl.*, vol. 24, pp. 905–913, 2016.
- [21] First Solar, “2016 Fact Sheet,” 2016.
- [22] D. . Bätzner, A. Romeo, H. Zogg, R. Wendt, and A. . Tiwari, “Development of efficient and stable back contacts on CdTe/CdS solar cells,” *Thin Solid Films*, vol. 387, no. 1, pp. 151–154, 2001.
- [23] G. R. Fowles, *Introduction to Modern Optics*, vol. 8. New York: Publications, Dover, 1989.
- [24] L. A. A. Pettersson, L. S. Roman, and O. Inganäs, “Modeling photocurrent action spectra of photovoltaic devices based on organic thin films Modeling photocurrent action spectra of photovoltaic devices based on organic thin films,” *J. Appl. Phys.*, vol. 487, no. 1999, pp. 487–496, 2011.
- [25] Z. Knittl, *Optics Of Thin Films*. John Wiley & Sons Ltd, 1976.
- [26] O. S. Heavens, *Optical properties of thin solid films*. 1991.

- [27] P. Peumans, A. Yakimov, and S. R. Forrest, "Small molecular weight organic thin-film photodetectors and solar cells," *J. Appl. Phys.*, vol. 93, no. 7, pp. 3693–3723, 2003.
- [28] A. Macleod and C. Clark, "Optical Coating Design with the Essential Macleod." Thin Film Center Inc., Tucson, 2012.
- [29] A. E. Conrady, *Applied Optics and Optical Design Part One*. Oxford UK: Oxford University Press, 1929.
- [30] M. Françon, *Optical Interferometry*. New York, London: Academic Press, 1966.
- [31] S. Woo, S. Kim, and C. K. Hwangbo, "Optical and Structural Properties of TiO<sub>2</sub> and MgF<sub>2</sub> Thin Films by Plasma Ion-Assisted Deposition," *J. Korean Phys. Soc.*, vol. 45, no. 1, 2004.
- [32] C. Tao, H. Yan, X. Yuan, Q. Yin, J. Zhu, W. Ni, L. Yan, and L. Zhang, "Sol-gel based antireflective coatings with superhydrophobicity and exceptionally low refractive indices built from trimethylsilylated hollow silica nanoparticles," *Colloids Surfaces A Physicochem. Eng. Asp.*, vol. 509, pp. 307–313, 2016.
- [33] B. Fabes, B. J. J. Zelinski, and D. R. Uhlmann, "Sol-Gel Derived Ceramic Coatings," in *Ceramic Films and Coatings*, J. B. Wachtman and R. A. Haber, Eds. Park Ridge: Noyes, 1993, pp. 224–284.
- [34] F. Mammeri, B. Le Eric, L. Rozes, and C. Sanchez, "Mechanical properties of hybrid organic-inorganic materials.," *J. Mater. Chem.*, vol. 15, no. 35–36, pp. 3787–3811, 2005.
- [35] Z. Guo, T. Pereira, O. Choi, Y. Wang, and H. T. Hahn, "Surface functionalized alumina nanoparticle filled polymeric nanocomposites with enhanced mechanical properties," *J. Mater. Chem.*, vol. 16, no. 27, p. 2800, 2006.
- [36] M. Pagliaro, R. Ciriminna, and G. Palmisano, "Silica-based hybrid coatings," *J. Mater. Chem.*, vol. 19, no. 20, p. 3116, 2009.
- [37] C. J. Brinker and G. W. Scherer, *Sol-Gel Science*. New York: Academic Press, 1990.
- [38] D. Ristau, S. Günster, S. Bosch, A. Duparré, E. Masetti, J. Ferré-Borrull, G. Kiriakidis, F. Peiró, E. Quesnel, and A. Tikhonravov, "Ultraviolet optical and microstructural properties of MgF<sub>2</sub> and LaF<sub>3</sub> coatings deposited by ion-beam sputtering and boat and electron-beam evaporation.," *Appl. Opt.*, vol. 41, no. 16, pp. 3196–3204, 2002.
- [39] P. M. Kaminski, F. Lisco, and J. M. Walls, "Multilayer Broadband Antireflective Coatings for More Efficient Thin Film CdTe Solar Cells," *IEEE J. Photovoltaics*, vol. 4, no. 1, pp. 452–456, Jan. 2014.
- [40] A. Deinega, I. Valuev, B. Potapkin, and Y. Lozovik, "Minimizing light reflection from dielectric textured surfaces," *J. Opt. Soc. Am. A*, vol. 28, no. 5, p. 770, 2011.

- [41] D. H. Raguin and G. M. Morris, "Analysis of antireflection-structured surfaces with continuous one-dimensional surface profiles.," *Appl. Opt.*, vol. 32, no. 14, pp. 2582–2598, 1993.
- [42] B. L. Sopori and R. a. Pryor, "Design of antireflection coatings for textured silicon solar cells," *Sol. Cells*, vol. 8, no. 3, pp. 249–261, 1983.
- [43] R. Prado, G. Beobide, A. Marcaide, J. Goikoetxea, and A. Aranzabe, "Development of multifunctional sol-gel coatings: Anti-reflection coatings with enhanced self-cleaning capacity," *Sol. Energy Mater. Sol. Cells*, vol. 94, no. 6, pp. 1081–1088, 2010.
- [44] X. Li, J. He, and W. Liu, "Broadband anti-reflective and water-repellent coatings on glass substrates for self-cleaning photovoltaic cells," *Mater. Res. Bull.*, vol. 48, no. 7, pp. 2522–2528, 2013.
- [45] K. Askar, B. M. Phillips, Y. Fang, B. Choi, N. Gozubenli, P. Jiang, and B. Jiang, "Self-assembled self-cleaning broadband anti-reflection coatings," *Colloids Surfaces A Physicochem. Eng. Asp.*, vol. 439, pp. 84–100, 2013.
- [46] R. Gordon, "Chemical vapor Deposition of Coatings on glass," *J. Non. Cryst. Solids*, vol. 218, pp. 81–91, 1997.
- [47] K. L. Chopra, P. D. Paulson, and V. Dutta, "Thin-film solar cells: an overview," *Prog. photovoltaics*, vol. 12, no. 23, pp. 69–92, 2004.
- [48] N. Re-, R. M. May, J. J. Dooley, M. G. Morgan, a K. N. Reddy, R. H. Williams, E. a Parson, D. W. Keith, R. T. Watson, M. C. Zinyowera, D. J. Dokken, a P. Kinzig, D. M. Kammen, R. E. Evenson, P. E. Waggoner, V. W. Ruttan, M. I. Nadiri, R. G. Noll, D. M. Kammen, D. Re-, and P. Alto, "Photovoltaic Technology : The Case for Thin-Film Solar Cells," vol. 285, no. July 1999, 2000.
- [49] O. a. Fouad, a. a. Ismail, Z. I. Zaki, and R. M. Mohamed, "Zinc oxide thin films prepared by thermal evaporation deposition and its photocatalytic activity," *Appl. Catal. B Environ.*, vol. 62, no. 1–2, pp. 144–149, 2006.
- [50] A. D. Compaan, A. Gupta, J. Drayton, S.-H. Lee, and S. Wang, "14% sputtered thin-film solar cells based on CdTe," *Phys. Status Solidi*, vol. 241, no. 3, pp. 779–782, Mar. 2004.
- [51] D. Bhattacharyya, N. K. Sahoo, S. Thakur, and N. C. Das, "Spectroscopic ellipsometry of TiO<sub>2</sub> layers prepared by ion-assisted electron-beam evaporation," *Thin Solid Films*, vol. 360, no. 1–2, pp. 96–102, 2000.
- [52] M. Castro, R. Cuerno, L. V??zquez, and R. Gago, "Self-organized ordering of nanostructures produced by ion-beam sputtering," *Phys. Rev. Lett.*, vol. 94, no. 1, pp. 1–4, 2005.
- [53] V. V Plotnikov, C. W. Carter, J. M. Stayancho, N. R. Paudel, H. Mahabaduge, D. Kwon, C. R. Grice, and A. D. Compaan, "Semitransparent PV Windows with

- Sputtered CdS / CdTe Thin Films,” in *proceedings of 39th IEEE PVSC*, 2013, pp. 0405–0408.
- [54] J. P. Enríquez and X. Mathew, “XRD study of the grain growth in CdTe films annealed at different temperatures,” *Sol. Energy Mater. Sol. Cells*, vol. 81, pp. 363–369, 2004.
- [55] P. J. Kelly and R. D. Arnell, “Magnetron sputtering: a review of recent developments and applications,” *Vacuum*, vol. 56, no. 3, pp. 159–172, 2000.
- [56] J. W. Seeser, P. M. LeFebvre, B. P. Hichwa, J. P. Lehan, S. F. Rowlands, and T. H. Allen, “Meta-Mode’ Reactive Sputtering: A new way to make thin film products,” in *Society of Vacuum Coaters, 35th Annual Technical Conference Proceedings*, 1992, pp. 229–235.
- [57] S. Horita, T. Tajima, M. Murakawa, T. Fujiyama, and T. Hata, “Improvement of the crystalline quality of an yttria-stabilized zirconia film on silicon by a new deposition process in reactive sputtering,” *Thin Solid Films*, vol. 229, no. 1, pp. 17–23, 1993.
- [58] B. D. Farbes, B. J. J. Zelinski, and D. R. Uhlman, *Sol-Gel Derived ceramic coatings*. Westwood, NJ, USA: Noyes Publications, 1993.
- [59] F. Mammeri, E. Le Bourhis, L. Rozes, and C. Sanchez, “Mechanical properties of hybrid organic-inorganic materials,” *J. Mater. Chem.*, vol. 15, no. 35–36, pp. 3787–3811, 2005.
- [60] T. Wada, Y. Sato, K. Suzuki, H. Aono, D.-G. Chen, A. Y. Yan, Y. Ono, and M. Takamatsu, “Anti-Reflection (AR) Coating Meter,” in *SAE Technical Paper*, 1999, pp. 1999–01–0897.
- [61] A. Wakabayashi, M. Nakao, H. Horikoshi, T. Neyu, T. Tsuchiya, M. Okumura, and Y. Iwasak, “Poster 1-67,” in *International Workshop on Glass, Ceramics, Hybrids and Nanocomposites from Gels*, 1999, pp. 19–24.
- [62] T. Oishi, T. Ishikawa, and D. Kamoto, “Poster 2-28,” in *10th International Workshop on Glass, Ceramics, Hybrids and Nanocomposites from Gels*, 1999, pp. 19–24.
- [63] D. Chen, “Anti-reflection (AR) coatings made by sol-gel processes: A review,” *Sol. Energy Mater. Sol. Cells*, vol. 68, no. 3–4, pp. 313–336, 2001.
- [64] I. Strawbridge and P. F. James, “Thin silica films prepared by dip coating,” *J. Non. Cryst. Solids*, vol. 82, no. 1–3, pp. 366–372, 1986.
- [65] D. Meyerhofer, “Characteristics of resist films produced by spinning,” *J. Appl. Phys.*, vol. 49, no. 7, pp. 3993–3997, 1978.
- [66] J. A. BRITTEN, “a Simple Theory for the Entrained Film Thickness During Meniscus Coating,” *Chem. Eng. Commun.*, vol. 120, no. 1, pp. 59–71, 1993.

- [67] D. R. Lide, *Handbook of Chemistry and Physics*, 87th ed. Boca Raton, FL: CRC Press, 1998.
- [68] E. V. Astrova and V. a. Tolmachev, "Effective refractive index and composition of oxidized porous silicon films," *Mater. Sci. Eng. B Solid-State Mater. Adv. Technol.*, vol. 69, pp. 142–148, 2000.
- [69] H. R. Moulten, "Method of producing thin microporous silica coatings having reflection reducing characteristics and the articles so coated," US 2474061 A, 1949.
- [70] W. Glaubitt and P. Löbmann, "Antireflective coatings prepared by sol-gel processing: Principles and applications," *J. Eur. Ceram. Soc.*, vol. 32, no. 11, pp. 2995–2999, 2012.
- [71] J. C. Thies, E. Currie, and G. J. W. Meijers, "Preparation of a mechanically durable single layer coating with anti-reflective properties," US 7655298 B2, 2010.
- [72] P. Buskens, N. Arfsten, R. Habets, H. Langermans, A. Overbeek, J. Scheerder, J. Thies, and N. Viets, "Innovation at DSM: State of the Art Single Layer Anti-Reflective Coatings for Solar Cell Cover," *Glas. Perform. Days 2009*, pp. 505–507, 2009.
- [73] P. K. Biswas, D. Kundu, and D. Ganguli, "A sol-gel-derived antireflective coating on optical glass for near-infrared applications," *J. Mater. Sci. Lett.*, vol. 8, no. 12, pp. 1436–1437, 1989.
- [74] AZoM, "Silica - Silicon Dioxide (SiO<sub>2</sub>)," 2001.
- [75] J. F. Shackelford, Y.-H. Han, S. Kim, and S.-H. Kwon, *CRC Materials Science and Engineering Handbook 4th Edition*. 2015.
- [76] AZoM, "Zirconia - ZrO<sub>2</sub>, Zirconium Dioxide," 2001.
- [77] P. Dahl, I. Kaus, Z. Zhao, M. Johnsson, M. Nygren, K. Wiik, T. Grande, and M. A. Einarsrud, "Densification and properties of zirconia prepared by three different sintering techniques," *Ceram. Int.*, vol. 33, no. 8, pp. 1603–1610, 2007.
- [78] E. P. Meagher and G. A. Lager, "Polyhedral thermal expansion in the TiO<sub>2</sub> polymorphs: refinement of the crystal structures of rutile and brookite at high temperature," *Can. Mineral.*, vol. 17, pp. 77–85, 1979.
- [79] A. R. Oganov and A. O. Lyakhov, "Towards the Theory of Hardness of Materials," *J. Superhard Mater.*, vol. 32, no. 3, pp. 143–147, 2010.
- [80] W. Martienssen and H. Warlimont, *Springer Handbook of condensed Matter and Materials Data*, vol. 1. 2005.
- [81] H. O. Pierson, *Handbook of Chemical Vapor Deposition: Principles, Technology and Applications*. 1992.

- [82] Y. W. Bae, W. Y. Lee, and D. P. Stinton, "Effects of Temperature and Reagent Concentration on the Morphology of Chemically Vapor Deposited  $\beta$ -Ta<sub>2</sub>O<sub>5</sub>," *J. Am. Ceram. Soc.*, vol. 78, no. 5, pp. 1287–1300, 1995.
- [83] P. M. Kaminski, G. Womack, and J. M. Walls, "Broadband Anti-Reflection coatings for Thin Film Photovoltaics," no. 1.
- [84] S. Schiller, U. Heisig, and K. Goedicke, "Alternating ion plating---A method of high-rate ion vapor deposition," *J. Vac. Sci. Technol.*, vol. 12, no. 4, pp. 858–864, 1975.
- [85] J. M. Walls, "Optical Coatings for ophthalmic lenses by reactive magnetron sputtering," *Technical Digest "Optical Interference Coatings 2001" (Optical Society of America, Washington)*, pp. ThD1–1, 2001.
- [86] W. Sampath, S. Kohli, R. A. Enzenorth, K. Barth, V. Manivannan, J. Hilfiker, P. R. McCurdy, K. Barricklow, and P. Noronha, "Advances in continuous, in-line processing of stable CdS/CdTe devices," in *proceedings of IEEE 33rd PVSC*, 2008, pp. 1–4.
- [87] M. Liu, M. B. Johnston, and H. J. Snaith, "Efficient planar heterojunction perovskite solar cells by vapour deposition.," *Nature*, vol. 501, no. 7467, pp. 395–8, Sep. 2013.
- [88] W. Kern, "Cleaning solutions based on hydrogen peroxide for use in silicon semiconductor technology," *RCA Rev.*, vol. 31, pp. 187–206, 1970.
- [89] M. A. Green, K. Emery, Y. Hishikawa, W. Warta, and E. D. Dunlop, "Solar cell efficiency tables ( version 42 )," *Prog. Photovoltaics Res. Applications*, vol. 21, pp. 827–837, 2013.
- [90] C. H. Chen, S. Y. Li, A. S. T. Chiang, A. T. Wu, and Y. S. Sun, "Scratch-resistant zeolite anti-reflective coating on glass for solar applications," *Sol. Energy Mater. Sol. Cells*, vol. 95, no. 7, pp. 1694–1700, 2011.
- [91] G. Womack, P. M. Kaminski, and J. M. Walls, "High temperature stability of broadband Anti-Reflection coatings on soda lime glass for solar modules," *2015 IEEE 42nd Photovolt. Spec. Conf. PVSC 2015*, pp. 1–3, 2015.
- [92] C. R. Osterwald and T. J. McMahon, "History of Accelerated and Qualification Testing of Terrestrial Photovoltaic Modules: A Literature Review," *Prog. Photovolt Res. Appl.*, vol. 17, pp. 11–33, 2008.
- [93] "Optics and photonics - Optical coatings, Part 4: Specific test methods," *ISO 9211-4*. 2012.
- [94] L. Yan, N. Liu, S. Zhao, H. Yan, H. Lü, and X. Yuan, "Effect of hydrophobic modification on the durability and environmental properties of porous MgF<sub>2</sub> antireflective films," *Acta Metall. Sin. (English Lett.)*, vol. 27, no. 4, pp. 649–655, 2014.

- [95] “Paints and varnishes -- Pull-off test for adhesion,” *ISO 4624*. 2002.
- [96] “Standard Test Method for Pull-Off Strength of Coatings Using Portable Adhesion Testers,” *ASTM D4541*. 2002.
- [97] “Glass in building. Coated glass. Requirements and test methods for class A, B and S coatings,” *Bs En 1096-2:2012*. 2002.
- [98] “Standard Test Method for Accelerated Acid Etch Weathering of Automotive Clearcoats Using a Xenon-Arc Exposure Device,” *ASTM D7356/D735*. 2006.
- [99] “Standard Test Method for Resistance of Transparent Plastics to Surface Abrasion,” *ASTM D1044-13*. 2013.
- [100] R. H. Kim, H. J. Kim, I. Bae, S. K. . Hwang, D. B. Velusamy, S. M. Cho, K. Takaishi, T. Muto, D. Hashizume, M. Uchiyama, P. André, F. Mathevet, B. Heinrich, T. Aoyama, D. Kim, H. Lee, J. Ribierre, and C. Park, “Non-volatile organic memory with sub-millimetre bending radius,” *Nat. Commun.*, vol. 5, no. 3583, 2014.
- [101] M. Vergöhl, D. Rademacher, and A. Pflug, “Progress on optical coatings deposited with dual rotatable magnetrons in a sputter up system,” *Surf. Coatings Technol.*, vol. 241, pp. 38–44, 2014.
- [102] M. A. Green, K. Emery, Y. Hishikawa, W. Warta, and E. D. Dunlop, “Solar cell efficiency tables (version 48),” *Prog. Photovolt Res. Appl.*, vol. 24, no. May 2016, pp. 905–913, 2016.
- [103] A. Morales-Acevedo, “Thin film CdS/CdTe solar cells: Research perspectives,” *Sol. Energy*, vol. 80, no. 6, pp. 675–681, 2006.
- [104] J. Britt and C. Ferekides, “Thin-film CdS/CdTe solar cell with 15.8% efficiency,” *Appl. Phys. Lett.*, vol. 62, no. 22, pp. 2851–2852, 1993.
- [105] Z. Ma, J. McCamy, J. M. Kephart, R. M. Geisthardt, W. S. Sampath, V. V Plotnikov, and A. Compaan, “Superstrate design for increased CdS/CdTe solar cell efficiencies,” in *Conference Record of the IEEE Photovoltaic Specialists Conference*, 2013, no. c, pp. 1150–1155.
- [106] L. a. Kosyachenko, E. V. Grushko, and X. Mathew, “Quantitative assessment of optical losses in thin-film CdS/CdTe solar cells,” *Sol. Energy Mater. Sol. Cells*, vol. 96, no. 1, pp. 231–237, 2012.
- [107] B. Sopori, J. Madjdpour, Y. Zhang, W. Chen, S. Guha, J. Yang, and A. Banerjee, “Optical Modeling of a-Si Solar Cells,” no. November, 1999.
- [108] Pilkington Group Limited, “Global Glass Handbook 2012 Architectural Products,” 2012.

- [109] J. M. Kephart, R. M. Geisthardt, and W. S. Sampath, "Optimization of CdTe thin-film solar cell efficiency using a sputtered, oxygenated CdS window layer," *Prog. Photovolt Res. Appl.*, vol. 23, no. January 2015, pp. 1484–1492, 2015.
- [110] X. Wu, R. G. Dhere, Y. Yan, M. J. Romero, Y. Zhang, J. Zhou, C. DeHart, a Duda, C. Perkins, and B. To, "High-efficiency polycrystalline CdTe thin-film solar cells with an oxygenated amorphous CdS (a-CdS:O) window layer," *Conf. Rec. IEEE Photovolt. Spec. Conf.*, no. May, pp. 531–534, 2002.
- [111] M. Rubin, "Optical properties of soda lime silica glasses," *Sol. Energy Mater.*, vol. 12, no. 4, pp. 275–288, 1985.
- [112] K.-H. Kim and Q-Han Park, "Perfect anti-reflection from first principles," *Sci. Rep.*, vol. 3, pp. 1–5, 2013.
- [113] J. F. Jordan, "Photovoltaic cell and method." Google Patents, 1993.
- [114] C. S. Ferekides, U. Balasubramanian, R. Mamazza, V. Viswanathan, H. Zhao, and D. L. Morel, "CdTe thin film solar cells: Device and technology issues," *Sol. Energy*, vol. 77, no. 6, pp. 823–830, 2004.
- [115] Z. M. Jarzebski and J. P. Marton, "Physical Properties of SnO<sub>2</sub> Materials I. Preparation and Defect Structure," *J. Electrochem. Soc.*, vol. 123, no. 7, pp. 199–205, 1976.
- [116] Y. Wang, I. Ramos, and J. J. Santiago-Avilés, "Optical bandgap and photoconductance of electrospun tin oxide nanofibers," *J. Appl. Phys.*, vol. 102, no. 9, 2007.
- [117] C. S. Ferekides, R. Mamazza, U. Balasubramanian, and D. L. Morel, "Transparent conductors and buffer layers for CdTe solar cells," *Thin Solid Films*, vol. 480–481, pp. 224–229, 2005.
- [118] a. Ismail and M. J. Abdullah, "The structural and optical properties of ZnO thin films prepared at different RF sputtering power," *J. King Saud Univ. - Sci.*, vol. 25, no. 3, pp. 209–215, 2013.
- [119] R. E. Treharne, a Seymour-Pierce, K. Durose, K. Hutchings, S. Roncallo, and D. Lane, "Optical Design and Fabrication of Fully Sputtered CdTe/CdS Solar Cells," *J. Phys. Conf. Ser.*, vol. 286, p. 012038, 2011.
- [120] X. Wu, R. G. Dhere, D. S. Albin, T. a Gessert, C. Dehart, J. C. Keane, a Duda, T. J. Coutts, S. Asher, D. H. Levi, H. R. Moutinho, Y. Yan, T. Moriarty, S. Johnston, K. Emery, and P. Sheldon, "High-Efficiency CTO / ZTO / CdS / CdTe Polycrystalline Thin-Film Solar Cells," *NCPV Progr. Rev. Meet.*, no. October, 2001.
- [121] S. Chaisitsak, T. Sugiyama, a. Yamada, and M. Konagai, "Cu (InGa) Se<sub>2</sub> Thin-film Solar Cells with High Resistivity ZnO Buffer Layers Deposited by Atomic Layer Deposition.," *Jpn. J. Appl. Phys.*, vol. 38, no. 9, pp. 4989–4992, 1999.

- [122] X. W. Sun and H. S. Kwok, "Optical properties of epitaxially grown zinc oxide films on sapphire by pulsed laser deposition," *J. Appl. Phys.*, vol. 86, no. 1, pp. 408–411, 1999.
- [123] E. D. Palik, *Handbook of the Optical Constants of Solids I*, 1st ed. London: Academic Press, 1985.
- [124] K. Durose, P. R. Edwards, and D. P. Halliday, "Materials aspects of CdTe/CdS solar cells," *J. Cryst. Growth*, vol. 197, no. 3, pp. 733–742, 1999.
- [125] X. Wu, P. Sheldon, Y. Mahathongdy, R. Ribelin, a Mason, H. R. Moutinho, and T. J. Coutts, "CdS/CdTe thin-film solar cell with a zinc stannate buffer layer," *Aip Conf. Proc.*, no. October, pp. 37–41, 1999.
- [126] "Deutsche Bank report: Solar grid parity in a low oil price era," 2015.
- [127] T. Leijtens, G. E. Eperon, N. K. Noel, S. N. Habisreutinger, A. Petrozza, and H. J. Snaith, "Stability of Metal Halide Perovskite Solar Cells," *Adv. Energy Mater.*, vol. 5, no. 20, Sep. 2015.
- [128] J. M. Ball, S. D. Stranks, M. T. Hörantner, S. Hüttner, W. Zhang, E. J. W. Crossland, I. Ramirez, M. Riede, M. B. Johnston, R. H. Friend, and H. J. Snaith, "Optical properties and limiting photocurrent of thin-film perovskite solar cells," *Energy Environ. Sci.*, vol. 8, no. 2, pp. 602–609, 2015.
- [129] A. Leguy, P. Azarhoosh, M. I. Alonso, M. Campoy-Quiles, O. J. Weber, J. Yao, D. Bryant, M. T. Weller, J. Nelson, A. Walsh, M. van Schilfgaarde, and P. R. F. Barnes, "Experimental and theoretical optical properties of methylammonium lead halide perovskites," *Nanoscale*, vol. 8, pp. 6317–6327, 2015.
- [130] P. J. M. Isherwood, N. Neves, J. W. Bowers, P. Newbatt, and J. M. Walls, "High quality aluminium doped zinc oxide target synthesis from nanoparticulate powder and characterisation of sputtered thin films," *Thin Solid Films*, vol. 566, pp. 108–114, Sep. 2014.
- [131] A. Klein, C. Körber, A. Wachau, F. Säuberlich, Y. Gassenbauer, S. P. Harvey, D. E. Proffit, and T. O. Mason, "Transparent Conducting Oxides for Photovoltaics: Manipulation of Fermi Level, Work Function and Energy Band Alignment," *Materials (Basel)*, vol. 3, no. 11, pp. 4892–4914, Nov. 2010.
- [132] N. Romeo, A. Bosio, V. Canevari, M. Terheggen, and L. Vaillant Roca, "Comparison of different conducting oxides as substrates for CdS/CdTe thin film solar cells," *Thin Solid Films*, vol. 431–432, pp. 364–368, May 2003.
- [133] S. Calnan and A. N. Tiwari, "High mobility transparent conducting oxides for thin film solar cells," *Thin Solid Films*, vol. 518, no. 7, pp. 1839–1849, Jan. 2010.
- [134] A. C. Galca, G. Socol, and V. Craciun, "Optical properties of amorphous-like indium zinc oxide and indium gallium zinc oxide thin films," *Thin Solid Films*, vol. 520, no. 14, pp. 4722–4725, 2012.

- [135] A. C. Gâlcă, M. Secu, A. Vlad, and J. D. Pedarnig, “Optical properties of zinc oxide thin films doped with aluminum and lithium,” *Thin Solid Films*, vol. 518, no. 16, pp. 4603–4606, 2010.
- [136] A. Gupta and A. Compaan, “14% CdS/CdTe thin film cells with ZnO: Al TCO,” in *MRS Proceedings*, 2003, vol. 763, pp. 1–6.
- [137] F. Kurdesau, G. Khripunov, a. F. da Cunha, M. Kaelin, and a. N. Tiwari, “Comparative study of ITO layers deposited by DC and RF magnetron sputtering at room temperature,” *J. Non. Cryst. Solids*, vol. 352, no. 9–20, pp. 1466–1470, Jun. 2006.
- [138] P. M. Kaminski, A. Abbas, J. W. Bowers, G. Claudio, B. Maniscalco, J. M. Walls, M. L. Crozier, and A. N. Brunton, “Characterization of contacts produced using a laser ablation/inkjet one step interconnect process for thin film photovoltaics,” in *Conference Record of the IEEE Photovoltaic Specialists Conference*, 2013, pp. 1694–1699.

# 11 PUBLICATIONS

1. G. Womack, P.M. Kaminski, J.M. Walls, "The performance and durability of broadband Antireflection Coatings for Thin Film CdTe Solar Cells" *Journal of Vacuum Science and Technology*, Volume 35, Issue 2, Jan 2017. doi: <http://dx.doi.org/10.1116/1.4973909>
2. G. Womack, P.M. Kaminski, J.M. Walls, "Optical optimisation of high resistance buffer layers in thin film Cadmium Telluride Solar Cells" *Vacuum*, 2016 doi: 10.1016/j.vacuum.2016.11.031
3. P.M. Kaminski, P.J.M. Isherwood, G. Womack, J.M. Walls, "Optical Optimisation of Perovskite Solar Cell Structure for Maximum Current Collection", *Energy Procedia*, Volume 102, pp. 11-18, 2016. doi: 10.1016/j.egypro.2016.11.312
4. G. Womack, P.M. Kaminski, J.M. Walls, "High Temperature Stability of Broadband Anti-Reflection Coatings on Soda Lime Glass for Solar Modules" in 42nd IEEE PVSC, 2015.
5. P.M. Kaminski, G. Womack, J.M. Walls, "Broadband Anti-Reflection coatings for Thin Film Photovoltaics," in 40th IEEE PVSC, 2014.